EPFL

Thèse n° 8109

Engineering Absorption for Foil Applications

Présentée le 20 mai 2022

Faculté des sciences et techniques de l'ingénieur
Laboratoire de nanophotonique et métrologie
Programme doctoral en photonique

pour l'obtention du grade de Docteur ès Sciences

par

Sebastian MADER

Acceptée sur proposition du jury

Prof. C. Moser, président du jury
Prof. O. Martin, directeur de thèse
Prof. H. Giessen, rapporteur
Prof. S. Bozhevolnyi, rapporteur
Prof. D. Norris, rapporteur

École polytechnique fédérale de Lausanne

2022

Acknowledgements

Let me first thank Olivier, who agreed five years ago to supervise me. What did I expect five years ago? Certainly not such a commitment and understanding. Thank you for the very interesting and enjoyable time we spent together, discussing, revising, and improving our research. Thanks for being available often at late hours or during weekends. The double burden of doing a PhD and simultaneously working in industry would not have been possible without your understanding and flexibility. Thanks for your curiosity, openness, excitement, advice, and commitment!

It was a pleasure to meet other members of the Nanophotonics and Metrology Laboratory on my rare visits at EPFL. Despite working mostly remote, I always felt very welcome and enjoyed our interactions. Especially, the ones on simulations with Andrei and Raziman as well as the ones on chemistry with Debdatta and Madasamy. Thanks also to David for promptly resolved my occasional IT issues.

Many thanks also to my employer, who let me work on my PhD studies during part of my working schedule. Special thanks to my supervisor Harald and our head R&D Achim for their general support of my PhD and making it possible within this framework. Thank you also for proofreading and enriching our articles as well as my thesis with your industrial expertise. Thanks also to Christian, Corrado, Gina, and Oliver for their understanding and assistance at work, when a week had just too few hours and you took over some of my duties.

Thank you to the members of the thesis committee, Prof. Sergej Bozhevolnyi, Prof. Harald Giessen, Prof. David Norris, and Prof. Christoph Moser for their time and involvement. Thank you for reading my thesis, taking part in the oral exam, and challenging questions to improve depth and scientific quality of my thesis.

I would like also to thank Rossen Todorov and Thomas Mayerhöfer. Both responded immediately upon my requests. Thank you Rossen for your technical advice on retrieving refractive index data for thin metal layers and Thomas for obtaining refractive index data with high precision. We had a pleasant exchange on both topics and your contributions clearly improved my modeling.

Thanks to my parents and siblings: Simone, Klaus, Rebecca, Christoph, and my second family: Erika, Karl, Sereina, Andrin, and Aaron. This adventure would not have been possible without your support! The countless hours that one of you took care of our beloved sons Andrin and Aaron. Thanks for agreeing to spend evenings, weekends, and even whole vacations together, so I could sit in the library to focus on my academic studies and writing my PhD. Andrin, next time you ask “Papi, bisch wiedär am schriibä?”, I can truly say I am done writing and look forward to spending more time with you and the rest of our family!

Abstract

Light matter interactions such as extinction, reflection, and transmission can be described by classical optics. During the past decades, research focused on a novel resonant extinction type called plasmonics that allows for enhancement of both types of extinction, absorption and scattering, depending on the size of the involved nanostructures. Plasmonics is a resonant interaction of light with conducting matter, especially metals with a free electron density in excess of 10^{22} cm^{-3}. The incident light excites oscillating electrons movement and this leads to absorption cross sections far exceeding the geometrical ones for sub-micron sized metal particles.

In this thesis, I research resonant absorption phenomena in three different and rather classical systems that can be principally manufactured on industrial scale using modern foil production. The chosen systems are carefully studied by simulations to reveal important parameters for tuning absorption for the application at hand. I reveal that the underlying absorption mechanisms of these three systems are different and, depending on the application, one may select the most suitable of these three systems to exploit narrow or broadband absorption.

The first system is based on interacting and randomly arranged metal nanoparticles placed atop a mirror surface forming a lossy Fabry-Perot cavity. Its sensitivity to parameters such as mirror distance, particle shape, polarization, spacing, metal type, and dielectric environment are investigated. This random system maximizes absorption across the entire visible spectrum and offers the flexibility to alter various system parameters including metal type and filling fraction to shift the absorption band spectrally at will. The focus of the second system is a simplification of the first one to facilitate mass production and reproducibility of the system, while still achieving near perfect absorption across the visible spectrum. This initially black appearing system is then modified locally by laser processing to realize high reflection or full transmission depending on laser pulse energy. The influence of the system parameters on the laser process window are investigated in detail and the findings are applied to realize a colorful 3D art print consisting of black, reflective, and transparent microscopic elements. The third and last investigated system enhances absorption of three dye lacquers atop corrugated surfaces. It is found that the interaction of a metal crossed grating with these dye lacquers can enhance absorption locally up to a factor of 20. Compared to applying the same lacquers on flat surfaces, this strong enhancement turns otherwise barely visible dye lacquers colorful and vivid.

The results demonstrate that very different systems can be used for absorption optimization. Each system uses a unique mechanism for local field enhancement to achieve strong absorption, inter-particle coupling, interference, or interaction of propagating as well as evanescent grating orders. The systems studied in this thesis can be mass produced using cost effective and scalable roll-to-roll foil production. This makes them especially attractive for applications in document authenticity protection and visual sensing, but also any other application that demands tuning of absorption to a selected spectral band.

Keywords: absorption, coatings, gratings, interference, laser processing, optics, plasmonics, perfect black, simulation, sub-wavelength structures.

Abstrakt

Die klassische Optik kann Wechselwirkungen zwischen Licht und Materie wie Extinktion, Reflexion und Transmission beschreiben. Die Forschung fokussierte in den letzten Jahrzehnten auf eine neue Form der resonanten Extinktion, genannt Plasmonik, welche beide Formen der Extinktion, Absorption und Streuung, in Abhängigkeit von der Grösse der beteiligten Nanostrukturen verstärken kann. Plasmonik ist eine resonante Wechselwirkung von Licht mit elektrisch leitender Materie, insbesondere Metalle mit einer freien Elektronendichte grösser 10^{22} cm^{-3}. Das einfallende Licht regt eine oszillierende Elektronenbewegung an und dies führt für Submikrometer grosse Metallpartikel zu Absorptionsquerschnitten, welche die geometrischen Querschnitte weit übersteigen.

In dieser Doktorarbeit untersuche ich resonante Absorptionsphänomene in drei verschiedenen und eher klassischen Systemen, welche prinzipiell in industriellem Massstab mit moderner Folienproduktion hergestellt werden können. Die ausgewählten Systeme werden detailliert mittels Simulationen untersucht, um die relevantesten Parameter für das Anpassen der Absorption für Zielanwendungen zu ermöglichen. Ich zeige, dass die zugrundeliegenden Absorptionsmechanismen für diese drei Systeme unterschiedlich sind und man in Abhängigkeit von der Anwendung das passendste dieser drei Systeme auswählen kann, um schmal- oder breitbandige Absorption auszunutzen.

Das erste System basiert auf der Wechselwirkung von zufallsmässig angeordneten, metallischen Nanopartikeln, die oberhalb einer Spiegelfläche platziert sind und so eine verlustbehaftete Fabry-Perot Kavität bilden. Die Empfindlichkeit von Parametern wie Spiegelabstand, Partikelform, Polarisation, Abstand zwischen Partikeln, Metallart und dielektrischen Medium wird untersucht. Dieses Zufallssystem maximiert die Absorption im gesamten sichtbaren Spektrum. Es bietet die Flexibilität verschiedenste Systemparameter zu variieren um das Absorptionsband spektral zu verschieben, unter anderem die Metallart und den Füllfaktor. Der Fokus des zweiten Systems ist die Vereinfachung des ersten, um Massenproduktion und Reproduzierbarkeit zu erleichtern, aber trotzdem eine nahezu perfekte Absorption im gesamten Spektrum zu erreichen. Die resultierende schwarze Erscheinung des Systems wird dann mittels gepulster Laserprozessierung modifiziert, um lokal eine hohe Reflexion oder komplette Transmission zu erreichen. Der Einfluss von Systemparametern auf das Laserprozessfenster wird systematisch untersucht und die Erkenntnisse für die Realisierung eines farbigen 3D-Kunstdruck angewandt, welches aus mikroskopischen schwarzen, reflektierenden und transparenten Bereichen besteht. Das dritte und final untersuchte System verstärkt die Absorption von drei Farbstoffschichten auf strukturierten Oberflächen. Die Untersuchungen zeigen, dass die Absorption dieser Farbstoffe lokal um mehr als Faktor 20 erhöht werden kann bedingt durch Wechselwirkung dieser Farbstoffschichten mit metallischen Kreuzgittern. Diese grosse Verstärkung resultiert in klar farbigen Oberflächen im Vergleich zum nahezu farblosen Eindruck derselben Farbstoffschichten auf ebenen Oberflächen.

Diese Resultate zeigen, dass sehr stark unterschiedlichen Systeme zum Optimieren der Absorption genutzt werden können. Jedes System nutzt hierfür einen einzigartigen Mechanismus; Kopplung zwischen Partikeln, Interferenz oder die Wechselwirkung von propagierenden und evaneszenten Beugungsordnungen. Die in dieser Doktorarbeit untersuchten Systeme können in Masse produziert werden mit kostengünstiger und skalierbarer Folienproduktion im Rolle-zu-Rolle Verfahren. Das macht sie besonders attraktiv für Anwendungen im Dokumentenschutz und für visuelle Sensorik, aber auch jede andere Anwendung, die von der gezielten Anpassung des spektralen Absorptionsbandes profitiert.

Schlagwörter: Absorption, Beschichtungen, Gitter, Interferenz, Laserprozessierung, Optik, Plasmonik, perfektes schwarz, Simulationen, Subwellenlängenstrukturen.

Content

Chapter 1 Introduction

With all its different forms, the interaction of light with matter leads to many interesting phenomena. Light interactions such as extinction, reflection, and transmission can often be accurately analyzed with classical optics [1,2]. During the past decades, a significant research effort has focused on a resonant type of extinction called plasmonics [3]. Here, the incoming light excites oscillating electron movements within matter, especially metals with a free electron density in excess of 10^{22} cm^{-3}, which in turn leads to strong extinction by scattering and/or absorption. Classical and plasmonic concepts are used in this thesis to describe, understand, and engineer absorption mechanisms in three different systems.

Absorption is a fascinating light interaction as the result can easily be observed and judged visually, i.e. determining the color of an object, while the underlying absorption origin can be counter intuitive. For example, black surfaces can be realized with systems involving randomly placed gold particles [4], while similarly sized gold particles dissolved in water lead to colorful red solutions, turning transparent water colorful [5]. Both exemplary systems are based on the material gold, which is neither black nor red in its natural state. It is the miniature size of the gold particles involved and the system surrounding them that determine the particular absorption behavior in both cases. It is thus key to understand the mechanisms behind the absorption system at hand in order to be able to engineer and exploit absorption for a specific application [3].

Plasmonic phenomena can be categorized into two forms : localized surface plasmons and (propagating) surface plasmon-polaritons or short surface plasmons [6]. The latter often need specific setups and/or conditions for their excitation, which makes them less interesting from a practical point of view [3]. In the case of localized plasmons this hurdle is not present as one can excite collective electron movements by direct light illumination. Localized plasmonic systems in their simplest form are individual metal particles. The excitation of the particles conduction electrons usually leads to strong resonant extinction over a rather narrow bandwidth and it is the particle size, which mainly determines the extinction type. In the case of a spherical silver particle embedded in a medium with refractive index of 1.5, light is mostly absorbed for particle diameters below 20 nm at an excitation wavelength of 520 nm, see Figure 1-1.

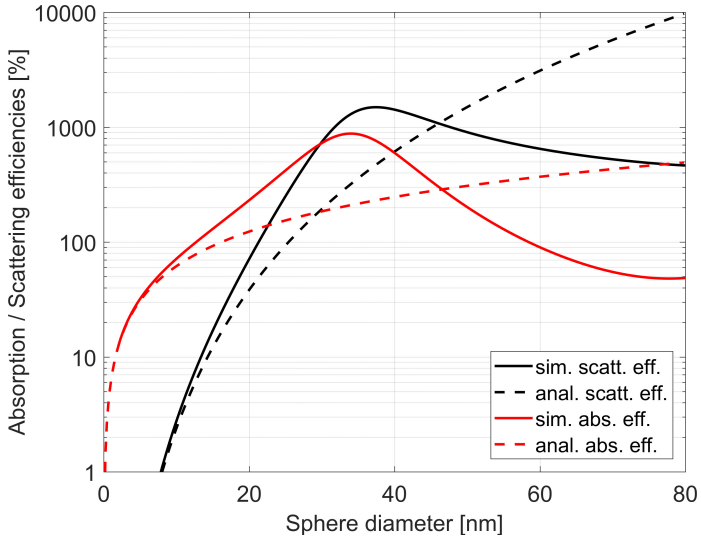

The simulations in Figure 1-1 were carried out with MiePlot and its provided material data for silver was used [7]. For small particle diameters one can derive analytical formulas for both, absorption Q_{abs} and scattering efficiencies Q_{sca} based on electrostatic polarizability [1],

$$Q_{abs} = 4x\, Im\left\{\frac{\varepsilon_m - \varepsilon_d}{\varepsilon_m + 2\varepsilon_d}\right\}, \qquad Q_{sca} = \frac{8}{3}x^4 \left|\frac{\varepsilon_m - \varepsilon_d}{\varepsilon_m + 2\varepsilon_d}\right|^2, \qquad x = \frac{\pi n_d d}{\lambda_0}, \tag{1-1}$$

where ε_d is the permittivity of the dielectric surrounding medium, ε_m the permittivity of the metal sphere, n_d the refractive index of the dielectric surrounding medium, d the particle diameter, and λ_0 the vacuum wavelength. Larger particles mainly scatter, independently of the material, as indicated by Mie theory [1]. It is only for specific metals that the absorption efficiency can exceed 100%. For example, a 34 nm silver sphere absorbs almost ten times more light in the green than predicted by its geometrical cross section as confirmed by Figure 1-1.

Besides exceptionally high absorption efficiency, the light excitation of plasmonic resonances also leads to strong local field enhancement at the resonance wavelength for small particles, where absorption dominates [8]. This is especially pronounced at the particle edges and falls of very rapidly (with the third inverse power) at distances of a few nanometers from the surface [9]. Both observations are very relevant to absorption applications as they can enable for example high sensitivity and spatial resolution, which are important for many sensing applications [10,11]. Of course, exploiting this enhancement at nanometer dimensions also demands very smooth surfaces [12,13]. Depending on the applications requirements, the central resonance wavelength and bandwidth of the plasmonic resonance can be tuned by material choice [5,14], dielectric environment [15], and/or shape of the involved nanostructures [8,16]. These small particles can consequently absorb resonantly part of the visible spectrum (VIS) for the right material and shape combination and particles of similar sizes, but different shapes result in distinguishably different spectra [9,17], see Figure 1-2. This is somewhat surprising as it is possible to create plasmonic colors even with naturally colorless metals such as aluminum or silver. The involved particles are often only a few nanometers in size and with suitable methods, they can be applied on a substrate with a precision in the sub-micron range [18–21]. This is something that is not achievable with classical coloration means such as dyes and pigments, where the smallest printable details are in the range of 10 µm [22]. Nonetheless, both are heavily used for printing and colorization of consumer goods today [23].

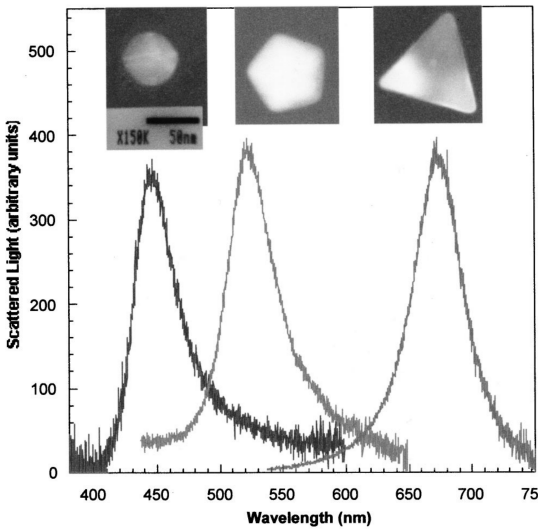

Figure 1-2. Typical optical spectroscopy measurements of individual silver nanoparticles. The figure shows the spectrum of an individual red, green, and blue particle, and the high-resolution TEM images of the corresponding particle are shown above their respective spectrum. This example is a representative of the main conclusion that the triangular shaped particles appear mostly red, particles that form a pentagon appear green, and the blue particles are spherical.
Reprinted from [17], with the permission of AIP Publishing.

High resolution printing and colorization are just two examples of possible utilizations for plasmonic absorption in small metallic particles. For these and other applications, the absorption efficiency offered by individual or sparsely placed

particles might not be strong enough. One strategy to increase absorption of individual particles is increasing their size, but this leads to stronger scattering and from intermediate particle sizes onwards even lower absorption efficiencies, see Figure 1-1. Alternatively, one can position small particles at shorter distances to alter and increase the plasmonic resonance by near-field coupling of two or more particles. It can be shown that in the case of a dimer, individual particle modes hybridize to form new and potentially stronger plasmonic modes depending on the particle size, shape and spacing [24–26]. Placing such dimers in a cavity offers even greater flexibility to alter the resonance amplitude and bandwidth. Depending on the location of the particle within the cavity, i.e. with respect to nodes of the standing waves pattern formed by the incident light, the coupling of particle and cavity modes is altered. This mechanism allows for the excitation of more and potentially stronger plasmonic modes within the particles [27,28].

A natural extension of the dimer concept is placing particles in chains with controlled spacing [29,30] with even greater potential to alter and further enhance resonances. In analogy to dimers, these chains can also be placed atop mirror surfaces, forming effectively an open and thus very lossy cavity. It has been shown that cavities can enhance the resonance strength by more than a factor of two [31]. This enhancement might be attributed to four mechanisms, intercoupling of neighboring particles [30], additional light from the reflection at the mirror interface [32], coupling of the particle with its mirror image [32], and coupling between localized and propagating plasmons along the mirror surface [33]. The dominating mechanisms must be identified for each system of interest, but absorption cross section must generally exceed the particle spacing for notable inter-particle coupling [34].

Engineering absorption based on small and possibly interacting metallic particles is already very promising, but modern lithographic technology allows for reproducible fabrication of much more complex geometries. This methodology is often applied for color generation and three extensive reviews summarize well the current state in plasmonic color generation [35–37]. These reviews show that for this purpose, plasmonic nanostructures are often periodically arranged and positioned atop a reflective back mirror. It is the spacing and nanostructure size that determine whether the individual nanostructures interact with each other. Consequently, the highest possible color generation resolution is achieved for nanostructures that are separated enough to avoid strong near-field coupling [34]. On the contrary, one often employs a periodic array of tightly spaced nanostructures that couple and enhance each other's absorption by resonant coupling [23,38,39]. While much research is focused on structures that create a colorful response, which is mostly independent of the incident light polarization, the dependency on the latter can also be beneficial. This dependency can be applied to authenticity protection applications [40] or to optimization of the target color's saturation [41]. The exploitable polarization sensitivity is usually a consequence of elongated structures in one direction that strongly brake the nanostructures symmetry [42–44].

Besides color generation, similar approaches were also employed in general broadband absorption optimization for applications in optical filtering, thermophotovoltaics, thermal emitters, and hot-electron collection [45,46]. Analog to color generation, this optimization is often achieved with periodically arranged nanostructures to maximize absorption across the desired wavelength band [47–53]. However, the absorption based on periodic structure is usually rather narrowband, which can be overcome by employing randomly arranged nanostructures or nanoparticles [54–57]. Note that, although this strategy is rarely used for color generation, one can also use randomly distributed particles for it [58]. A possible reason why random structures are generally less often used for narrow or broadband absorption is likely the more complex description, reproduction, and analysis of these systems. Often the analysis of random systems is only possible based on average parameters, for example mean diameter and spacing of the randomly arranged structures or particles [59]. Consequently, these random arrangement effects are quite complex to capture and reproduce in experiments as well as in simulation models.

The objective of this thesis is to address this difficult modelling of randomized systems by drawing a link between simpler and well-ordered few particle systems and the response of systems involving many randomly placed particles. Further, well-ordered systems are optimized for original approaches in local absorption switching and color generation. The selected absorption systems are analyzed in detail by simulations and can be industrialized with cost effective and scalable roll-to-roll foil processes.

Chapter 2 investigates the most relevant parameters for strong absorption of a few well-aligned particles in a lossy Fabry-Perot cavity. The findings are then applied to understand the near perfect and broadband absorption across the entire VIS for randomly distributed particles embedded in a dielectric layer atop a mirror. In Chapter 3, the random system is simplified by replacing the embedded particles with a homogenous chromium layer. This system also appears nearly perfect black after optimization but can be modified locally by laser processing. It is shown how the initially black appearance can be switched to a highly reflective or even a fully transparent one and the influence of the system parameters on the laser processing window are also systematically studied. Both chapters are based on systems that absorb nearly all light within the VIS, while the grating systems studied in Chapter 4 only absorb a fraction of the VIS and can thus be used for color generation. The selected crossed grating produces a self-color in direct reflection, which is enhanced and altered by overcoating it conformally with different dye lacquers. The results reported in this chapter reveal why and how the absorption of the dye lacquer is enhanced locally through the crossed gratings by more than a factor of thirty. Comments on industrial scalability and applications are provided in the final section of each individual chapter, while the final Chapter 5 draws general conclusions on the obtained results together with an outlook for future developments.

Chapter 2 Mechanisms of perfect absorption in nano-composite systems

The results in this chapter are inspired by an initial literature search on plasmonic systems that are essentially compatible with roll-to-roll foil manufacturing and part of this chapter was published elsewhere [14]. I conceived the ideas and designed simulations in this article, while both authors analyzed and discussed the results in close collaboration and co-wrote it. The chapter is an extended version of that publication with additional content on the system parameters, like the role of the source polarization or the embedding media. An additional discussion on the possibility to manufacture this system on an industrial scale completes this chapter.

The researched absorption system in this chapter is a metal insulator metal (MIM) system that can absorb light across the entire VIS [33]. Such 3-layer systems consist typically of a metallic base layer (mirror layer), a dielectric spacer layer and an at least partially metallic top layer. Note that dielectric top layers have also been explored to maximize absorption bandwidth and strength [60]. The system researched here numerically, was manufactured experimentally by evaporation and co-evaporation of gold and glass SiO_2, a metal and dielectric respectively [56]. The layout of the experimentally fabricated MIM system is visualized in Figure 2-1(a) and, as only evaporation steps are needed, the process is straightforward to upscale to an industrial scale. However, upscaling has its pitfalls as outlined in Section 2.5.1.

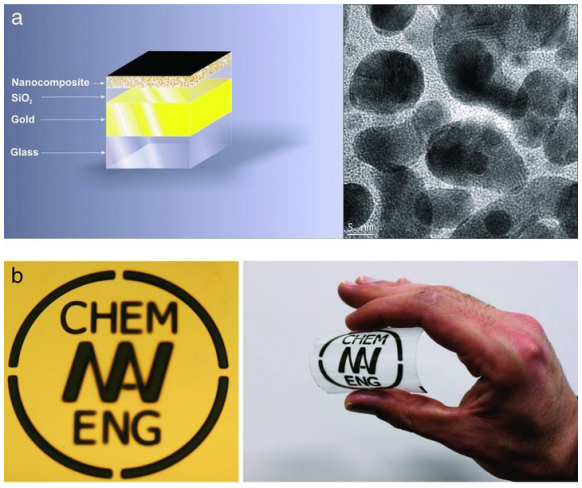

Figure 2-1. Nearly perfect absorbing MIM system realized by Hedayati et al. [56]. (a) Schematic of the perfect absorber structure manufactured by sputtering. The thickness of the nanocomposites, SiO_2 spacer, and the gold mirror are 20, 25, and 100 nm, respectively. The left panel illustrates that the whole structure resides on a glass substrate; the right panel shows a top-view TEM image of the nanocomposite film. (b) Perfect absorber (blackbody) coated via a mask on gold-coated glass (left) and flexible polymer foil (right). These examples show the potential of the coating for application on a flexible substrate.

The visual appearance of an experimental sample photographed in Figure 2-1(b) is indeed very dark and thus confirms the desired strong absorption in the VIS. It is fascinating that a system consisting only of transparent and highly reflective materials can absorb almost 100% of the incident light and the objective of this chapter is to elucidate the underlying physical phenomenon. The analysis of this system led me to research a much simpler system that can be modified by laser processing and is described in Chapter 3.

Section 2.1 gives a general overview of the state of the art in MIM systems that are optimized for strong absorption. The results in this chapter are all based on numerical simulations and the methodology as well as the main model parameters are described in Section 2.2. Experimental MIM systems contain thousands of possibly overlapping particles that are randomly arranged, which are challenging to simulate and analyze. Therefore, much simpler systems that contain only a few and well aligned particles are analyzed first in Section 2.3. This analysis reveals the influence of many systems parameters on absorption strength and location. This knowledge helps understand the conclusions on the much more complex and realistic multi particle systems studied in Section 2.4. The findings are summarized in the final Section 2.5, where also the possibility to manufacture such a system on an industrial scale is discussed.

2.1 State-of-the-art in MIM systems

Several MIM systems with periodic and thus well-ordered top layers have been manufactured over the years to maximize absorption across the desired wavelength band [25,47–53]. These periodic systems can achieve broad-band absorption levels in the range of 60-80% for the case of thoroughly optimized systems [47], while certain systems can even absorb up to 100% in the infrared spectrum [48]. Orienting the MIM system vertically enables a similar performance also in the VIS and even ultra-violet (UV) range [50]. The periodicity and the generally well-defined geometry enables a theoretical analysis, including the dipolar and quadrupolar resonances at hand [25]. It is also possible to quantitatively study the coupling of the localized surface plasmon (LSP) mode of the individual nanostructures with the surface plasmon polariton (SPP) of the metallic mirror layer [49]. All these well-ordered structures require however high precision manufacturing processes, such as electron beam lithography, which limits manufacturing throughput and structured area size. Both limitations can be overcome in systems that rely either on homogenous or random layers. Generally, one may classify absorbing MIM systems into four categories:

1. Layered systems with 2D-periodic top layers [47,52,61,62]
2. Layered systems with homogenous top layers [45,63–65]
3. Layered systems with random top layers [54–56,66,67]
4. Deep and often random metallic nanostructures [68–71]

The latter are rather IM systems instead of true MIM systems; they are included here as they also rely on absorption within a metal layer for maximizing absorption. The main features of these systems are summarized in Table 2-1.

Ref.	Investigated system	Layers	Type	Peak abs. [%]	Peak WL [nm]	Bandwidth [nm]	Pol.-sens.	Angle-sens.
[47]	2D-periodic Ag patterns at a distance from a Ag mirror	3	E, S	85	560	150	no	yes
[52]	2D-periodic Au discs at a distance from a Au mirror	3	E, S	99	1610	110	no	no
[61]	2D-periodic hole patterns in Au (void plasmons)	1	E, S	100	750	25	no	no
[62]	2D-periodic Au particles at a distance from a Au mirror	3	E, S	88	1580	100	yes	no
[45]	Homogenous Cr layer at a distance from a Cr mirror	3	E, S	99	600	>350	no	no
[63]	Homogenous Cr layer between two SiO_2 layers on Au mirror	4	E, S	98	1100	900	no	no
[64]	Two pairs of alternating silica and Ti films on Au mirror	5	E, S	98	650	>500	no	no
[65]	Homogenous W layer between two Al_2O_3 layers on W mirror	4	E, S	98	625	1200	no	no
[56]	**Random Au nano-composite at a distance from a Au mirror**	**3**	**E**	**100**	**575**	**400**	**no**	**no**
[54]	Random Ag nano-composite on glass	2	E	57	750	1250	n/a	n/a
[55]	Random Ag nano-composite on glass	2	E, S, A	97	600	>600	no	no
[66]	Random Au nano-composite at a distance from a mirror	3	S	98	620	>250	n/a	n/a
[67]	Random Ag nano-composite at a distance from a Ag mirror	3	E, S, A	98	550	380	n/a	n/a
[68]	Ag gratings of a few nm deep ridges	1	S	98	475	20	yes	n/a
[69]	2D-periodic deep grooves in Au	1	E, S	98	670	>400	no	n/a
[70]	2D-periodic nanocones in Au	1	E	99	550	>500	n/a	no
[71]	Random nanocones in Al	1	E	94	600	>300	n/a	n/a

Table 2-1. Summary of absorbing metal systems and their specific characteristics.

Table 2-1 includes for each reference a brief description of the system and the number of layers, excluding the superstrate. The type indicates whether the article contains experimental data (E), simulations (S), and/or an extensive analytical section (A). The values for peak absorption, peak wavelength, and bandwidth are extracted from experimental data, where possible. The bandwidth is determined between limiting values of 90% peak absorption and the greater sign is used, when the bandwidth exceeded the plot dimensions. The sensitivity is evaluated when angle- or polarization-data are provided. The criteria for no polarization sensitivity is satisfied when the absorption spectra differ by less than 20% for both polarizations, up to 45° incidence angle. The criterion for no angular sensitivity is more strict and requires that absorption spectra change less than 10% for up to 45° incidence angle, which corresponds to typical viewing conditions with the naked eye.

Table 2-1 indicates that near perfect absorption of greater 95% can be achieved by a plurality of systems that rely on different strategies. The achieved bandwidth varies however strongly, ranging from a few tens of nanometers to more than 1000 nanometers. The investigated system in this chapter, which was experimentally realized by Hedayati et al. [56] and is highlighted in bold in Table 2-1, has true perfect absorption at the peak wavelength of 575 nm and a moderate bandwidth of 400 nm. The top layer contains randomly sized and arranged metal nanoparticles that are usually embedded in a dielectric matrix and called nano-composite layer in this chapter. It is a very appealing system for which both – peak wavelength and bandwidth – can be tuned by varying the metal filling fraction of the nano-composite layer. Thus, this system offers more flexibility compared to layered systems with homogenous top layers [45,63–65]. Further, its performance is largely insensitive to polarization as well as incidence angle of the incoming light and in principle mass producible as shown in Section 2.5.1. Last but not least, it consists only of flat layers and consequently no nanostructure replication is needed in contrast to systems relying on deep and often random metallic nanostructures [68–71]. Its fabrication required only the precise control of evaporation rates of gold and SiO_2 in three successive evaporation steps [56] and similar optical performance was observed for gold, silver and copper based nano-composites [72]. Thus, the system can be manufactured with a variety of materials and no high precision manufacturing processes are required, contrary to layered systems with 2D-periodic top layers [47,52,61,62]. Note that the nano-composite layer can be created by direct thin layer evaporation [73–76], thermal annealing [77–79], laser-induced dewetting [80], co-evaporation [54–57], spin-coating [81] or even through simple drop-casting [82].

The random nature and nanometer dimensions of the composite layer makes an insightful analytical analysis of the system's optical properties difficult; especially the key parameters that lead to this exceptional performance. Thus, other authors resorted to studying this system numerically using finite difference time domain (FDTD) algorithms [59,66]. On one hand, Etrich et al. focused on retrieving the optical parameters of the nano-composite layer through simulations and optimized the dielectric spacer thickness to enhance absorption [59]. This optimization was carried out with a transfer matrix algorithm, which results agreed very well with those obtained by FDTD. On the other hand, Feng et al. researched the optical parameters required to achieve high and broadband absorption [66]. They identified for example that perfect absorbers require a dielectric spacer layer at least 20 nm thick to assure modest requirements on the nano-composite layer permittivity.

Both research groups treated the metallic nano-composite layer as a homogenous, dispersive, and isotropic material and focused on its "macroscopic" properties. In contrast, the focus in this chapter is on understanding the microscopic absorption mechanisms of the system described in [56]. In particular, the question why light is absorbed with such a broad bandwidth and where it is absorbed locally. Possible resonance broadening mechanisms associated with variations of the gold particles shape, size, position or plasmonic coupling to the metal mirror were suggested in [56,72]; however, the latter mechanism can be ruled out, as discussed in Section 2.3. Instead, the resonance broadening effect is assigned to lossy Fabry-Perot interferences in combination with plasmonic inter-particle coupling. These findings are based on numerical simulations and the methodology is described in the next section.

2.2 Simulation methodology

Lumerical FDTD, a commercial-grade simulator based on the FDTD method is used to perform all simulations below [83]. Figure 2-2 shows the general simulation layout used in this chapter. It consists of a linear polarized light source in the x-z-plane, a metallic nano-composite layer, a dielectric spacer layer and a mirror layer. The nano-composite layers in Section 2.3 consist of a few individual and well-aligned particles as schematically illustrated in Figure 2-2(a). Contrary, in Section 2.4 the nano-composite layer contains many randomly placed layers to mimic the experimental system. These layers are stacked periodically in the vertical direction as shown in Figure 2-2(b) for four stacked particle layers. Both MIM structures are embedded in a lossless dielectric background of constant refractive index 1.5. Linear polarized plane waves first impinge on the nano-composite layer before they pass the dielectric spacer layer and then hit the 100 nm thick metallic mirror layer. Bloch-type periodic boundary conditions have been used in x-y-directions and power detectors were placed at appropriate positions.

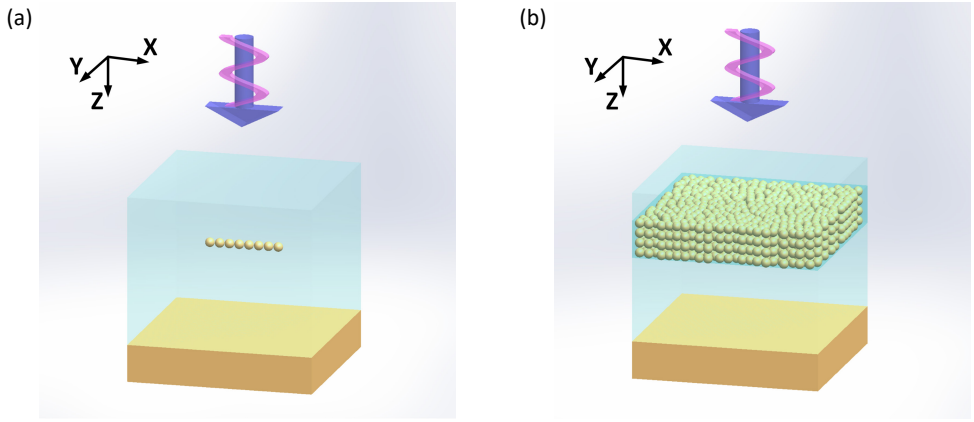

Figure 2-2. Schematical visualization of the simulated 3-layer model. (a) Few particle system with 8 particles. (b) Many particle system with 4 gold particle layers.

Table 1 summarizes all relevant parameters that are used for the simulations. The particle diameter value is kept constant as size variations mainly lead to different resonance amplitudes, following the arguments by Etrich et al. [59]. Note that the mesh's spatial resolution is set to 0.3 nm in and around the spheres. This high resolution was selected to assure good convergence of the solution.

Parameter	Value
FDTD-simulation region	100 nm × 100 nm × 2000 nm
Boundary conditions	Bloch in X- and Y-direction. Perfect matching layer (PML) with 32 layers in z-direction
Mesh type, refinement, and accuracy	Auto non-uniform, conformal variant 1 and level 5
Time step and minimum mesh size	dt stability factor 0.99 and 0.3 nm
Source	Linear polarized light in the X-Z-plane with bandwidth 300-800 nm. Injected at z = -800 nm with unit amplitude
Frequency domain power monitors	Transmission is recorded at z = 700 nm Reflection is recorded at z = -700 nm by subtracting the source's field from the measured one (most accurate)
Gold spheres	Constant diameter of 5 nm
Mirror layer	Spanning across the X-Y-plane Placed at Z = -90 nm, if not stated otherwise
Material parameters	Au (Gold) Johnson and Christy with 8 coefficients Al (Aluminum) CRC with 6 coefficients Ag (Silver) CRC with 6 coefficients All with 0.1 fit tolerance
Dielectric background and spacer	Constant value of 1.5
Early Shutoff	1E-6

Table 2-2. Summary of relevant simulations parameters.

The early shutoff parameter determines the criterion for a simulation to terminate when the remaining energy in the simulation volume is lower than this value. The value of 1E-6 reported in Table 2-2 is sufficient for almost all the results in this chapter except for some of the results in Section 2.3.2, where the absorption of particles with large gap sizes is determined. This is achieved by calculating the absorption of a single particle from the simulated reflection as shown below. In short, the very small absorption signal is extracted from a large reflection signal. Figure 2-3 highlights the importance of the early shutoff parameter for such cases to minimize residual ripples in the quantity of interest: here a value of 1E-10 is necessary, while for most other cases the default of 1E-6 is sufficient.

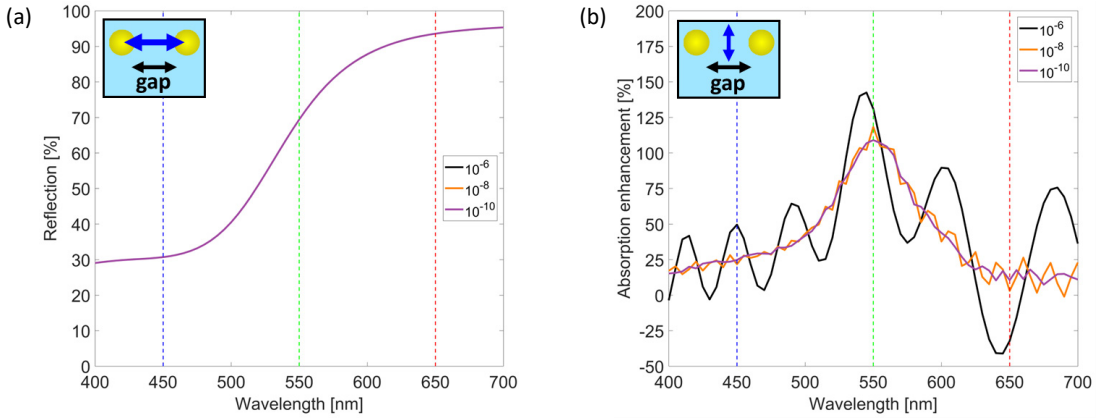

Figure 2-3. Simulated spectra for varying numbers of particles. (a) Reflection spectrum and (b) corresponding absorption enhancement as defined by Equation (2-1).

2.3 Absorption enhancement of few particle systems

Understanding the mechanisms that lead to broadband absorption within the MIM system is essential for improving its performance and translating this concept to other systems. The experimentally fabricated system by Hedayati at al. consists of many randomly arranged gold nanoparticles above a gold mirror layer [56]. Investigations of such large random systems are presented in Section 2.4. Let us however first investigate here the optical response of a few individual particles, which represents the ingredients for the large multi particle systems.

To answer the question what microscopic parameters are most important for strong broadband absorption, the response of a few particles with diameter 5 nm is studied first. This value is in good agreement with Hedayati's mean diameter of approximately 4.5 nm. The particles are embedded in a lossless dielectric medium of refractive index 1.5 and positioned 90 nm above a highly-reflective mirror layer, mostly a 100 nm thick gold layer. The single particles are placed within an arbitrarily sized region of 100 nm periodicity in x- and y-directions to avoid coupling of the periodic regions.

Figure 2-4(a) shows the total absorption of the system for varying numbers of particles atop the gold mirror, while the center-to-center distance of 5.3 nm is kept constant. In the case of 8 particles, the total absorption of the system is also plotted for the case where the gold mirror is replaced by a perfect reflector. In this perfect reflector case, it is obvious that the total absorption corresponds also to the absorption within the particles. The top inset in Figure 2-4(a) show a simplified top view of the modeled system, while the bottom inset shows a side view; the blue arrow indicates the source polarization. The three colored vertical lines are selected wavelengths that represent the primary colors red (λ = 450 nm), green (λ = 550 nm) and blue (λ = 650 nm).

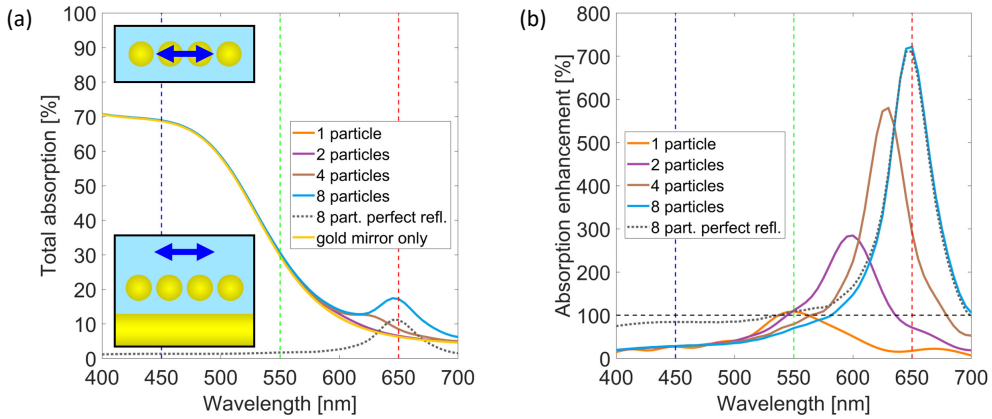

Figure 2-4. Simulated absorption and absorption enhancement spectra for varying numbers of particles. (a) Total absorption for a 3-layer system with varying numbers of particles inside the top layer. (b) Corresponding absorption enhancement of (a).

A simple absorption case is the "no particle"-case with only a gold mirror, where total absorption equals bulk absorption of the 100 nm thick gold layer, and no energy is absorbed elsewhere. In all other cases it is less obvious where light is absorbed. Figure 2-4(b) shows the rescaled absorption within the particles, which is called absorption enhancement and is defined in analogy to the absorption efficiency for the case of isolated particles [1],

$$\text{absorption enhancement } [\%] = A/G \cdot \text{particle absorption } [\%], \tag{2-1}$$

where G denotes the particles' geometrical cross section projected on a plane, i.e. $G = n\pi a^2$ for n spherical particles of radius a and A is the simulation area. Equation (2-1) has the advantage that the calculated absorption enhancement is independent of the somewhat arbitrarily chosen x-y-periodicity. In contrast to the total absorption in Figure 2-4 (a), the absorption enhancement reported in Figure 2-4(b) indicates how much light is absorbed at a specific wavelength within the particles. The particle absorption can be extracted from the simulation by placing transmission detectors before and after the few particles in z-direction. The difference in steady state transmission equals the particle absorption. One can see that the plasmon resonance red-shifts as expected for increasing number of particles in Figure 2-4(b) [31]. One can also observe that the resonance strength dramatically increases and exceeds the geometrically possible absorption by a factor of 7. The enhancement in the blue and cyan parts of the spectrum remains however relatively low and nearly constant.

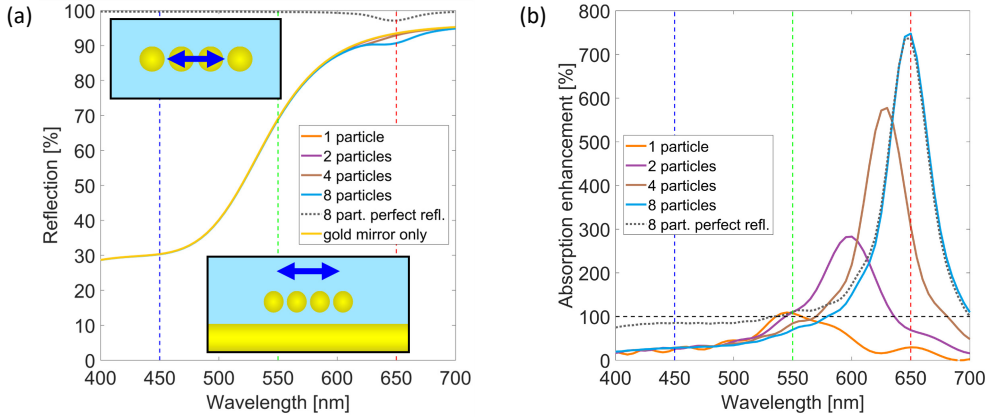

Figure 2-5. Simulated spectra for varying numbers of particles as in Figure 2-4(b), but with 200 nm periodicity. (a) Reflection spectra and (b) corresponding absorption enhancement.

Figure 2-5 demonstrates that the arbitrarily sized simulation region of 100 nm × 100 nm indeed prevents significant coupling of the neighboring periodic particles. The simulations with a 200 nm periodicity in Figure 2-5 exhibit only minor differences when compared with those of 100 nm periodicity in Figure 2-4(b). The comparison thus confirms that the

periodic particle pairs have negligible coupling at 100 nm distance. Note that the larger simulation area is also symbolically visualized in the figure inset by a larger empty area surrounding the four particles. Many experimental parameters influence the absorption enhancement, as will be studied in the next subsections.

2.3.1 Influence of source polarization

The absorption enhancement as defined by Equation (2-1) is highly polarization sensitive. On the one hand, linear polarized light that is incident parallel to the gold particle chain leads to resonances that strongly increase in amplitude and resonance wavelength with increasing number of particles, i.e. clearly red-shifted resonances as reported in Figure 2-5. On the other hand, linear polarized light that it is incident perpendicular to the particle chain leads to modest decrease in amplitude and resonance wavelength with increasing number of particles, i.e. moderately blue-shifted resonances as reported in Figure 2-6(b). Hence, contrary to the parallel case, resonance amplitude and wavelength decrease with increasing number of particles. I must draw attention to a practical issue: the change with increasing number of particles for the directly measurable reflection is so small that it is barely visible in Figure 2-6(a). Yet, the absorption enhancement is noticeable in Figure 2-6(b). In the remainder of this chapter, reflection plots will thus only be provided when they show a clear difference for the evaluated system parameters. Otherwise, only the resulting absorption enhancement will be shown.

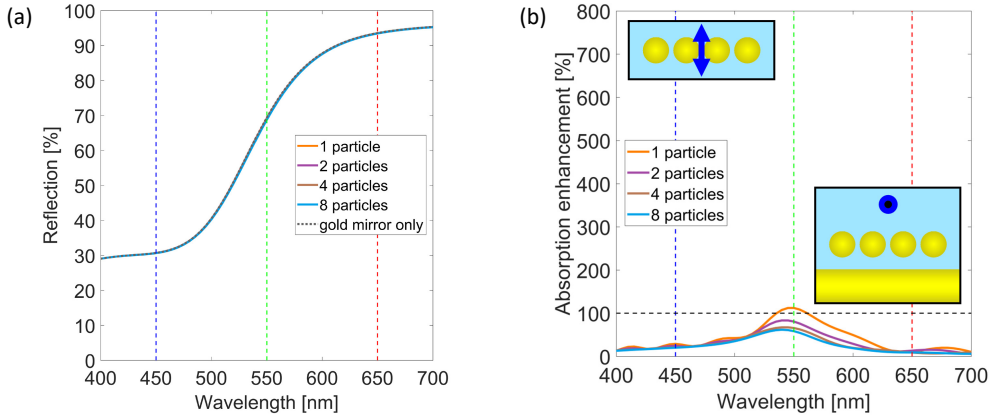

Figure 2-6. Simulated spectra for varying number of particles with a 90° rotated source polarization, compared to Figure 2-5. (a) Reflection spectra and (b) corresponding absorption enhancement.

Both findings agree with the results of Rechberger et al. for significantly larger dimer systems [24]. They showed that this polarization-dependent resonant effect can be understood by picturing a charge or a related spring model. For the case of a single small gold particle, the incident light excites the plasmon resonance of that particle since the electron charges follow the exciting light oscillation [3]. One can also picture this plasmon resonance as the spring constant of an individual particle, see side view in Figure 2-7(a). In the case when two or more particles are sufficiently close, here a few nm, particles' fields couple to each other. For light polarized parallel to the chain, positive and negative charges of neighboring particles face each other, see side view in Figure 2-7(b). This leads to an attractive force between them, which in turn weakens the repulsive force within the two individual particles, thus leading to a stronger resonance with lower resonance energy, viz. longer resonance wavelength. In the spring model, both springs are connected by a third spring that allows both springs to pull together. Note that the third spring constant (or in the plasmon picture the coupling) depends on the distance between particles, as shown in the next section.

For the case of perpendicular polarized light to the particle chain, the positive and negative charges of neighboring particles are aligned to each other, see top view in Figure 2-7(c). This leads to an increased repulsive force between them and within each particle, thus higher resonant frequency, viz. longer resonance wavelength. In the spring model, the forces between opposing charges might also be pictured as diagonal springs. Consequently, one must overcome this

additional restoring force, which results in smaller resonance amplitude and higher resonance energy as confirmed by Figure 2-6(b).

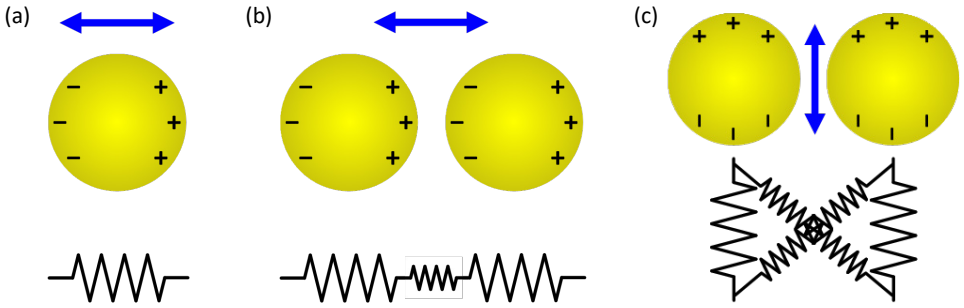

Figure 2-7. Schematic charge distribution and corresponding spring model for (a) a single particle (side view), (b) a dimer illuminated with linear polarized light parallel to the long axis (side view), and (c) a dimer illuminated with linear polarized light perpendicular to it (top view).

Figure 2-8 highlights that this drastic change in absorption behavior with polarization is gradual and is maximized when the light oscillates parallel to the particle chain (0°). The strong polarization dependence will thus lead to a reduced absorption enhancement in the case of illumination with unpolarized light. Nonetheless, the enhancement will still exceed the geometrical absorption by a factor of 3.5 in the case of eight well-aligned particles with a center-to-center distance of 5.3 nm.

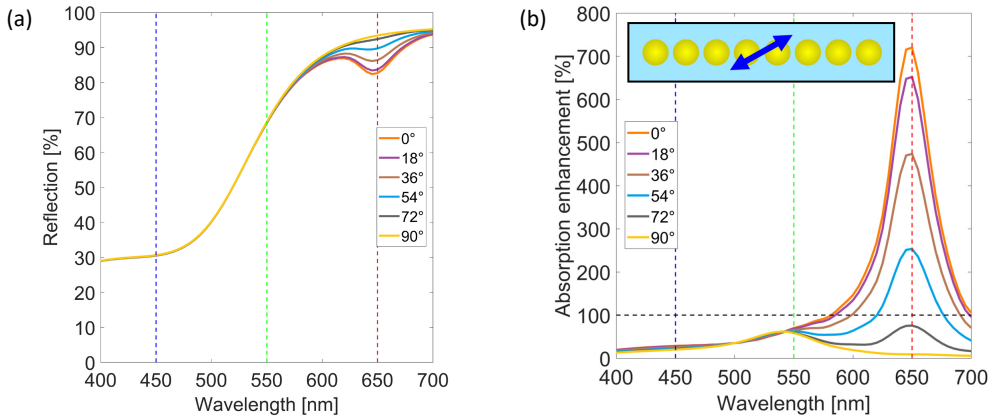

Figure 2-8. Simulated spectra for eight particles with varying illumination polarization. (a) Reflection spectra and (b) corresponding absorption enhancement.

2.3.2 Influence of particle gap size

The study in this section follows the approach of the entire thesis and remains within the limits of a pure classical approach using FDTD despite the very small gap sizes studied. Thus, non-local, electron spilling, or quantum effects are not considered and are beyond the scope of this work [84–88]. The gap dependence for both polarizations is investigated for two extreme cases, a dimer and an infinite chain of particles. The dependence for any finite number of particles should lie in between these two extreme cases. Figure 2-9 shows the dependency for two particles placed 90 nm atop a gold mirror. For linear polarized light parallel to the dimer long axis, the absorption enhancement is maximal in the case of a negative gap and thus overlapping particles, where the absorption maxima is also most red-shifted. Increasing the gap reduces the enhancement and already at a gap of 2 nm, the enhancement is only about 50% stronger than in the case of isolated particles (95 nm gap). This demonstrates that small gaps and overlapping particles are key for strongly enhanced and red-shifted absorption due to near field coupling between the particles. This is in agreement with previous reports that the gap size must be smaller than 10% of the particles diameter to realize strong red-shifts and enhancements [89,90]. For linear polarized light perpendicular to the dimers long axis the behavior is reversed and the absorption enhancement is minimal in the case of a negative gap and thus overlapping particles.

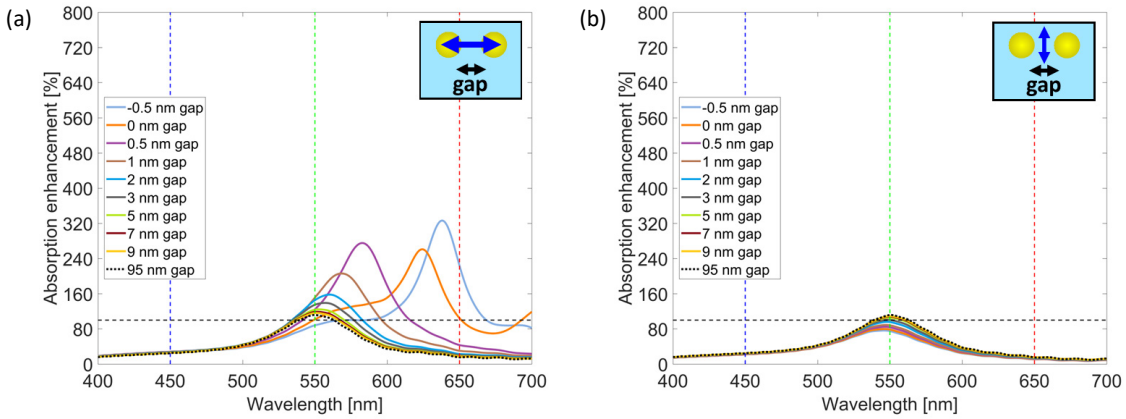

Figure 2-9. Simulated absorption enhancement spectra for dimers with varying gap sizes. (a) Linear polarized light is incident parallel to the dimers long axis and (b) perpendicular to it.

The distance-dependence of the dimers near field coupling is further quantified in analogy to the works by Maier et al. and Downing et al. on spheres and cylinders, respectively [30,91]. To this end, the peak absorption wavelength λ_{res} is determined for each positive gap distance and plotted in Figure 2-10(a) for incident light parallel to the dimers longs axis.

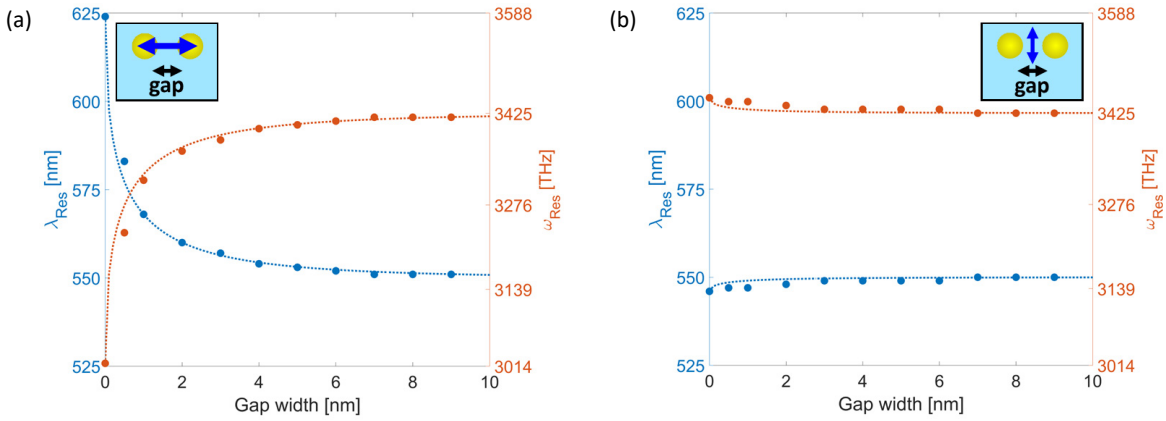

Figure 2-10. Resonance wavelengths and frequencies for dimers with varying gap sizes.
(a) Linear polarized light incident parallel to the dimers long axis and (b) perpendicular to it.

In analogy of the results by Su et al. [92], best agreement for λ_{res} was found for an exponential fit of the following form

$$\lambda_{res} = \lambda_{iso} - (\lambda_{iso} - \lambda_{cont}) \exp\left\{-\sqrt{\frac{g}{\sigma_{gap}}}\right\}, \tag{2-2}$$

where λ_{iso} denotes the resonance wavelength of an isolated particle, λ_{cont} the resonance frequency of particles in contact (0 nm gap size g), and σ_{gap} the interaction decay length. Note that λ_{iso} is determined from the results for a 95 nm large gap, which is a solid approximation since the interaction drops very rapidly (σ_{gap} = 0.5 nm). The second vertical axis shows the corresponding resonance angular frequencies ω_{res}. The corresponding fit is determined in close analogy to Equation (2-2) by replacing the resonance wavelength variables with angular frequency ones,

$$\omega_{res} = \omega_{iso} - (\omega_{iso} - \omega_{cont}) \exp\left\{-\sqrt{\frac{g}{\sigma_{gap}}}\right\}. \tag{2-3}$$

Figure 2-10(a) confirms that the resonance wavelength increases for incident light parallel to the dimers longs axis with decreasing gap size. It also shows that the change in resonance frequency is only significant for very small distances, on the order of a single particle diameter. For a gap size g of 5 nm λ_{res} = 553.1 nm according to the exponential fit, which

differs only by about 1% from λ_{iso} = 550 nm (ω_{iso} = 3425 THz). Figure 2-10(b) reveals that the change in λ_{res} is significantly less prominent for light perpendicular to the dimer longs axis, in agreement with the findings of others [30,91]. The fitted σ_{gap} equals again 0.5 nm and for the largest gap size of 95 nm, i.e. almost isolated particles, λ_{iso} and ω_{iso} agree as they should. This demonstrates that the near field coupling for dimers consisting of two 5 nm sized gold spheres is limited to very short gap distances of about a single diameter. This contrasts with the results for significantly larger dimers, where this coupling occurs for around 2.5 times the diameter [92]. This is likely a result of the dominant absorption efficiency Q_{abs} and the small scattering efficiency Q_{sca} for the small particles used here (Q_{abs} = 38% and Q_{sca} = 0.01% for gold particles with 5 nm diameter in n = 1.5 for a wavelength of 550 nm [7]).

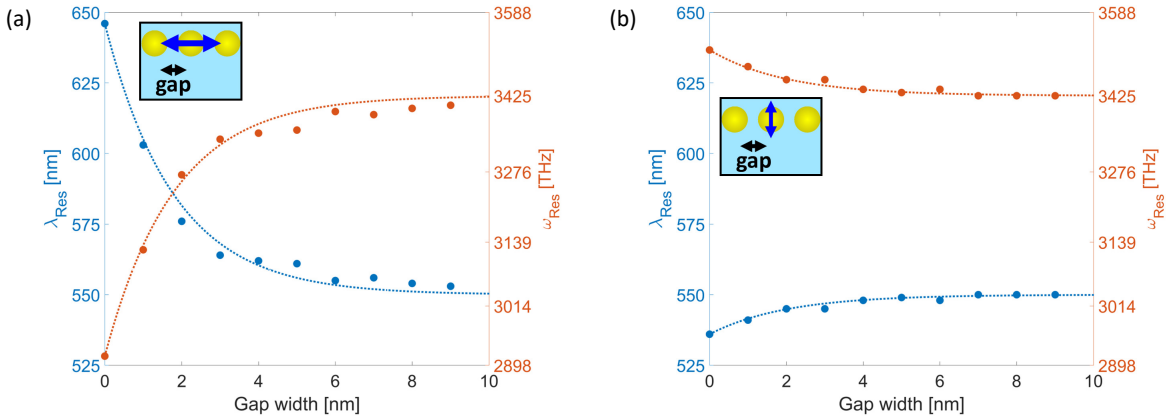

Figure 2-11. Determined resonance wavelengths and frequencies for varying gap sizes of an infinite particle chain. (a) Linear polarized light is incident parallel to the dimers long axis and (b) perpendicular to it.

Figure 2-11 shows that this very short-ranged coupling is also observed for the case of infinite particle chains. By visual comparison of the results in Figure 2-11 and Figure 2-10 it is already evident that the near field coupling is longer-ranged for chains compared to dimers. The following exponential fit for λ_{res}

$$\lambda_{res} = \lambda_{iso} - (\lambda_{iso} - \lambda_{cont}) \exp\left\{-\frac{g}{\sigma_{gap}}\right\}, \tag{2-4}$$

agrees best with the determined peak wavelengths for σ_{gap} equal to 2.0 nm. The fit according to Equation (2-4) differs from Equation (2-2), but evaluating the fit for a gap size of 5 nm confirms that λ_{res} = 557.9 nm is indeed about 1.4% larger than that of isolated particles (λ_{iso} = 550 nm). Nonetheless, there is only negligible coupling beyond the distance of single gold particle diameter. Figure 2-11(a) also reveals that besides slightly slower decay of λ_{res} for light incident parallel to particle chain, the magnitude of the change is also larger, i.e. 96 nm vs. 74 nm. The same is true for light incident perpendicular to particle chain as reported in Figure 2-11(b). The change in λ_{res} is clearly larger compared to the dimer results in Figure 2-10(b). Note that the fit for ω_{res} is determined again in close analogy by replacing the resonance wavelength variables with angular frequency,

$$\omega_{res} = \omega_{iso} - (\omega_{iso} - \omega_{cont}) \exp\left\{-\frac{g}{\sigma_{gap}}\right\}. \tag{2-5}$$

The previous results show that the strong near field coupling decreases drastically over distances smaller than 10 nm. For significantly larger distances one could observe a different kind of distance-dependent interaction between neighboring particles, which is based on plasmonic surface lattice resonances as reviewed by Kravets et al. in 2018 [93]. This type of (diffractive) coherent coupling is usually observed for larger particles and is not present here as revealed by distant-dependent simulations for large distances (between 100 nm and 900 nm) for both polarizations, Figure 2-12.

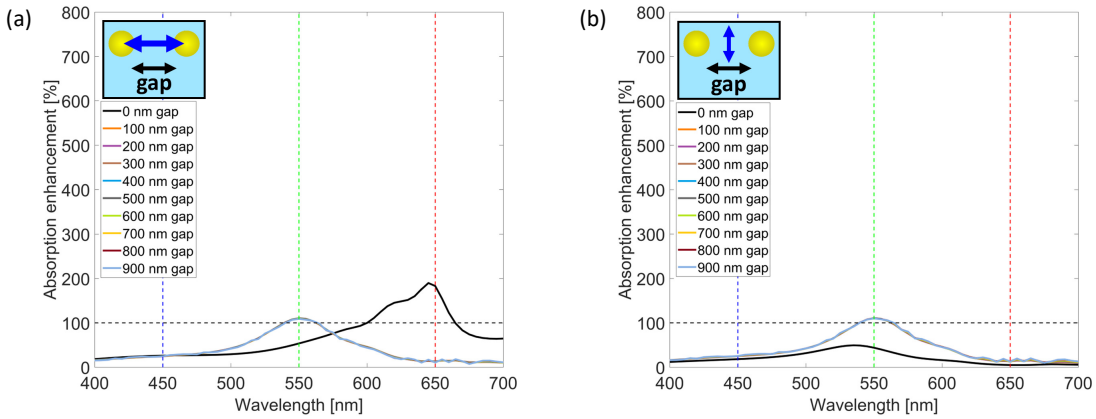

Figure 2-12. Simulated absorption enhancement spectra for varying large gap sizes of infinite particle chains. (a) Linear polarized light is incident parallel to the dimers long axis and (b) perpendicular to it.

The lack of plasmonic surface lattice resonances is attributed to the small scattering efficiency of the 5 nm sized gold particles, which is significantly smaller than 1%, see above. This lack of scattering efficiency prevents (diffractive) coherent coupling for larger spacings.

2.3.3 Role of interference effects

The strong enhancement could be a consequence of two different mechanisms: inter-particle coupling and plasmonic mode coupling of particles with the metallic mirror due to the small distances. The latter was investigated for example by Nordlander and Prodan for the case of a single particle atop a metallic mirror [94]. However, Figure 2-13 shows that the hybridization of the modes is negligible here. The absorption enhancement of 8 particles is nearly symmetric around the mirror distance of 80 nm, for example the absorption enhancements at 70 and 90 nm distances are the same. The range over which it is symmetric varies with the wavelength. Comparing for example the mirror distances 50 nm and 110 nm (80 ± 30 nm) in Figure 2-13 reveals that it is most symmetric around the resonance in the red. This indicates that the strong absorption enhancement is mainly a consequence of enhanced resonances due to interference of the incident light beam with the reflected light beam from the gold mirror. It is maximized at a mirror distance between 90 and 110 nm, where both beams interfere most constructively.

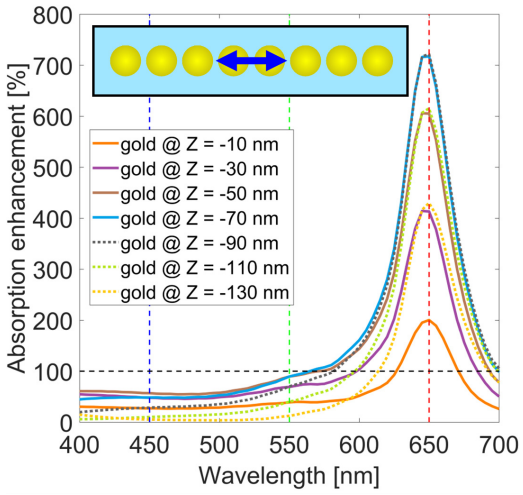

Figure 2-13. Simulated absorption enhancement spectra for varying mirror particle distances (particles @ Z = 0 nm).

Actually, Li et al. realized nearly perfect absorption based on interference with an even simpler MIM system [45]. They used a thin and homogenous chromium layer atop a chromium mirror layer, separated by a 90-100 nm thick SiO_2 spacer layer. They experimentally achieved an average absorption larger than 95% in the VIS and clearly demonstrated that

the high absorption is the result of their manufactured lossy Fabry-Perot cavity. This work was discovered during writing of the article that accompanies this chapter [14] and inspired the work in Chapter 3. Similar absorption performance can also be achieved for embedded systems, even at elevated temperatures [63,65]. Ghobadi et al. showed that one can even increase the bandwidth further by replacing the homogenous top layer with a multi-step one [95], while Ding et al. used two dielectric thin metal layer pairs to broaden and maximize absorption [64]. Both works agree with the finding that interference enhances absorption and in fact, simulations without gold mirror reveal that one needs almost four subsequent layers of 8 particles with a 150 nm spacing in the light propagation direction to reproduce the strong enhancement obtained with a mirror, see Figure 2-14. The lower inset shows a simplified front view of this layered system without a mirror layer.

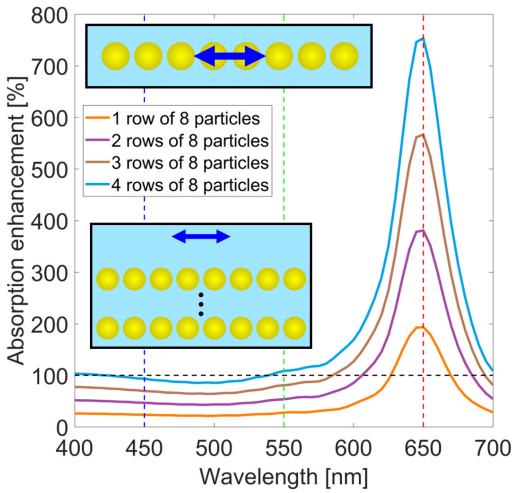

Figure 2-14. Simulated absorption enhancement spectra for varying amount of 8 particle layers.

This is another indication that, in the case of a mirror, two beam interference enhances the intensity by up to a factor of four. Figure 2-15 shows that the intensity is certainly greater than 3 times the incident intensity at the location of 8 particles 90 nm above a perfect reflector. This makes sense despite the small distance of 90 nm, as the perfect reflector leads to a phase change of 180° and the 90 nm spacing to phase changes from 150° @ 650 nm to 216° @ 450 nm. These phase changes add up to almost 360° within the nano-composite layer, which is required for perfect constructive interference. One can thus infer that the enhancement is significantly influenced by lossy Fabry-Perot interference. Note that a similar phase phenomenon has recently been used to build ultrathin planar cavity metasurfaces by Wang et al. [96].

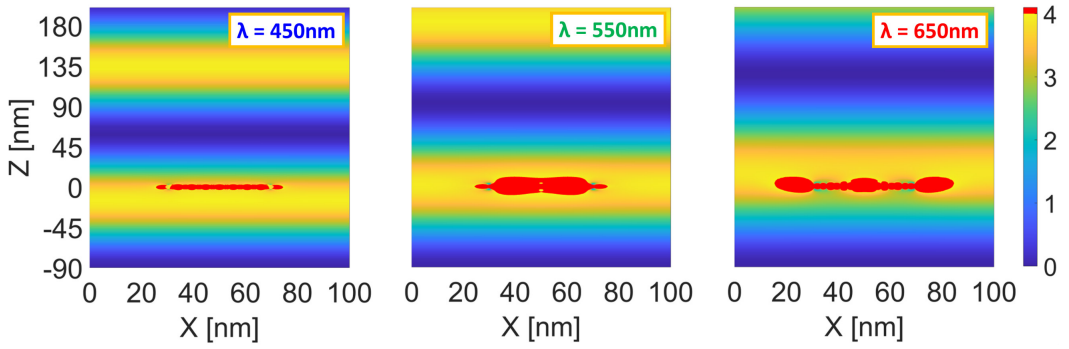

Figure 2-15. Intensity distribution in the X-Z-plane at three different wavelengths λ for 8 gold particles embedded in a semi-infinite dielectric atop a perfect reflector, which is located at Z = -90 nm.

2.3.4 Influence of particle material

The previous results show how absorption can greatly be enhanced in the red part of the spectrum. In Section 2.4 it will also be necessary to increase the absorption in the blue and green parts for the optimization of the many particle systems absorption. To this end, the particle material is first changed to silver and then to aluminum. These materials are selected as their plasmon frequencies are in the blue, respectively UV region of the spectrum [97]. Simulations of a few silver particles' absorption enhancement show significantly increased absorption efficiency in the blue and green, compare the results in Figure 2-16(a) with those in Figure 2-4(b) for gold particles. It is also remarkable that only 8 silver particles with 5.3 nm center-to-center distances within a periodically arranged area of 100 nm × 100 nm achieve an absorption enhancement of almost 100% throughout the whole VIS.

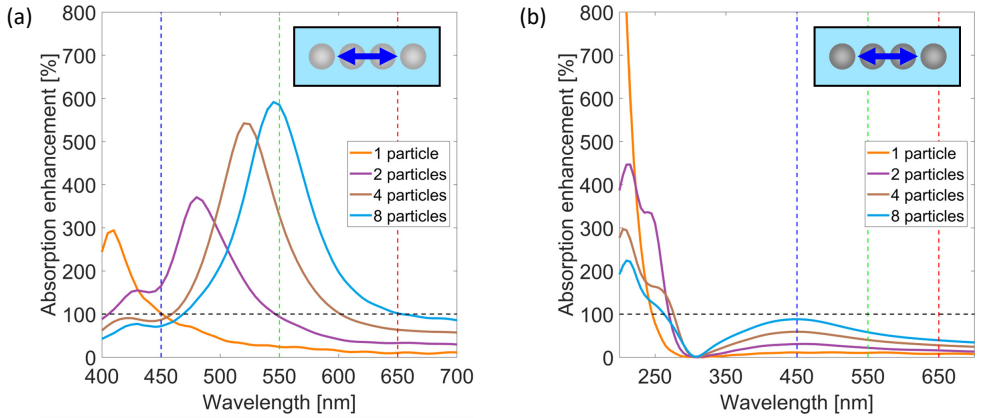

Figure 2-16. Simulated absorption enhancement spectra for two different particle materials atop an aluminum mirror layer. (a) Absorption enhancement of silver particles. (b) Absorption enhancement of aluminum particles.

Figure 2-16(b) shows that in the case of aluminum particles, absorption can be in enhanced in the UV, but significantly less in the blue and green compared to silver. In both cases, absorption in the red region of the spectrum is lower compared to the gold particles case in Figure 2-4(b). One should thus favor these materials for any application, where enhanced absorption at smaller wavelengths is important. Note that aluminum is selected here as mirror layer material to clearly investigate the absorption effects related to the particle material choice and not due to the mirror layer material (compared to aluminum, gold has a reduced reflectivity from UV till the green part of the spectrum).

2.3.5 Influence of dielectric surrounding media

Another mean to change the resonance wavelength and absorption strength is to modify the surrounding medium. Embedding 8 particles in a medium of refractive index differing from 1.5 in the VIS leads to a resonance enhancement with a peak wavelength differing from the initially 650 nm. On one hand, Figure 2-17 reveals that surrounding media with lower refractive indices, i.e. 1.1 and 1.3, will lead to blue-shifted and smaller absorption enhancements. On the other hand, the opposite is true for higher refractive index media, where the peak is red-shifted and the strength even further increased. The combination of any material with high plasmon frequency, such as silver and aluminum, with high refractive index materials seems very promising for optimizing absorption enhancement but is not further explored here.

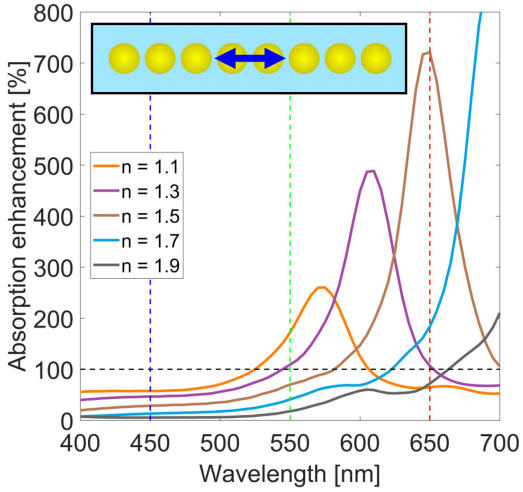

Figure 2-17. Simulated absorption enhancement spectra for 8 particles with varying dielectric surrounding media.

2.3.6 Influence of particle shape

Although manufactured particles at single nanometer length scales tend to be spherical [56,73,76], other shapes are principally possible [5] and can provide possible means to shift the resonance wavelength as an alternative to changing the particle material [89]. Figure 2-18(a) shows the absorption enhancement of a few spherical particles, which was reported in Figure 2-4(b) and is included here for easy comparison with the other results.

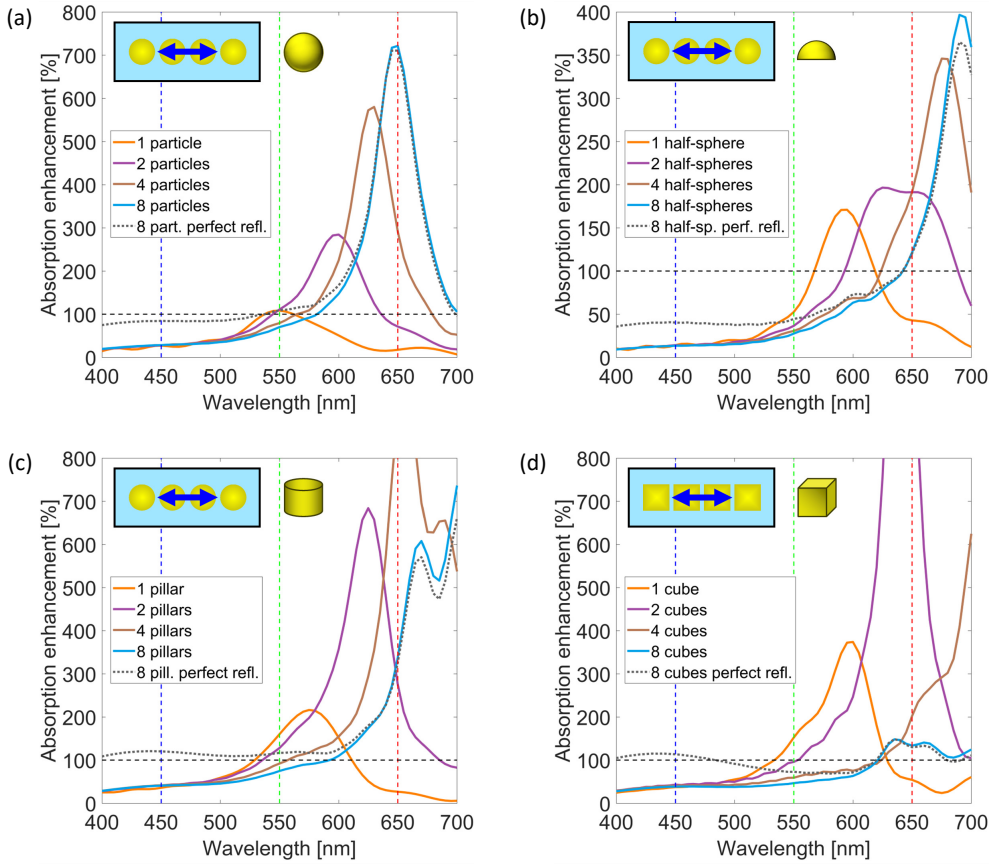

Figure 2-18. Simulated absorption enhancement spectra for varying particle shapes. (a) Absorption enhancement for a 3-layer system with varying number of particles as reported in Figure 2-4(b). (b) Absorption enhancement for hemi-spherical particles. (c) Absorption enhancement for pillar particles. (d) Absorption enhancement for cubic particles.

Figure 2-18(b-d) visualize the absorption enhancement for three possible particle shapes; hemi-spheres, pillars and cubes, accounting in Equation (2-1) for the different geometrical cross sections of these particle shapes. One can conclude from these results that other particle shapes lead to higher amplitudes compared to spherical ones and thus are more efficient for absorption enhancement. Note that this is also true if the data is normalized to the effective particle volumes. For non-spherical particles, one can observe again that increasing the number of particles in a chain aligned with the source polarization leads to a red-shifted and stronger resonance, as in the case for spherical particles. However, the resonance of a single non-spherical particle is already red-shifted compared to the spherical case. Thus, one would need to use different materials to absorb strongly in the VIS, especially in the blue and green parts of the spectrum. Silver and aluminum would be suitable materials as explored in the previous section.

2.4 Absorption of many particle systems

The results in the previous section reveal the absorption enhancement mechanisms for systems containing only a few well-ordered particles, while laboratory samples contain many unordered particles. To simulate the optical performance of these samples, one must include a mean of randomization. The results of three approaches to mimic randomization are visualized in Figure 2-19(a), where a single particle layer of these randomized versions is placed 90 nm atop a gold mirror. The absorption of the gold mirror without particle layer and the case of a purely periodic particle layer with center-to-center distances of 5.3 nm in both directions are also plotted for comparison.

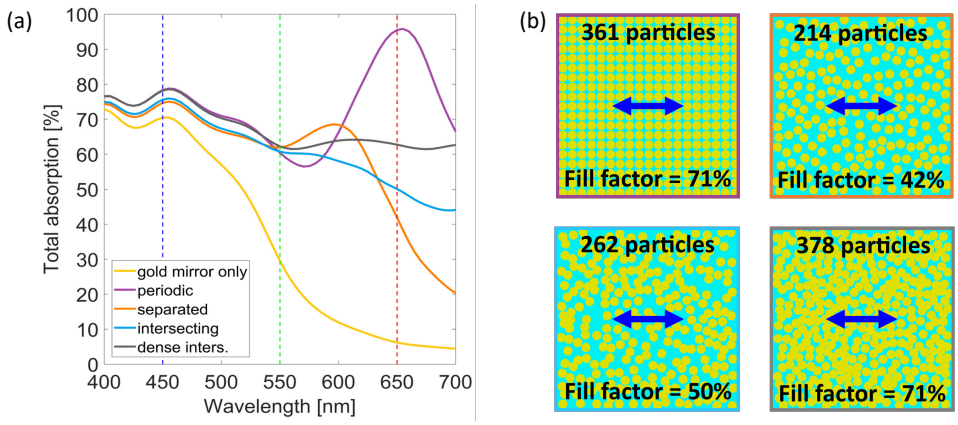

Figure 2-19. Results of periodic and randomly placed gold particles in a single layer atop a gold mirror. (a) Total absorption spectra of these systems. (b) Visualization of the four different particle layers.

Figure 2-19(b) shows simplified top views of the four particle layer systems, where the source polarization is again marked by a blue arrow. The frame color of each top view corresponds to the line color of the absorption plots in Figure 2-19(a). The randomized system with dense intersecting particles shows the most promising performance as the absorption is rather flat across the entire VIS (gray line). In this approach, particles can partially overlap a maximum of 1 nm and are otherwise freely placed with the only restriction that particles are not allowed to cross the periodic boundaries. This system contains in total 378 particles within the periodic area of 100 nm × 100 nm, which corresponds to an area fill factor of about 71%. Both values can be inferred for all four systems from the top view labels in Figure 2-19(b). The system is thus very dense in contrast to the sparse few particle systems in the previous sections, with filling factors in the range of 0.2-1.6%. In the case of a gold mirror, the absorption enhancement as defined by Equation (2-1) even equals total absorption. In all other cases, one can obtain the absorption enhancement by multiplying the total absorption with the inverse filling factor. Therefore, total absorption will be used in this section to measure absorption performance as it can be measured directly without even knowing the filling factor of the system at hand. It is thus an advantageous quantity for the characterization of any experimental realization.

2.4.1 Influence of particle layer distance

The layers containing a few particles were placed at a distance of 90 nm atop the gold mirror as this distance maximized the absorption in case of few particle absorption described in Section 2.3. Figure 2-20(a) confirms that the distance of 90 nm also maximizes absorption in the red for three many particle layers atop a gold mirror. In contrast to the single layer results in Figure 2-19, these three particle layers are stacked with a periodicity of 5.3 nm in vertical direction to further increase total absorption. This periodicity is chosen to avoid additional overlap in z-direction and ensures a strong absorption enhancement due to the resulting small gap size of 0.3 nm in this direction. Note that the distance of 90 nm in z-direction is also ideal in the case of placing the three particle layers atop an aluminum mirror, see Figure 2-20(b). The absorption in the blue part of the VIS is however lowered compared to the gold mirror case, due to reduced substrate absorption in the blue, which is also confirmed in the next section.

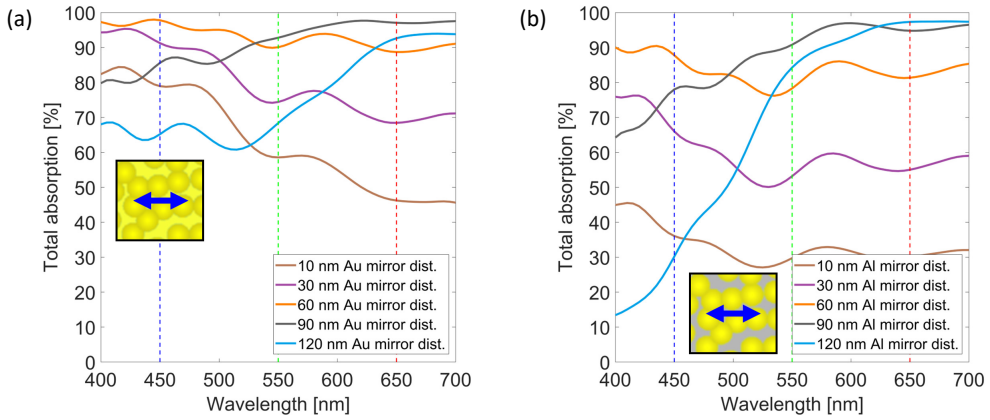

Figure 2-20. Simulated absorption for varying distances of randomly placed gold particles above different mirror materials. (a) Total absorption of gold mirror system. (b) Total absorption of aluminum mirror system.

2.4.2 Influence of amount of particle layers on two mirror materials

Systems with up to four gold particle layers were simulated to study the influence of the amount of particle layers for both mirror materials, gold and aluminum. Figure 2-21(a) shows that both 4-layer systems reach 100% absorption in the red part of the spectrum. The absorption enhancement is thus large enough in this region to reach saturation. However, Figure 2-21(a) also shows that, in agreement with the previous sections, the aluminum mirror system's absorption is lower in the blue and green parts of the spectrum compared to the gold mirror ones.

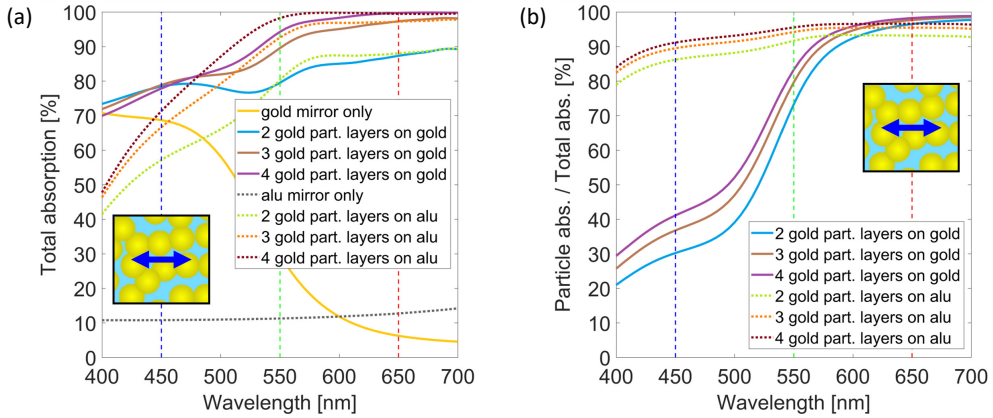

Figure 2-21. Simulated absorption spectra for varying number of particle layers and mirror material. (a) Total absorption of many particle systems. (b) Relative particle absorption of many particle systems.

Still, these systems absorb on average almost equally well, especially above λ = 450 nm. This is certainly unexpected as the bulk absorption of the aluminum layer is significantly lower than that of the gold layer, but can be explained by

investigating where light is absorbed in the system. To this end, detectors are placed at appropriate positions to compute the absorption of the particles and of the mirror separately in analogy to the method used in Section 2.3.

The ratio of particle layer absorption to total absorption is plotted in Figure 2-21(b) and shows that for both mirror materials most energy is absorbed within the particle layers in the red part of the spectrum. However, the situation changes in the green part and is clearly different in the blue part of the spectrum, where particle absorption remains only high for the aluminum case. It is this higher particle absorption that compensates for the lower absorption of the aluminum mirror layer. Replacing the gold layer by an aluminum layer – at little costs in terms of total absorption for the 4-layer case – certainly helps realize the system on an industrial scale [33]. One could even additionally reduce the mirror thickness, since the average transmission across the VIS of a 50 nm thick aluminum layer is already smaller compared to that of a 100 nm thick gold layer.

2.4.3 Enhancing absorption by varying particle materials

The lack in absorption efficiency below 450 nm visible in Figure 2-21(a) might be compensated by a proper particle material choice. Thus, either half or all of the gold particles are replaced by silver or aluminum particles to boost absorption in the blue/green thanks to the aluminum or silver particles' absorption behavior, see also Section 2.3.6. To evidence the improvement provided by such a mixture, systems with 3 particle layers are studied to avoid possible absorption saturation in the red. Figure 2-22(a) shows that mixtures of gold and silver particles (dotted orange line) as well as gold and aluminum particles (dotted dark red line) do indeed absorb more in the blue than the pure gold particle system (gold line). However, the systems containing only silver particles (light blue line), or aluminum particles (gray line) absorb even better than their corresponding mixtures with gold particles.

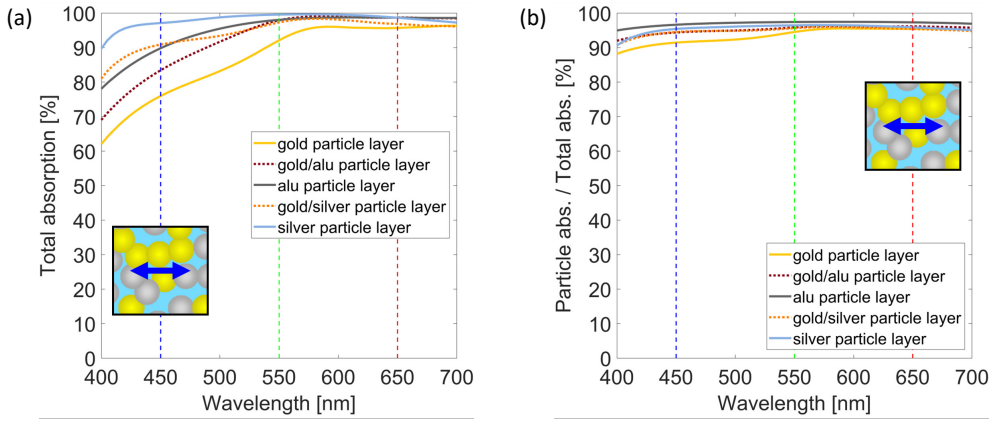

Figure 2-22. Simulated absorption spectra for varying particle material mixtures. (a) Total absorption of many particle systems. (b) Relative particle absorption of many particle systems.

Given that the pure silver particle system absorbs even better in the blue than the pure aluminum system, one can therefore surprisingly conclude that silver with its relatively low bulk absorption is best for maximizing the system's total absorption in the visible part of the spectrum. This is in agreement with Etrich et al. [59], although it might be counterintuitive. It can also be understood by the fact that the silver absorption enhancement results show red-shifted and strongly enhanced absorption with increasing number of particles, see Figure 2-16(a). In Figure 2-22(a), the system is much denser, and thus one can exploit this strong relative absorption enhancement from silver particles to increase also the total absorption to 100%. This exceptionally high absorption is thus a result of plasmonic inter-particle interaction and constructive interference effects with the nano-composite layer of the three-layer system. These two effects, rather than the silver's pure bulk material properties, significantly boost the absorption and result in this unexpected strong absorption behavior.

Independent of the particle material choice, on average more than 93% of the light is absorbed within the particle layer, see Figure 2-22(b). This is in agreement with Li et al., who found that their ratio of thin film to mirror energy dissipation

is larger by more than a factor of 15 for a lossy chromium Fabry-Perot configuration [45]. This shows again the similarity of both systems and the key role played by interference.

2.4.4 Absorption localization

Figure 2-22(b) shows that most of the light is absorbed within the particle layer, but not exactly where it is absorbed. To answer the question of where light is effectively absorbed, the local heat source density is calculated within the particle layers and integrated in z-direction. According to Baffou et al., the local heat source density $q(r_i)$ is defined as [98]:

$$q(r_i) = \omega\, Im(\epsilon)|E_i|^2, \tag{2-6}$$

where ω denotes the frequency, ϵ the total permittivity and $|E_i|^2$ the electric field intensity at the location r_i within the particle. The local heat is a consequence of absorption and the local heat source density $q(r_i)$ is thus an indirect measure of local absorption.

Figure 2-23 shows the averaged $q(r_i)$ in z-direction for gold particles at three specific wavelengths that were marked in the figures above by colored vertical dashed lines. The average heat source density values were normalized to 7000 J / s µm^2 and relative values exceeding one are plotted in red for easy comparison. The value of 7000 J / s µm^2 was empirically optimized to achieve the best visualization contrast, i.e. maximum visibility of the resonance phenomenon at the particle centers and edges. In the case of 3 dense gold particle layers 90 nm above an aluminum mirror layer, one can observe three wavelength-dependent behaviors. In the blue at 450 nm, absorption within the particles is dominated by bulk material absorption and is thus highest in the center of the particles. In the green at 550 nm, one notices a transition from bulk to resonant absorption as edge and gap effects start to play a role. In the red at 650 nm, absorption is almost only determined by resonant effects at the particle edges just beneath their surface.

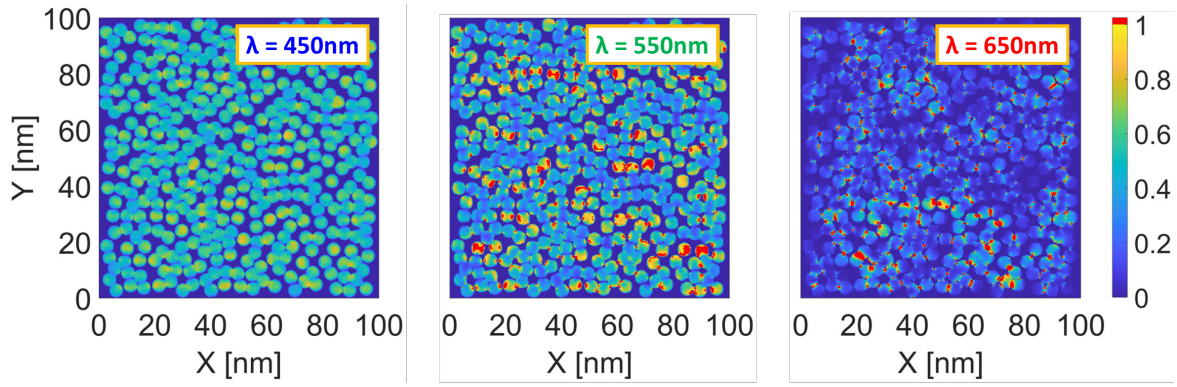

Figure 2-23. Heat source density maps of 3 gold particle layers atop an aluminum mirror, evaluated at 3 different wavelengths λ.

This agrees with the gold particles' absorption enhancement simulations in Section 2.3, which showed reasonable resonant absorption enhancement in the green and strong enhancement in the red. Comparing qualitatively the results of Figure 2-23 with those in Figure 2-4(b) indicates that simulations of relatively simple few particle systems provide some understanding for the microscopic absorption behavior of the much more complex many particle systems.

Figure 2-24 shows that the behavior is quite different in the case of 3 dense silver particle layers floating 90 nm above an aluminum mirror layer. Here, the absorption is determined mainly by resonant effects independent of the wavelength. This is in agreement with the silver particles' absorption enhancement simulations in Figure 2-16(a) that show great absorption enhancement throughout the VIS for varying number of particles.

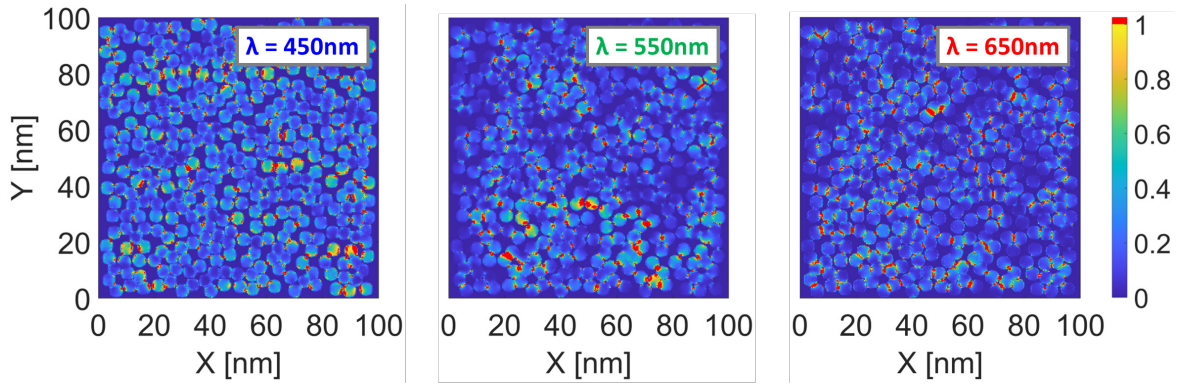

Figure 2-24. Heat source density maps of 3 silver particle layers atop an aluminum mirror, evaluated at 3 different wavelengths λ.

2.4.5 Influence of dielectric surrounding media

The results in Section 2.3.5 revealed that both, the resonances peak wavelength and the absorption strength of a few well-ordered particles 90 nm atop a mirror surface increase with increasing dielectric constant of the surrounding medium. This is in agreement with analytical results of isolated particles [1] and is also observable for many particle systems as Figure 2-25 reveals. The absorption of 3 gold particle layers atop an aluminum mirror also increases in the red part of the spectrum with increasing dielectric constant. There is however no clear peak observable in contrast to the few particle results in Figure 2-17 and the resonance is much broader due to the multi particle interaction as outlined previously. The refractive index of the surrounding medium is thus a useful parameter to locate the broadband absorption besides the particle material composition.

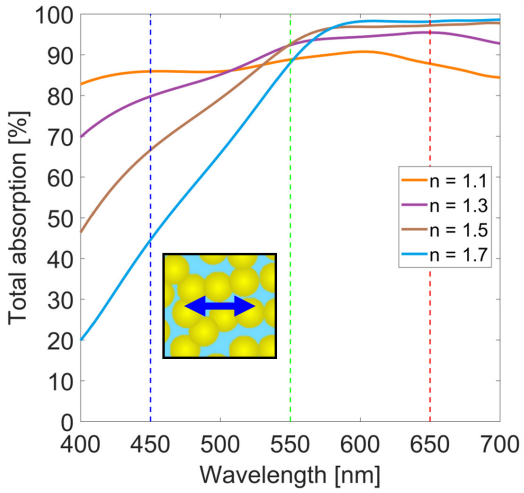

Figure 2-25. Simulated absorption enhancement spectra of 3 gold particle layers with varying dielectric surrounding media.

2.4.6 Optimization of the absorption

Depending on the application, the system reported here may needs to be optimized for peak absorption, bandwidth, angular dependence, polarization sensitivity, or a combination of them. In the case of peak absorption, the system with three random silver particle layers achieves 99.6% at 575 nm as indicated in Figure 2-22. However, the experimental system of Hedayati et al. consisted of gold and achieved 100% absorption [56]. This is not the case for the simulated gold particle system in Figure 2-22 that absorbs “only” 96.3% of the incident light at 695 nm. Especially the absorption in the blue of around 80% is lower compared to 97% measured by Hedayati. The difference to 100% absorption originates from residual reflections.

These residual reflections can be controlled and thus minimized by the following means:

1. Optimizing the spacer layer thickness for the target wavelength band, see Figure 2-13 and Figure 2-20
2. Selecting a different nano-composite metal as reported in Figure 2-16 and Figure 2-22
3. Modifying the filling fraction of the nano-composite layer as confirmed by Figure 2-19
4. Altering the nano-composite layer thickness as revealed by Figure 2-21
5. Varying the index of the surrounding dielectric material as shown in Figure 2-25

In the case of fixed dielectric index and spacer thickness, one can calculate the ideal permittivity ε_{null} of the nano-composite layer for zero reflectivity – thus maximum absorption – as outlined in [66]. Alternatively, one can assume a fixed dielectric and nano-composite index and minimize residual reflections based on the admittance matching method [99,100]. Analysis of the ideal permittivity showed that broadband absorption demands that both real and imaginary parts of the nano-composite permittivity increase monotonically over a large wavelength range. Furthermore, reflection is minimized when the imaginary part of the nano-composite is slightly larger than that of ε_{null}. In this case, the real part of the nano-composites permittivity can differ quite significantly from the ideal one and still result in minimal reflection for the system [66]. Etrich et al. showed in Fig. 4 of Ref. [59] how the monotonic increase of the nano-composite permittivity is enhanced for high metal fill factors close to the percolation threshold. The results in Figure 2-19 indeed confirm that absorption is maximized for dense systems. The angular dependence of the system can be reduced by minimizing the thicknesses for the spacer and the nano-composite layer, thus achieving very small phase changes ($<<\pi$) within those materials [66]. The use of high-refractive index materials for the surrounding dielectric material as well as the spacer material minimizes the phase change for oblique incidence within both layers. This is due to refraction at the interface described by Snell's law [1], which predicts smaller angles within high refractive index materials n_d by

$$\theta_d = \sin^{-1}\left\{\frac{\sin\theta_i}{n_d}\right\}, \tag{2-7}$$

where θ_i is the incident angle in air and θ_d the angle within the dielectric medium. Assuming 45° incident light, the angle within a moderate refractive index material of 1.5 is approximately 28° and within a high refractive index material of 2.4 it is reduced to 17°. For 75° incidence, the corresponding angles are 40° and 24°, respectively. For the case that the randomized system should further absorb relatively independent of polarization, the nano-composite layer should be amorphous and consist only of isotropic ingredients to avoid depolarization effects.

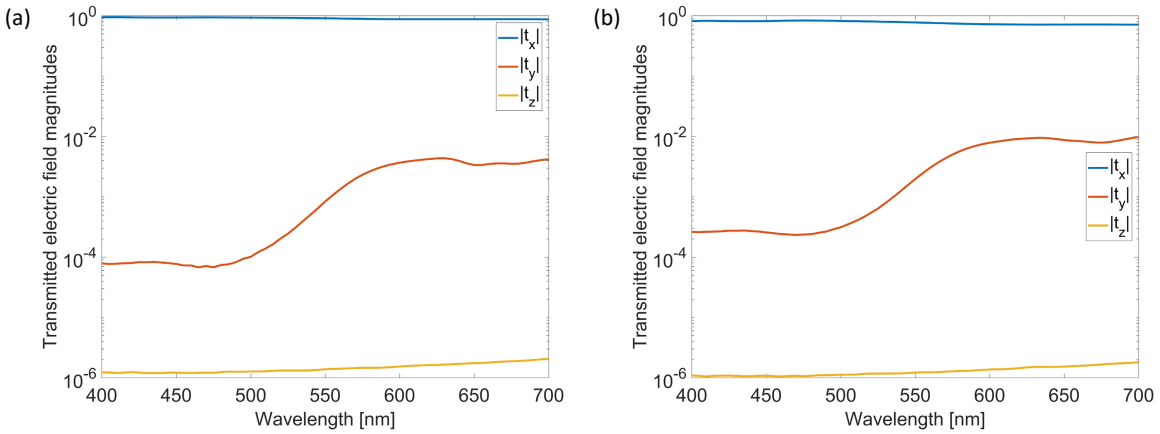

Figure 2-26. Simulated transmissions of the nano-composite layer's electric field magnitudes. (a) Consisting of a single gold nano particle layer and (b) three stacked layers.

This is fulfilled here as confirmed by the evaluation of the transmitted electric field magnitudes in Figure 2-26 for free-standing nano-composite layers (no mirror layer) with a single and three stacked particle layers. The incident field has a magnitude of one and is polarized in x-direction. The magnitude of the transmitted field in x-direction is on average more than two orders of magnitude higher than that in the two other directions. Thus, no significant depolarization in the nano-composite layer is observed, in agreement with systems analyzed by Etrich et al. [59].

2.4.7 Approximation of the nano-composite system with effective medium models

Optimizing the system for high absorption can be achieved by varying the different parameters in the system and computing its optical response, e.g. using FDTD. Unfortunately, this approach is extremely numerically intensive. A simplified approach consists in simulating transmission and reflection spectra for the pure nano-composite layer to extract its permittivity, which can then be used in numerically less-intensive transfer matrix calculations [59]. However, this simplified approach is still quite numerically intensive since it must be performed for any variation of the nano-composite layer, i.e. thickness, nano-composite metal or fill factor.

An alternative is to calculate its permittivity based on effective medium theories, which can predict the permittivity in milliseconds rather than hours or days for a full FDTD simulation with appropriate randomization of the nanoparticles. Two commonly used effective medium theories for this purpose are the Maxwell Garnett and Bruggemans methods [1,101–104]. In this section, they are applied to the investigated perfect absorber system. The Maxwell-Garnett theory was derived for spherical inclusions in a host material [101] and the Bruggeman theory for two component mixtures [102], where one cannot distinguish any inclusions. The many particle systems investigated in this chapter do not satisfy the assumption of either theory as the particles can partially overlap and thus are neither true inclusions nor a completely randomly inhomogeneous medium [1]. In the case of Maxwell Garnet the effective ε_{eff} is implicitly defined by

$$\frac{\varepsilon_{eff}-\varepsilon_d}{\varepsilon_{eff}+2\varepsilon_d}-f_m\frac{\varepsilon_m-\varepsilon_d}{\varepsilon_m+2\varepsilon_d}=0, \tag{2-8}$$

where ε_m is the metal permittivity, ε_d the dielectric permittivity, and f_m the metal filling fraction [59]. Maxwell Garnett theory is derived for inclusions in a host material and Equation (2-8) is only valid for metal inclusions in a dielectric host. For the case of dielectric inclusions in a metal, one must substitute ε_m with ε_d and calculate the dielectric fill factor. In the case of Bruggeman [1], ε_{eff} can be calculated according to

$$f_m\frac{\varepsilon_d-\varepsilon_{eff}}{\varepsilon_d+2\varepsilon_{eff}}+(1-f_m)\frac{\varepsilon_m-\varepsilon_{eff}}{\varepsilon_m+2\varepsilon_{eff}}=0. \tag{2-9}$$

Note that the explicit choice of the metal filling fraction f_m in Equation (2-9) is arbitrary since substituting ε_m with ε_d and then using the dielectric fill factor is possible due to the symmetry of the equation. Explicit formulas for the effective permittivity are available in References [1] and [66], respectively. Both equations are solved numerically with Matlab scripts using ε_d = 2.25 (n = 1.5) and the permittivity of gold as determined by Johnson and Christy [105]. The original many particle layer shown in Figure 2-27(a) can then be replaced by a homogeneous slab with the corresponding effective permittivity, Figure 2-27(b).

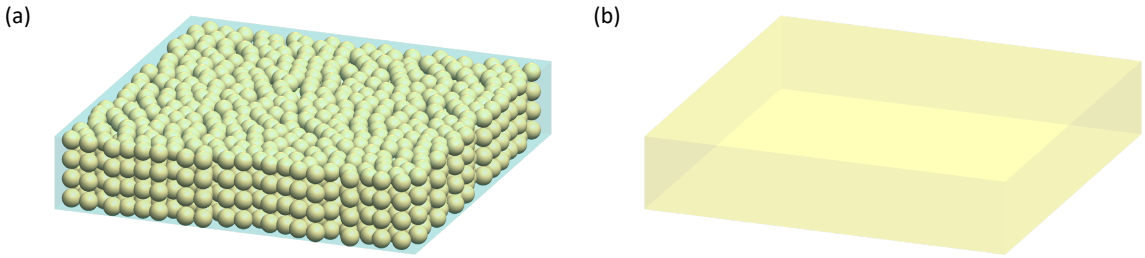

Figure 2-27. Schematic visualizations of the modelled nano-composite layer. (a) Original many particle layer and (b) simplified homogenous layer based on effective medium theory.

This simplified system is then simulated using Lumerical FDTD, although simpler methods such as the transfer matrix method are equally well-suited to simulate reflection in stratified media. Figure 2-28(b) shows the simulated absorption spectra based on the Maxwell Garnett method for varying metal filling fractions of 0.47, 0.28, and 0.50 corresponding to periodic, separated, and dense intersecting arrangement, respectively. Note that these metal filling fractions differ from the areal ones provided in Figure 2-19(b). Comparing the absorption spectra in Figure 2-28(b) based on Maxwell Garnett theory with the results of the original system reported in Figure 2-19(a), one notices that there is good agreement in the blue and turquoise parts of the spectrum.

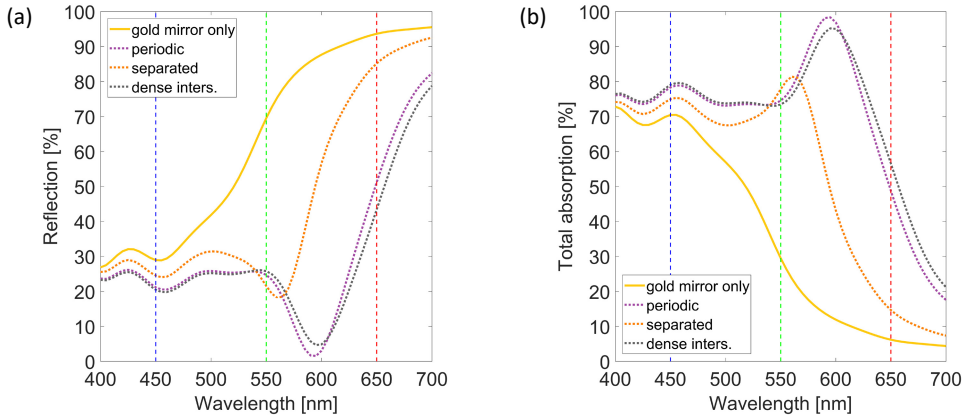

Figure 2-28. Single effective medium layer atop a gold mirror based on Maxwell Garnett theory. (a) Reflection spectra and (b) total absorption spectra of these systems with line colors according to the original model in Figure 2-19(a).

However, the agreement is only modest in the green part and rather poor in the red part of the spectrum. This is most prominent for the overlapping systems with intersecting and dense intersecting particles. The agreement is reasonable, where near field interaction within the nano-composite layer is weak according to the results for few particle systems in Section 2.3. The flat and strong absorption in the red, especially by the dense particle system, is however not observed with Maxwell Garnett theory. This is understandable since Maxwell Garnet theory was not derived for overlapping particles.

The total absorption spectra based on Bruggeman's theory in Figure 2-29(b) also agree with the simulation results of the original model in Figure 2-19(a) in the blue and turquoise spectral ranges. For longer wavelengths, the behavior is quite different and flat spectra are predicted for all three metal filling fractions and these three plateaus differ only modestly from each other. This is in great contrast to the original calculations, where the periodic and separated nano particle arrangements exhibited clear absorption peaks, see Figure 2-19(a). Furthermore, in the green and red parts of the spectrum, the absorption based on Bruggeman's effective medium layer is significantly lower than in the original calculations. In summary, it is not possible to adequately predict the absorption behavior for the many particle systems based on effective medium theories. The study of many particle systems requires modelling of the complete physical system to predict the strong and flat absorption that is in agreement with the experimentally measured data in [56]. This is also in good agreement with the work of others [59,66].

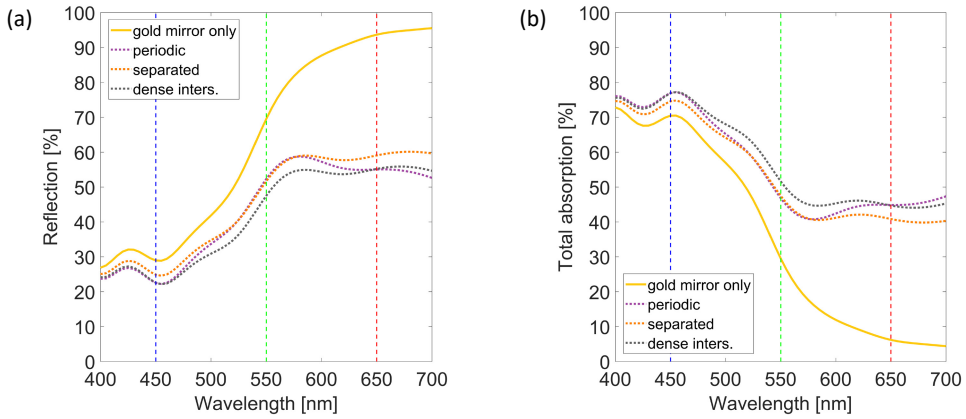

Figure 2-29. Single effective medium layer atop a gold mirror based on Bruggeman theory. (a) Reflection spectra and (b) total absorption spectra of these systems with line colors according to the original model in Figure 2-19(a).

2.5 Conclusion

The optical response of MIM systems with a top nano-composite layer and different mirror materials, particle materials and dielectric spacer thicknesses was investigated in this chapter. It was demonstrated that small gaps and overlapping particles are required for strong resonance enhancements within the nano-composite layer. In agreement with the findings of others, the resonance is red-shifted and strongly enhanced with increasing number of particles. The data indicate that the distance of the composite layer to the mirror layer is of key importance as the MIM's high and broad-band absorption is a consequence of lossy Fabry-Perot interference rather than a pure plasmonic effect. Consequently, interference strength can be maximized with highly reflecting mirror materials. Hence, systems with an aluminum mirror layer can maximize absorption, although one would guess the opposite effect because of aluminums high reflectivity. Other highly reflecting materials would be equally suitable for that purpose.

Most of the light is resonantly absorbed within the particles, just beneath their surface. Thus, one can tune the absorption behavior as shown here by modifying particle material, size, or density. These results demonstrate the flexibility and versatility of MIM systems to absorb light efficiently over specific wavelength bands and the guidelines provided can assist in realizing functionalities that require near-perfect absorption over specific wavelength bands. Any application that demands a near perfect optical absorption across a large band can benefit from this design freedom.

2.5.1 Comments on industrial scalability

The whole system could be manufactured on flexible foils in a single roll-to-roll vacuum coater with two evaporation sources that can be controlled independently. It would require three successive runs through the machine to evaporate first the nano-composite layer, second the dielectric spacer and, finally, the aluminum mirror layer. Of course, the order could be changed depending on whether or not one intends to view the effect through the foil or not. In the latter case, one must apply an additional overcoating to provide the assumed refractive index of 1.5 here, which can be achieved with almost any polymer material.

Thus, industrialization of the system seems to be straightforward. However, co-evaporating a conducting (e.g. aluminum) and insulating material (e.g. SiO_2) simultaneously is challenging for at least three reasons:

1. The required oxygen for the SiO_2 formation can oxidize conducting materials such as aluminum or silver.
2. Realizing the system with gold as conducting and inert material avoids this issue, but can still contaminate the evaporation source of the insulating material (and vice versa).

3. It is challenging to simultaneously control all parameters such as partial gas pressure, two evaporation rates, etc.

These challenges can be fully avoided by replacing the top nano-composite layer with a homogenous layer such as chromium. This was already demonstrated by Li et al. in 2015 and will be explored in the next chapter for engineering transmission [45].

2.5.2 Possible Applications

The researched MIM system has almost perfect absorption, which is nearly independent of the incident angle [56]. It can principally be applied on any surface that either fits in an evacuation chamber or by a suitable transfer process. In the case when the system is coated on a transfer foil as outlined above, the MIM system can be transferred to almost any surface by hot stamping, cold stamping, lamination or even injection molding. This variety of available processes facilitate the MIM system finding applications in the following fields:

- Warm water generation or thermal solar cells due to high absorption and low heat resistance (thin layers)
- Stray light prevention, e.g. in optical instruments or experimental setups like holography
- Heat management by adapting the system to infrared, e.g. for layers on window glasses
- Replacement of black anodizing to avoid using the involved chemicals for electrochemistry
- Light blocking layer on blackout curtains
- Thermal camouflage for military applications
- Improved space blanket by using the foil as it is, absorbing black outside reflecting aluminum inside

This list is certainly not comprehensive, but highlights that many applications with a requirement on strong absorption could benefit from this MIM system.

Chapter 3 Engineering multi-state transparency of MIM systems

The results in this chapter are inspired by the work of Li et al. [45] that was discovered during the preparation of the manuscript related to the results in Chapter 2 [14]. These authors describe a MIM system that contains only homogenous layers: top and mirror chromium as well as a glass (SiO_2) spacer layer, see Figure 3-1(a). This leads to a perfect black appearance, see Figure 3-1(c), due to broadband destructive interference resulting from the very thin SiO_2 spacer layer. This represents a drastic simplification of the system in Chapter 2 that contained a nano-composite top layer, by replacing the nano-composite layer with a homogenous chromium layer. Their results indicate that despite the simplification, broadband absorption with similar performance can be achieved, comparing Figure 3-1 and Figure 2-1. This chapter is also an extended version of a publication [106] with additional content on the used methodology and details of the system parameters. In analogy to Chapter 2, comments on the possibility to manufacture this system on an industrial scale are presented in Section 3.6.1.

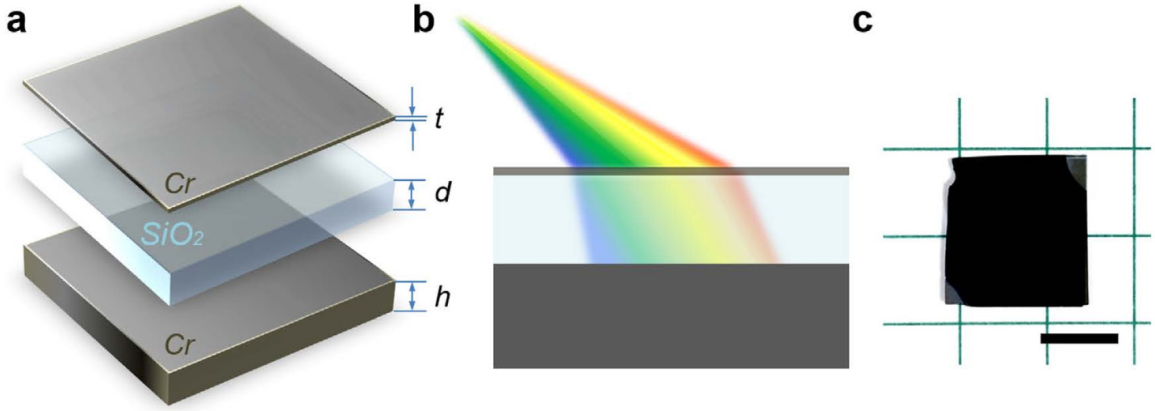

Figure 3-1. Visualization and realization of a strongly absorbing MIM system realized by Li et al. [45]. (a) Schematic diagram of the Cr-SiO_2-Cr tri-layer thin film stack. The geometrical parameters are: t= 3 nm, d= 95 nm, and h = 100 nm. (b) Schematic of perfect absorption for oblique broadband illumination of visible light. (c) Optical image of $CrSiO_2Cr$ sample, revealing totally black color in contrast with background notebook. The length of scale bar is 1 cm. Figure and sub-captions reproduced with permission (CC BY).

The objective of this chapter is to show how the system shown in Figure 3-1 is modified and optimized to fabricate a MIM system that is similarly black, but contains a high reflective aluminum mirror layer rather than a medium reflective chromium one. The resulting black state can be switched by pulsed laser processing to a mirror-like and/or partial or full transparent state. The choice of aluminum is motivated by the about twice higher reflection of aluminum compared to chromium; it could also be chemically structured as alternative method to the optothermal one presented here. The optical state of a material is important as it does not only affect its visual appearance, but also determines possible applications for that material. For example, maximizing optical absorption enables many applications, including sensing, photodetection, steam generation, as well as enhancement of solar cell efficiencies [52,95,107,108]. On the other hand, maximizing reflection is essential for optical mirrors, cavities or diffractive elements [109–112], while high transmission is required for any see-through application such as smart windows or displays [113–118]. Engineering optical absorption and reflectance have been – and still are – extensively researched, but the realization of a transparent state from an initially highly absorbing state is considered novel. All these states are accessible with this MIM system.

Further, applications may demand additionally switching from one optical state to another, e.g. from diffuse reflection to strong absorption as in most printing, sensing or data storage applications [119,120]. The MIM system even allows

for the realization of multiple states and thus even multi-state printing is feasible that can be used for very advanced QR codes [121]. All these applications can highly benefit from the laser processing methodology presented in this chapter.

The latter application is realized in Section 3.5 by multi-state printing of a large area three-dimensional (3D) art image. Note that the used printing strategy here transforms/switches the metallic parts of the MIM system rather than drying and/or applying an ink. This switching is realized with a resolution of about 508 dpi as 50 micron sized laser spots are utilized, but can be increased to the level of single micron as works by others have shown for simpler systems, as discussed in Section 3.1.

Section 3.2 provides a description of all experimental and numerical methods used to manufacture, measure, and simulate the system. The optical mechanism that allows for strong and broadband absorption as well as the corresponding system optimization are discussed in Section 0. This broadband absorption of the system leads to an initially black state, which can be modified/switched by laser processing as shown in Section 3.4. This section also reveals, which parameter influences the switching of this state and a process window is determined for two different types of substrates. This laser process is then applied to the realization of multi-state printing of a large area 3D art image in Section 3.5, before the findings are summarized in the final Section 3.6, where also the possibility to manufacture the system on an industrial scale is discussed.

3.1 State-of-the-art in optical appearance switching

Any application that demands switching of optical properties, e.g. printing, needs means to supply this functionality. For this process, one could conventionally apply, with possible additional curing, ink on a substrate. Alternatively, one could erase part of a homogenously colored medium with an applied solvent, heat, electricity, or laser energy [122]. The latter is used in the following sections to realize and explore the limits of multi-state printing with an initially homogenously black appearing MIM system.

Most laser processing publications focus on the modification of single-layer systems. Zywietz et al. showed that silicon spheres can be deposited locally from a homogenous donor silicon layer by focused femtosecond laser pulses [18]. Their size can be controlled by the laser energy, affecting the color produced by their strong electric and magnetic dipole resonances, thus enabling printing in the submicron range. Mao et al. focused a green continuous wave laser with a high numerical aperture objective to locally create gold nanoparticles from a continuous, 12 nm thick, gold film [123]. At the focal spot, the gold film is liquefied and forms nanoparticles that exhibit plasmonic resonances with a colorful optical response different from the original gold film. Microscopic observations revealed that it is possible with this method to print legible text with a height of a single micron. Guay et al. proved that one could even directly modify the color of silver coin surfaces with large topography variations by varying the laser fluences of a nanosecond pulsed laser [124]. They used a single- and multi-pulse strategy to create vivid colors and observed that multiple pulses in burst mode can broaden the achievable color gamut. Odintsova et al. demonstrated in 2019 similar decorative results by modification of polished bulk substrates for jewelry applications, by varying the intensity and number of nanosecond laser pulses [125].

This previous art shows that single-layer modification works for a plurality of laser sources and metal combinations and can also be applied to alter the top layer of multi-layer systems [19,21,44,113]. However, the research focus has always been on switching the local appearance of areas by modifying initially colorful or metallic surfaces in a binary way, i.e. switching from one reflective state to another. In this chapter, the appearance of an initially black MIM system is modified in a gradual way. The system appears initially black, viz. not colorful, and is transformed, respectively tuned, gradually to a plurality of reflection and transmission states. It thus goes beyond the current state-of-the-art in optical appearance switching.

3.2 Methodology

The following methods are used throughout this chapter to manufacture the researched MIM systems by multiple layer evaporation before they can be analyzed spectroscopically. The spectroscopic measurements are then compared to simulations and both are combined to reveal where light is absorbed and perform systematic parameter studies.

3.2.1 Layer evaporation

The chromium and aluminum layers were evaporated with a Leybold Heraeus L560 by electron-beam evaporation, see Figure 3-2(a). For the deposition of aluminum, the chamber was evacuated to a pressure of 3.5×10^{-5} mbar and the deposition rate was adjusted to 0.4-0.8 nm/s. The chromium evaporation was executed at a pressure of 3.5×10^{-5} mbar and the deposition rate was set to 0.2-0.3 nm/s. The MgF_2 spacer layer was applied by thermal evaporation with a Tectra GmbH Mini-Coater at a pressure of 2×10^{-5} mbar, see Figure 3-2(b), and a deposition rate in the range of 0.8-1.2 nm/s.

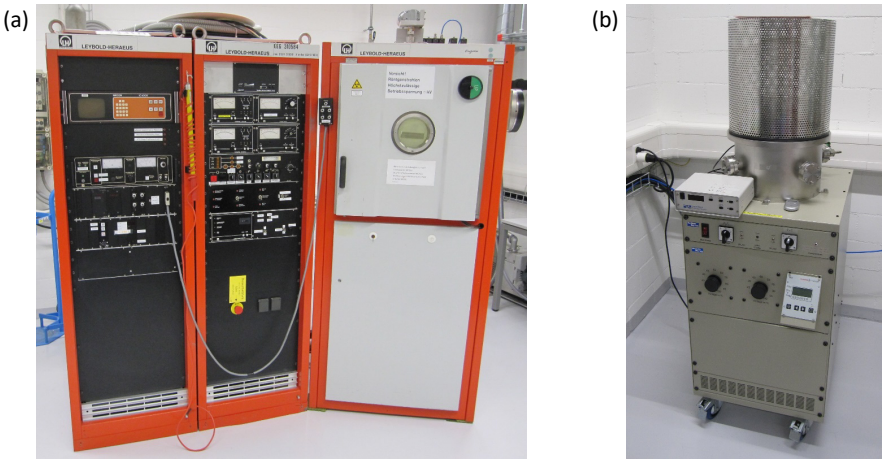

Figure 3-2. Photographs of the used evaporation equipment. (a) Electron-beam evaporator Leybold Heraeus L560. (b) Thermal evaporator Tectra GmbH Mini-Coater.

3.2.2 Spectral measurements

An Avatec ULS3648-USB2 spectrometer in combination with the reflection probe FCR-7UVIR200-2-ME and the broadband light source Thorlabs SLS201/M was used for all spectroscopic reflection measurements in direct reflection, see Figure 3-3.

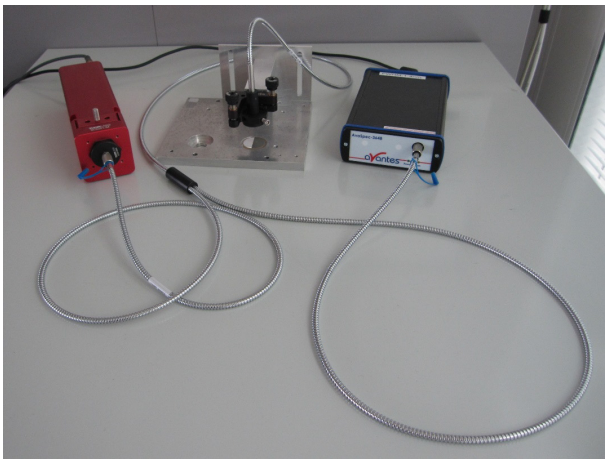

Figure 3-3. Photograph of the used spectroscopic equipment.

Sample transmission was not measured since the MIM system is optically opaque due to the thick aluminum bottom layer as outlined below. The measured absorption spectra thus can be calculated by

$$\text{absorption [\%]} = 100\% - \text{reflection [\%]}. \tag{3-1}$$

For spectral measurements with obliquely incident illumination, the ellipsometer SEMILAB SE-2000 was used. The optional photometry option was not available and thus the raw signals for unpolarized light were measured for the reflection from the sample and from an aluminum reference mirror at the same incidence angle. The reflection for the sample R_{sample} was subsequently obtained by means of the photometry method as outlined in the user's manual by

$$R_{\text{sample}} = I_{\text{sample}}\, R_{\text{ref}} \,/\, I_{\text{ref}}\,, \tag{3-2}$$

where R_{ref} is the reflection of the aluminum reference mirror, I_{ref} its corresponding raw signal and I_{sample} the sample's raw signal. Note that R_{ref} was obtained by computing the unpolarized reflection of a semi-infinite aluminum mirror with Lumerical FDTD for each incidence angle using material data by Rakić [83,126].

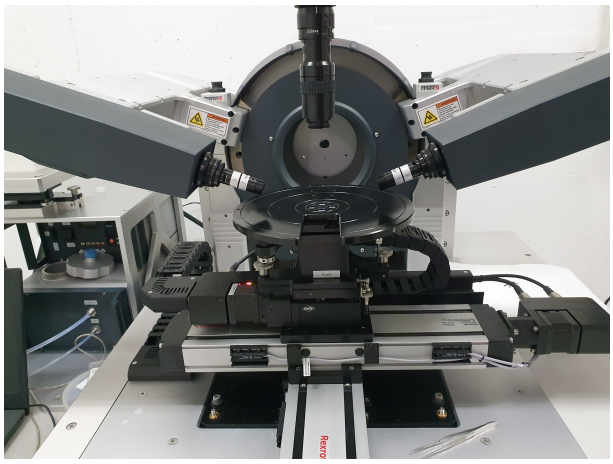

Figure 3-4. Photograph of the used ellipsometer SEMILAB SE-2000.

3.2.3 Simulations

The spectral simulations were performed with Lumerical FDTD [83]. A linearly polarized broadband source from λ = 350 nm to 1100 nm was used to illuminate the MIM system. The simulation region of 10 nm × 10 nm × 2000 nm uses a conformal meshing of variant 1 with an accuracy of 5. The first parameter assures that all simulated elements are modelled conformal to avoid stair-case effects. The accuracy of 5 ensures that the mesh is fine enough for this approach by creating a mesh, which is finer than λ/22 (2 + 4 × accuracy). Bloch-type periodic boundary conditions were selected laterally and perfect matching layers with 32 layers in z-direction. Figure 3-5 visualizes the system and effect of the periodic boundary conditions by rendering the periodically repeated areas with an increased transparency. Note that the visualization is cut after a single period, while the simulation extends infinitely in x-y-directions and the transparency of the chromium layer is also constant.

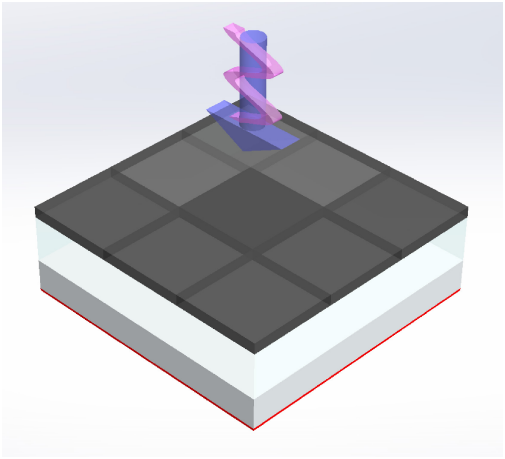

Figure 3-5. Schematical visualization of the simulated MIM system.

The mesh in and close to the chromium and MgF_2 layer was overwritten to a maximum size of 2 nm × 2 nm × 0.25 nm, mainly to ensure accurate resembling of the layer dimensions in axial direction. Power detectors were placed at appropriate positions in accordance with the recommendations by Lumerical to achieve the highest possible accuracy in reflection and absorption detection, for example the reflection detector is placed in front of the source to minimize scattering. The material data of aluminum, chromium and MgF_2 are based on literature values [126–128]. The main parameters are summarized in Table 3-1 below.

Parameter	Value
FDTD-simulation region	10 nm × 10 nm × 2000 nm
Boundary conditions	Bloch in X- and Y-direction. Perfect matching layer PML with 32 layers in z-direction
Mesh type, refinement, and accuracy	Auto non-uniform, conformal variant 1 and level 5
Time step and minimum mesh size	dt stability factor 0.99 and 0.25 nm
Source	Linear polarized light in the X-Z-plane with bandwidth 350-1100 nm. Injected at z = -800 nm with unit amplitude
Frequency domain power monitors	Transmission is recorded at z = 700 nm Reflection is recorded at z = -700 nm by subtracting the source's field from the measured one (most accurate)
Material parameters	Al (Aluminum) Rakic with 6 coefficients Cr (Chromium) Lozanova with 6 coefficients MgF_2 (magnesium fluoride) Marcos with 5 coefficients Metals with 0.01 fit tolerance, MgF_2 with 0.001
Dielectric background and spacer	Constant values of 1.0 and 1.5, respectively
Early Shutoff	1E-5

Table 3-1. Summary of relevant simulation parameters.

3.3 Optimization and manufacturing of the black MIM system

The MIM system used for all experiments in this chapter is schematically shown in Figure 3-6. It is a three-layer stack of homogenous materials: chromium Cr, magnesium fluoride MgF_2 and aluminum Al. All three layers are directly vacuum coated on transparent substrates (either glass or foil) as described in Section 3.2.1; they could also be applied indirectly via e.g. a hot stamping foil [129]. Typically this special MIM type, a lossy Fabry-Perot layer stack embedded in air, consists of a partially transparent absorber layer, a transparent dielectric spacer layer and an opaque mirror layer [28]. It can absorb part of the incoming light in the VIS based on a lossy Fabry-Perot interference effect.

3.3.1 Optical functions of the MIM layers

The partial transparency of the absorber layer ensures that the incoming light is partially transmitted, reflected and absorbed in appropriate portions. The transmitted fraction is reflected at the bottom mirror layer before it hits again the top chromium layer, where a fraction of this light is again transmitted, reflected, and absorbed. These multi reflections and transmissions lead to a multi beam interference phenomenon as sketched in Figure 3-6, resulting in nearly perfect destructive interference over the entire VIS for thin dielectric spacer layers as shown below. This requires that intensity and phase of these multiple beams match, as described in detail in Reference [96].

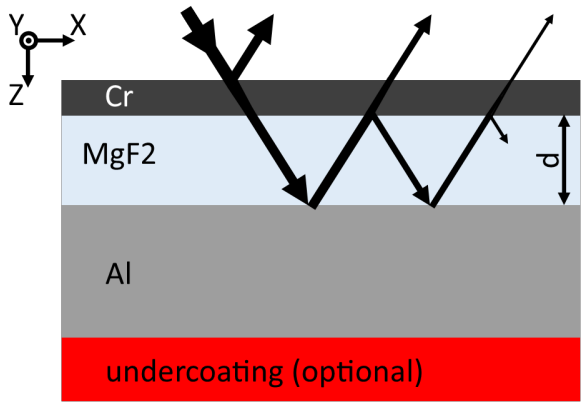

Figure 3-6. Schematical visualization of the fabricated MIM system.

Chromium is selected as partially transparent absorber layer in analogy to the work by Li et al. [45] as it tends to form closed and homogenous layers even at low thicknesses [127]. The relatively low absorption for a metal allows for a relatively large thickness in the range of 6-12 nm to achieve the optimum transmission of 40-70% for strong interference effects in this lossy Fabry-Perot stack, see Figure 3-7(a). The high transmission is a combination of two effects, thin films tend to form isolated islands with lower conductivity and chromium tends to oxidize. The latter effect is mainly prominent for laboratory samples with slow evaporation rates and long evaporation distances compared to roll-to-roll production, where the transmission of bulk chromium in Figure 3-7(b) is more appropriate. Thus, much thinner layers in the range of 3-6 nm are suitable for large scale fabrication. Note in both cases that too thin layers lead to lower reflections and thus weaker interference, while thicker layers prevent multi beam interference due to their low transmission. The reflectance spectra in the latter case are thus dominated by the reflectivity of the chromium layer only.

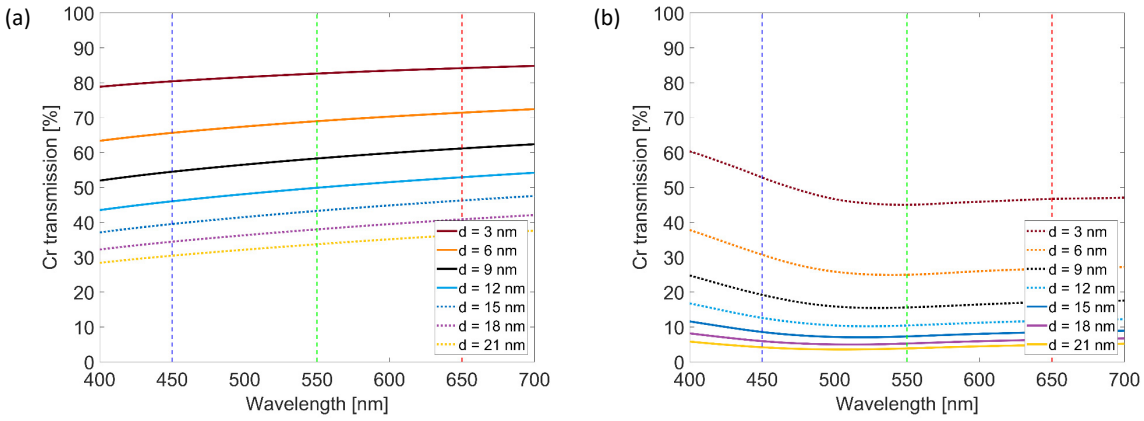

Figure 3-7. Simulated transmission of thin chromium films embedded in air. (a) Based on material data for thin films[127]. (b) Based on bulk material data[130].

Aluminum is chosen as opaque reflector as the mirror layer should be highly reflective and also be optically thick with a negligible transparency (below 1%) to assure that there is no influence of the substrate on the optical absorption of the system [131]. The high reflectance also allows for a high-quality mirror state as shown later. Besides fulfilling the technical criteria above, aluminum is also very economical, which makes the system compatible for mass production. Any

aluminum layer thickness above 30 nm assures the optically thick criterion and leads to identical optical absorption of the MIM system. However, the chosen thickness influences the process window as will be shown later for four different variations: 50, 100, 200, and 400 nm thick mirror layers.

The dielectric spacer layer can be any dielectric and MgF_2 was chosen here to benefit from a well-established thermal evaporation process in the laboratory; it could be replaced with any material of a similar refractive index, e.g. SiO_2. The spacer thickness *d* determines the conditions for constructive interference. These stacks produce a colorful effect for intermediate ranges of *d*, i.e. 300-500 nm, as only one or two wavelengths interfere constructively [28]. This effect is well known and has been applied for more than two decades on an industrial scale for the creation of color changing inks for banknotes and ID documents [132].

3.3.2 Optimization of the spacer layer thickness

The system here should however appear initially black and thus the MgF_2 thickness is varied in the much thinner range of 40-140 nm, while keeping constant the aluminum thickness of 50 nm and the chromium thickness of 9 nm. The reflection spectra is measured as outlined in Section 3.2.2 and the absorption spectra in Figure 3-8(a) are calculated from these values by applying Equation (3-1) as one can neglect here transmission thanks to thick enough aluminum layer.

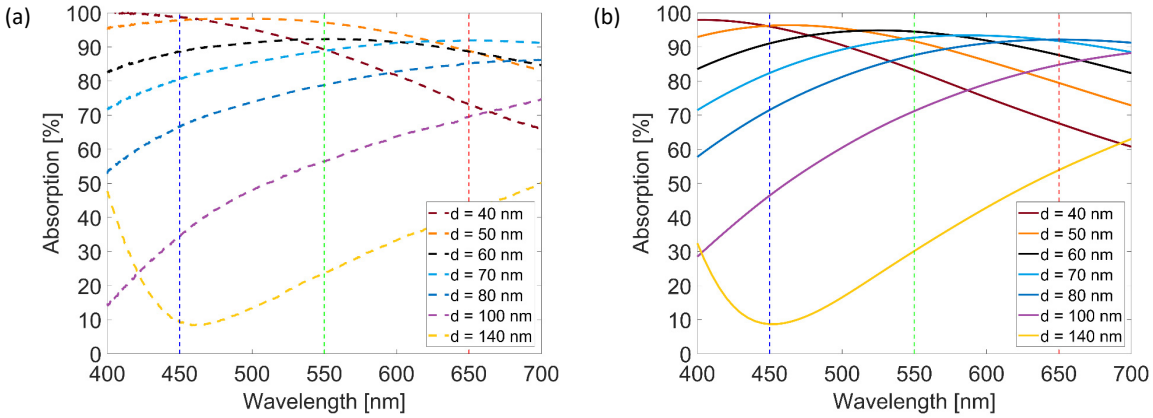

Figure 3-8. Absorption spectra of the MIM system for varying MgF_2 thickness.
(a) Experimentally measured spectra. (b) Simulated spectra.

The dashed measured spectra in Figure 3-8(a) agree extremely well with the solid simulated ones in Figure 3-8(b) using Lumerical FDTD [83] (an identical line color code is used for both panels). Both results reveal that exceptionally thin MgF_2 spacer layers in the range of 50-70 nm are best for maximizing absorption in the VIS. This good agreement is a consequence of the very smooth multi-layers system, as confirmed by AFM measurements ($S_q < 2$ nm) after evaporation of all three layers, see Figure 3-9. Consequently, the experimental data match the ideally flat system considered in the simulations.

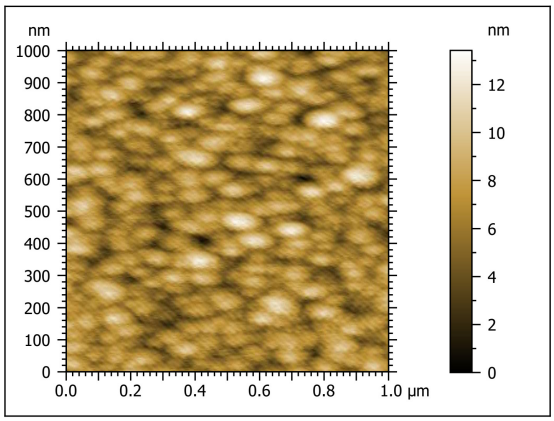

ISO 25178		
Height Parameters		
Sq	1.71	nm
Ssk	0.273	
Sku	3.20	
Sp	6.75	nm
Sv	6.67	nm
Sz	13.4	nm
Sa	1.35	nm

Figure 3-9. Atomic force microscope image that reveals the smoothness of the three-layer sample, where consecutively a 400 nm thick aluminum layer, a 60 nm thick MgF_2 layer, and a 9 nm thick chromium layer were evaporated.

This is also confirmed by the optical microscopy images of the fabricated samples with different MgF_2 spacer layers shown in Figure 3-10, where each image is framed with the color corresponding to the spectra in Figure 3-8. These images highlight the very different visual appearance of each sample as a function of the MgF_2 spacer thickness: the samples with the two thinnest MgF_2 spacer layers (40 nm and 50 nm) appear visually dark brown metallic; the optimal 60 nm thick sample appears nearly perfectly black; the 70 nm thick sample looks metallic dark grey and the 80 nm one grey; while the thickest samples (100 and 140 nm thick MgF_2 layers) appear metallic light blue. Thus, the optimal MgF_2 thickness of 60 nm is selected for all further experiments in this chapter as it exhibits the highest simulated absorption and has the darkest visual appearance of the three samples in the range 50-70 nm. Note that the experimental samples and the simulated system are embedded in air. Simply embedding the MIM system in e.g. a polymer would lead to lower absorption for this selected configuration with a 60 nm MgF_2 spacer layer, but it could also be optimized to reach a similar absorption performance by varying the spacer thickness to compensate for the different dielectric constant of a polymer compared to air.

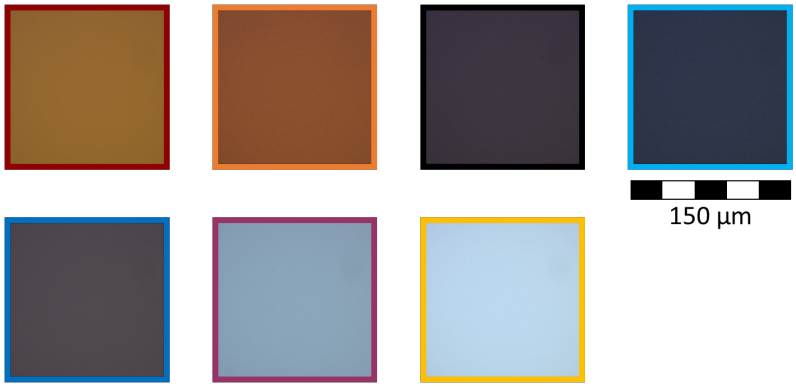

Figure 3-10. Microscopic images of the samples corresponding to the 7 absorption spectra in Figure 3-8, where the edge of each image is highlighted in the color of the corresponding spectra.

All the images in Figure 3-10 are taken with a 10 times magnifying objective (NA 0.3) and the observed microscopic colors agree very well with visual inspection as the color is relatively independent of viewing and illumination angle, owing to low thickness of the MgF_2 spacer layers. The modest dependency of the system on these observation parameters is shown by the direct reflection spectra in Figure 3-11 for observation angles up to 45°, which is sufficient for common low NA observation.

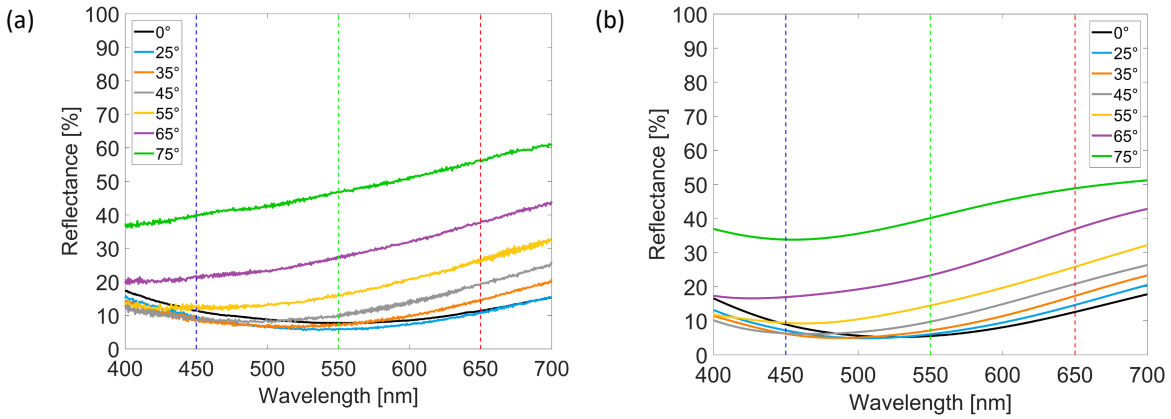

Figure 3-11. Reflection spectra of the system with a 9 nm thick chromium layer and a 60 nm thick MgF_2 spacer thickness for different illumination and viewing angles. (a) Photometrically measured and (b) simulated spectra for unpolarized illumination.

For applications where highest absorption and lowest dependency on the viewing angle are important, s-polarized light should be used for illumination as revealed by simulations for polarized light in Figure 3-12. For both polarizations, there is only a modest change in reflection up to incidence angle of 45° where the system is not polarization-sensitive, in agreement with the criteria for categorizing absorbing systems mentioned in Section 2.1.

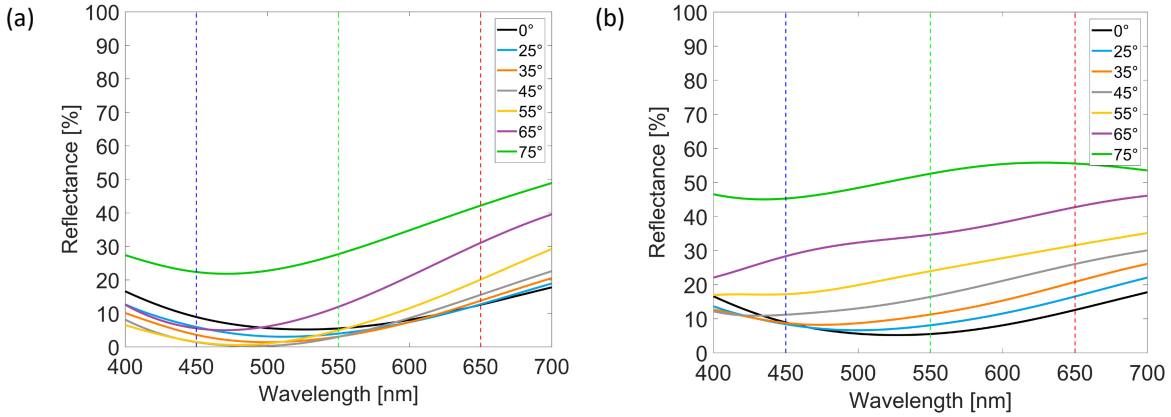

Figure 3-12. Simulated reflection spectra as in Figure 3-11(b), but illuminated with (a) s-polarized and (b) p-polarized light.

Indeed, the systems manufactured here fall into the second category of absorbing systems in Section 2.1, i.e. layered systems with homogenous top layers. It is a common property of these systems that they have negligible polarization and angular sensitivity, see Table 2-1. In comparison to the related systems in References [45,63–65], the investigated system here has slightly lower peak absorption and bandwidth of around 92.3% and 320 nm, respectively. The lower peak absorption is a consequence of the used aluminum mirror layer, instead of the lower reflecting materials such as chromium, gold, and tungsten used in those references. Both, peak wavelength and bandwidth, could nonetheless be further optimized, by varying for example the spacer or top layer material and thickness. As described in Section 2.4.6, general optimization for perfect absorption is possible using the admittance matching function and varying specific parameters [99,100]. However, the achieved average absorption of 91% in the VIS is sufficient for the demonstration of multi-state printing in this chapter.

3.4 Modifying the black state by pulsed laser processing

The previous section described how the optimal MIM configuration of a 9 nm thick chromium layer, a 60 nm thick MgF_2 spacer layer and a more than 50 nm thick aluminum layer was selected for maximizing absorption in the VIS. Let me now show that the initially black state can be switched locally to a reflective or transmissive state by focusing of a

nanosecond pulsed laser beam. Larger areas can be modified by scanning the focal spot across the sample as schematically shown in Figure 3-13, where the black state is modified locally at the focal spot by a single laser pulse. In between pulses, the focal spot moves to a new position, where the state can be altered with the same or another pulse energy. Repeating this procedure, one can raster scan the sample and modify its appearance locally within polygons, images, or line elements such as texts.

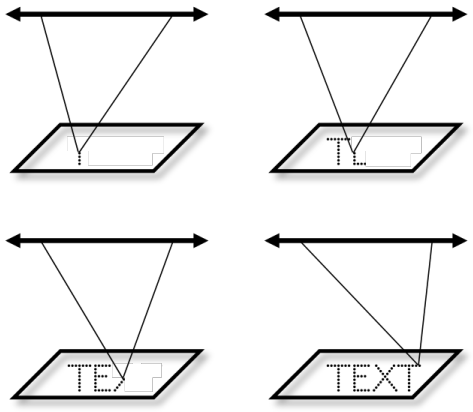

Figure 3-13. Schematical visualization of the point-wise raster-scanning of the laser focal spot to modify the samples state locally.

By varying the laser pulse energy one can either remove the chromium layer only or remove both the chromium and the aluminum bottom layer. Figure 3-14 shows the cross-section of the system (side and top views) for three different states (from left to right): the original state, the chromium layer removed and, finally, both metal layers removed. In direct reflection, these states correspond to a black, a mirror-like, and finally an almost completely transparent appearance, as depicted in the top view in Figure 3-14. Note that neither the metal layers nor the dielectric layers are substantially removed, the metallic layers are in fact melted and form nanoparticles with high transparency as will be shown in the following.

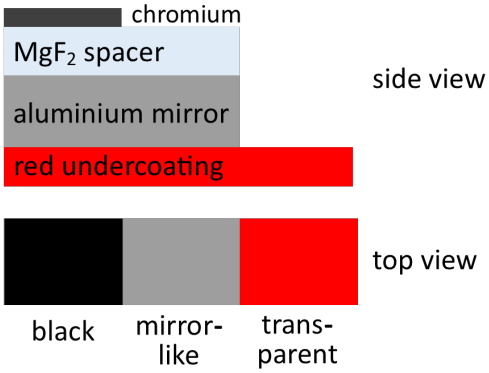

Figure 3-14. Visualization of the MIM system, where the top view shows the resulting state upon removing of the metallic layers.

By further modifying the density of the laser spots, one can realize semi-reflective states: a mixture of black and high reflectance; or semi-transparent states: a mixture of black and transparency. This rasterization produces areas of different transparencies, facilitating the realization of 3D impressions and half-tone images as shown in Section 3.5 [133]. However, the pure three states (black, mirror-like or transparent) are realized first, since this allows the determination of the process window and a more systematic description of the underlying physical mechanisms.

3.4.1 Absorption requirements for laser state switching

The commercial laser marking system Trumpf TruMark Station 5000, see Figure 3-15, operating at a wavelength of λ = 1064 nm with a typical pulse duration of 24 ns and an average optical power of 2.2 W at a repetition rate of 8 kHz is used for all experiments. Laser marking systems operating in the near-infrared at 1064 nm are readily available and are often used for the laser personalization processes of ID documents since the involved materials are transparent at this wavelength, or for other industrial applications [40].

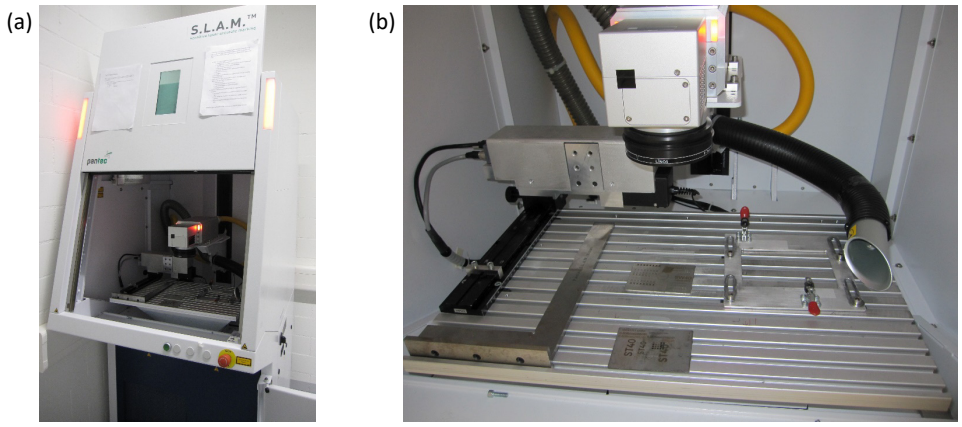

Figure 3-15. Photographs of the used laser marking system Trumpf TruMark Station 5000.
(a) System including protective door and (b) the laser marking area.

In order to modify, respectively melt any of the metallic layers one must assure that the MIM system absorbs at the lasing wavelength. Figure 3-16 extends the absorption spectra plot of Figure 3-8(b) to the near infrared NIR, where the laser operates. The optimized system with 60 nm MgF_2 thickness (black line) absorbs 42% of the incoming light power at 1064 nm according to simulations, while 58% is reflected and thus lost for the process. The laser wavelength of 1064 nm is visualized by a gray dashed line in Figure 3-16. A pulsed laser in the VIS could be more effective as around 91% of the incoming energy is absorbed on average in the VIS, but the laser power of the used marking system is more than sufficient to compensate the light loss in the NIR; actually, it even had to be attenuated for most experiments reported here.

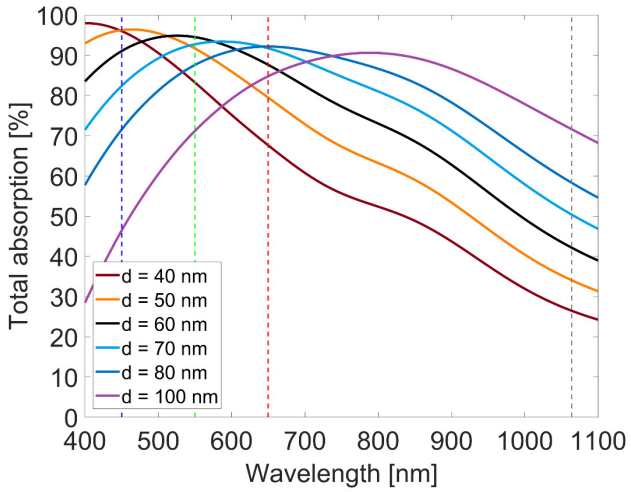

Figure 3-16. Simulated total absorption of the MIM system for varying MgF_2 layer thickness extended to the NIR.

Switching from the black state to the metallic or mirror-like state requires further that the light is absorbed substantially in the chromium layer to melt only this layer at intermediate laser pulse energy. Figure 3-17 confirms that this is indeed the case as about 88% of all absorbed light at 1064 nm is absorbed within the chromium layer (black line). The relative absorption is the ratio of the chromium layer absorption over the total absorption depicted in Figure 3-16. Thus, in total about 37% of the laser pulse energy is directly available for melting of the top chromium layer.

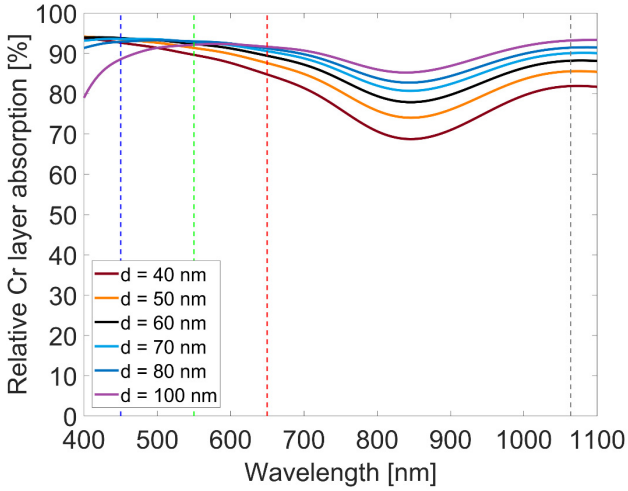

Figure 3-17. Simulated relative absorption within the 9 nm thick chromium layer for varying MgF_2 spacer thickness d.

3.4.2 Determining the process window of the laser state switching

The optical configuration of the used laser system Trumpf TruMark Station 5000 leads to a 40-50 µm laser spot size and for all the results in this section, the distance between consecutive laser spots is chosen to be 50 µm, such that individual laser spots do not overlap. The system is typically used for label engraving on bulk metal parts and its power had to be attenuated by 87.5% for all the results in this section, resulting in an optical power of 0.275 W and an energy per pulse of 34 µJ. These values correspond to 100% in the following analysis; they are sufficient to melt either only the chromium layer or both the chromium layer and a thin 50 nm bottom aluminum layer. A low power pulsed laser could also be utilized for this task, using a multi-pulse strategy to achieve similar results, as long as the repetition rate is high enough to prevent significant cooling between successive pulses [134,135]. This emphasizes that the results presented here can be realized with a variety of laser systems and all graphs use a relative scale to reflect this flexibility. Absolute values will depend on the laser system and the pulses overlap, but the curves and results presented here should be reproducible with many different laser systems.

Figure 3-18 shows this relative laser pulse energy versus average reflection in the VIS for varying thicknesses of the bottom aluminum layer on glass substrates. The relative laser pulse energy is about the same for switching from the initially black state with low average reflection (high absorption) in the VIS to the mirror state with high average reflection, by melting only the top chromium layer. This leads to a drastic increase of the chromium's transmission and happens between 20-30% relative laser pulse energy. On the other hand, switching from mirror-like to transparent state strongly depends on the aluminum bottom layer thickness: Thicker aluminum layers require a higher laser pulse energy and thus a wider range of laser pulse energies can be used to realize the mirror state. Consequently, the process window for three transparency state laser switching is larger for thicker aluminum bottom layers. Increasing the laser pulse energy further, the aluminum bottom layer as well as the top chromium layer are melted, thus transforming the initially black appearance into a mostly transparent one. Note that each of the test squares shown in Figure 3-18 has a side length of 3 mm and the spectral reflection is measured with a collimated light beam that has a diameter of about 2.5 mm. Each datapoint of the average reflection thus corresponds to the mean reflection from about 2000 laser processed spots since the raster cell area per spot is 2500 μm^2.

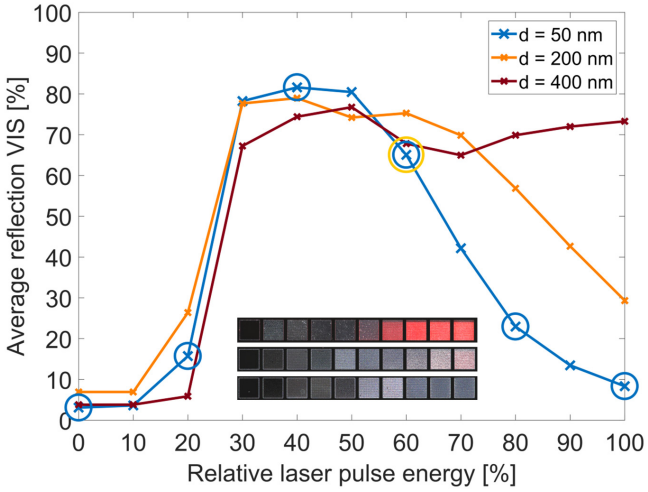

Figure 3-18. Process windows of the optimized system on 1 mm thick glass for varying aluminum mirror thicknesses.

The switching of optical states can also be observed in the inset of Figure 3-18, where the top row is a photograph of the sample with a 50 nm thick aluminum bottom layer, the central row with a 200 nm thick one and the bottom row with a 400 nm thick one. The laser power increases from left to right and the transparent state is revealed by placing red paper below the sample. This could also be realized with a thin red dye layer beneath the bottom aluminum layer, as shown in Figure 3-14. Note that even the thickest 400 nm aluminum layer can be made fully transparent using a higher laser power (approx. 150%) or applying several pulses at the same location as previously mentioned and utilized later.

Another parameter that significantly influences the size of the process window is the choice of the substrate material beneath the MIM system. The evaluated systems in Figure 3-18 are evaporated on 1 mm thick glass substrates, while those in Figure 3-19 are evaporated on 19 µm thin polyethylene terephthalate (PET) foils. This change of substrate material leads to a significant reduction of the process window. The switching from black to transparent state still happens for relative pulse energies around 20-30%, but the switching from mirror-like to transparent state happens now at a much lower power (compare for example the orange curves for d = 200 nm in Figure 3-18 and Figure 3-19). This can also be inferred from the insets in Figure 3-19 that show photographs of the test rows with increasing aluminum layer thicknesses from top to bottom and increasing laser power from left to right.

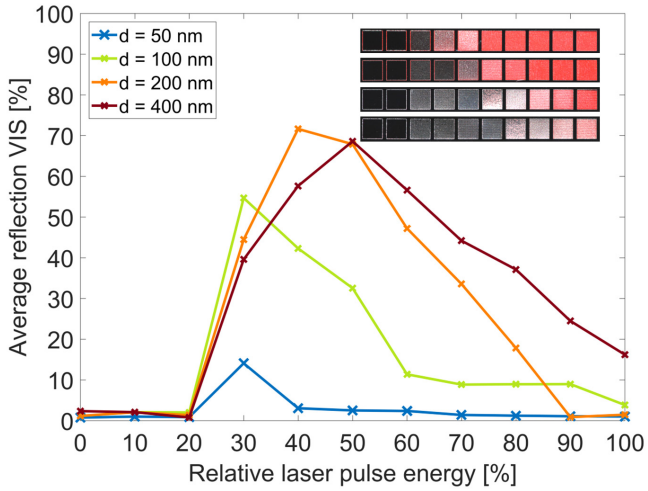

Figure 3-19. Process windows of the optimized system on 19 micron thick PET foil for varying aluminum mirror thicknesses.

Even for thick aluminum bottom layers, the laser pulse energy must be very precisely controlled to reproducibly switch between the three states; while for the 50 nm thick aluminum bottom layer, the mirror state cannot be reached at all. A likely reason for this behavior is that, since PET has a lower melting temperature, a larger fraction of the top PET

substrate surface melts compared to the glass one [136]. Heat is also likely more localized due to the lower heat conductivity of PET compared to glass [137] and further, the boiling temperature of PET is so low that fumes can crack the MIM system at intermediate laser pulse energies, which also increases transmission and consequently lowers reflection.

3.4.3 Microscopic effects associated with the laser power

The microscope reflection images in the top row of Figure 3-20 correspond to the blue encircled data points in Figure 3-18. They show how the initially black state (0% or no laser pulse applied) is partially switched to a mirror-like state at 20% relative laser pulse energy, second image from the left in the top row of Figure 3-20. It is known that the used laser system has a significant variation in laser pulse energy at low powers and thus the successive dots vary in shape and size. This MIM system can thus also be used to measure the reproducibility of laser pulses. At 40% relative laser pulse energy, the energy is sufficient to completely melt the top chromium layer. A fraction of the chromium layer is evaporated, but the larger fraction flows to the rim of the laser spot, mainly due to thermal gradients, where it solidifies and forms small chromium spheres (black dots in Figure 3-20) [138]. Increasing the relative laser pulse energy further from 60% to 80% and, finally 100%, results in partial and then full melting of the bottom aluminum layer. The liquefied metal is again redistributed to the rim of the individual laser spots as can be clearly seen in the rightmost picture, which corresponds to 100% relative laser pulse energy.

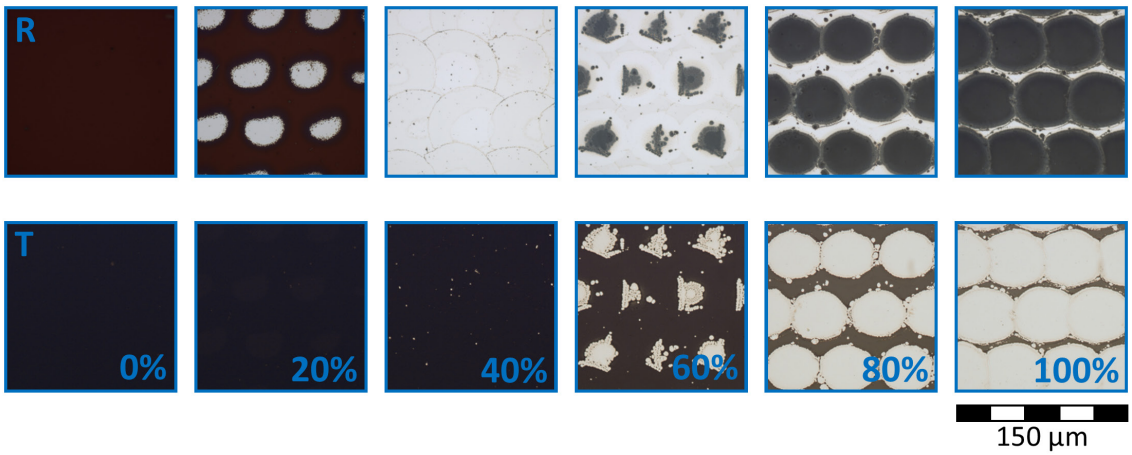

Figure 3-20. Optical microscopy reflection (top row) and transmission images (bottom row) for six different laser settings. (Data points highlighted by light blue circles in Figure 3-18.)

The dark areas in the microscopic images of the top row in Figure 3-20 for pulse energies between 60% and 100% are in fact transparent areas as revealed by the corresponding transmission microscope images in the bottom row. They are taken at identical positions by switching the microscope from reflection to transmission mode and show a contrast reversal between the reflection and transmission images. This confirms that the area modified by the laser pulse has effectively become transparent. Note that the remaining aluminum was partially melted close to the rims of the transparent areas and solidified again, forming typically spherical shapes as one might expect from the tendency of liquids to minimize free surface energy. The formation of a few micron sized spherical coagulations is only possible at the rim as the mobility is still high enough, while in the fully transparent areas particles in the submicron range are formed, which are essentially transparent besides negligible scattering and absorption caused by such small particles [1].

The insets in Figure 3-18 and Figure 3-19 are photographs of the samples placed on a red paper. Alternatively, one could place the samples on green, blue, or even white paper as shown in Figure 3-21. This illustrates how the transparent state can be used in combination with a suitable undercoating to realize multi-color states. Even a true-color image consisting of red, green, and blue printed pixels in combination with white and black metallic pixels is feasible by registered melting of the MIM system.

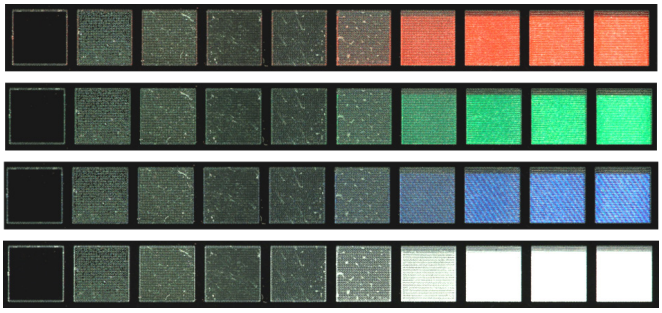

Figure 3-21. Photographs of the process window test pattern on plain paper as well as red, green, and blue papers.

3.5 Multi-state laser processing of MIM systems

The results in the previous section demonstrated that three different optical states can be realized by laser exposure: black, mirror-like, or transparent. These modifications occur at localized spots in the MIM system. In this section, this methodology is extended to create additional states by varying the rasterization strategy for the laser beam spots.

3.5.1 Multi-state artwork

Figure 3-22 shows a 3D art representation of the EPFL logo that requires six different states for its realization: black (initial, no switching), mirror-like, low-, medium- and full-transparency, as well as a matt state. The front faces of the logo are fully transparent, the top faces have a medium and the side faces a low transparency. The black lines between the red faces are not modified during laser processing and thus appear black as initially, while the background uses the mirror state. At the top left and bottom right, six white EPFL logos are placed that are created by a matt state, obtained by melting and reflowing of the top chromium layer as further explained in the next section. Beneath this artistic print, test squares of all five modified states used in the logo are placed and will be investigated in detail in Section 3.5.3. To utilize the largest process window, a glass substrate with an aluminum layer thickness of 400 nm in combination with a 9 nm thick chromium layer and a 60 nm thick MgF_2 layer is used for all remaining results in this section.

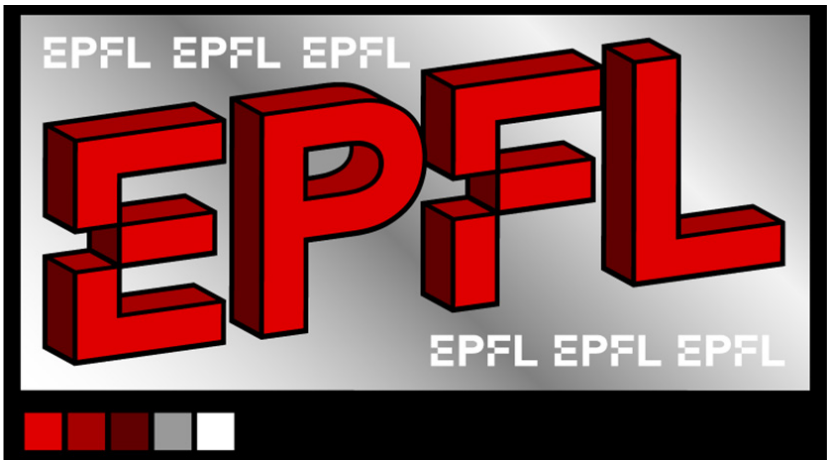

Figure 3-22. 3D artwork used for multi-state laser printing.

3.5.2 Multi-state realization using different rasterization strategies

The photograph in Figure 3-23 shows the laser modified sample placed on red paper. One clearly sees the scattering matt state for the three 2D EPFL logos at the top and bottom, as well as the differences in transparency for the 3D logo

faces, which agree well with the original 3D art design in Figure 3-22. On the bottom left of the picture one can identify quadratic test patterns for the five different optical states.

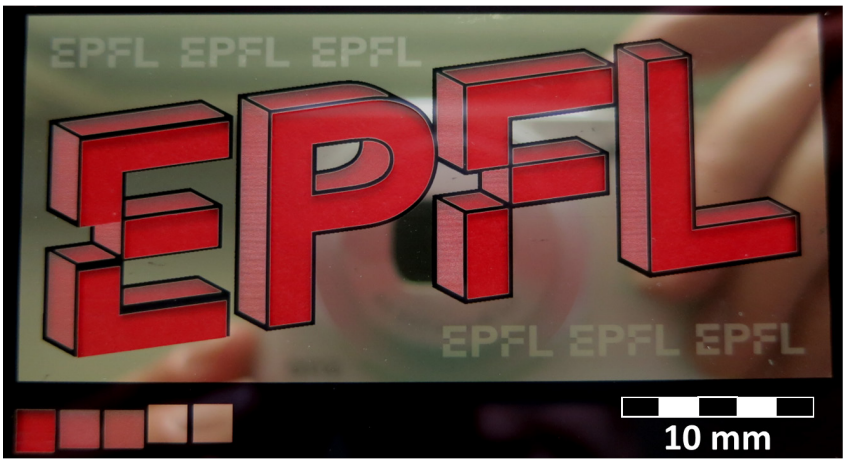

Figure 3-23. Photograph of the multi-state laser printed 3D artwork placed on top of red paper.

All these states are created by varying the laser rasterization strategy, while the black state needs no laser exposure at all as it corresponds to the original MIM system itself. The mirror-like state is realized as described in Section 3.4.2 by melting the top chromium layer with a single pulse strategy and 50 µm spacing between consecutive laser spots at intermediate power of 29% to reveal the aluminum mirror beneath. This state is also used as background for the 3D art, which is highly reflective as confirmed by the strong reflection of the camera. Both semi-transparent states are realized by adjusting the raster distance in one direction, as illustrated in Figure 3-24. Corresponding areas of the 3D art image are rasterized in a line-wise manner and a 25 µm distance between consecutive spots is used along this horizontal line by reducing the scanning speed to 50% of its original value of 400 mm/s and keeping the 8 kHz pulse frequency constant. The distance between successive raster lines in the vertical direction is changed to 60 µm, respectively 70 µm, for medium, respectively low transparency. This results ideally in 10 µm, respectively 20 µm wide black lines between the 50 µm wide transparent lines, producing a reduced transparency, viz. the non-processed and thus white areas between raster lines in Figure 3-24(b).

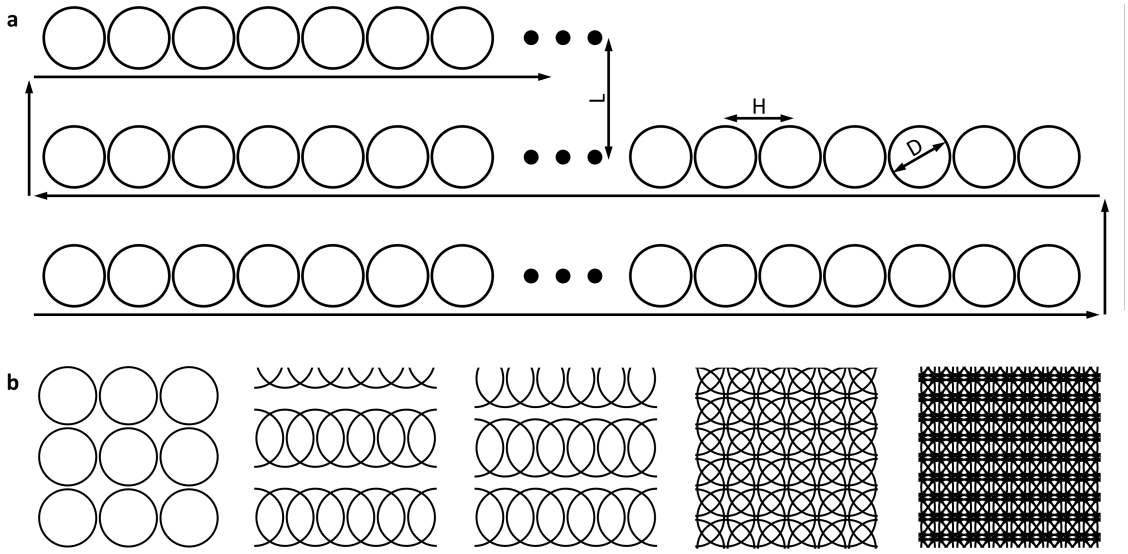

Figure 3-24. Schematic visualization of the used rasterization process. (a) The horizontal spacing *H* determines the overlap in primary scanning direction, while the line spacing *L* determines it in the secondary direction for the laser spots of diameter *D*. (b) Resulting raster patterns for the realized states: mirror, low to high transparency, and, finally, matt from left to right.

The fully transparent state is realized with a multi-pulse strategy by also decreasing the line spacing to 25 µm. This produces an overlap by about 50% for individual laser spots in both directions and ensures that the transparency is

maximized by fully melting also the 400 nm thick aluminum layer. The varying transmission grades for these three states can also be observed directly by inspecting the sample in transmission. Figure 3-25 shows a photograph of the sample when illuminated from the back. Note that the camera is still visible in reflection due to scattering of the transmitted light by the camera white front face.

Figure 3-25. Photograph of the multi-state laser printed 3D artwork illuminated from the back.

Finally, the sixth and last state realized here, is used for the series of white EPFL logos in the 3D artwork in Figure 3-23. It is a matt state, which corresponds to strong light scattering. This is realized with a slightly lower relative laser pulse energy (27%) than that used for the mirror-like state (29%), but with a large spatial overlap of the individual laser spots, i.e. 75% overlap and thus a multi-pulse strategy. This leads to multiple reflow and solidification of the chromium top layer. The liquefied chromium flows towards the rim of each laser spot due to a thermal gradient, resulting in a pseudo-periodic pattern with a mean period length of 12.5 µm as shown in Figure 3-26 top right. The reflow produces a topography, which in turn alters the phase of the incoming light and ultimately leads to scattering. The periodicity of this pattern is however broken, mostly due to the limited precision of the laser scanning system. All modified laser power and raster parameters for these states are summarized in Table 3-2 below, while the laser pulse frequency of 8 kHz was kept constant for all state realizations. The raster parameter summarized in Table 3-2 are also illustrated in Figure 3-24.

State	Laser power [%]	Speed [mm/s]	Overlap [%]	Raster line spacing [µm]
Mirror	29	400	none	50
High transparency	70	200	50	25
Medium transparency	50	200	50	60
Low transparency	50	200	50	70
Matt	27	100	75	15

Table 3-2. Laser and raster parameters of the five states that were used for the 3D print realization in Figure 3-23.

3.5.3 Microscopic inspection of the different states

The optical microscope images shown in Figure 3-26 assists the investigation of the effects on the MIM system by laser processing. The top row corresponds to reflection images and the bottom row to transmission images; each column corresponds to one of the test patterns on the bottom left in Figure 3-23. The three left image columns reveal that these test patterns are indeed mostly transparent and have weak blocking lines in case of the medium and low transparency state. The fourth column from the left in Figure 3-26 shows the mirror-like state, where the chromium flew to the rims of the individual laser spots. This state is also used as background for the 3D art, which appears greyish in the photograph due to the chosen exposure angle to avoid saturation effects from direct light reflection. Finally, the right most column in Figure 3-26 shows microscope images of the matt state and reveals the pseudo-periodic reflow of the aluminum bottom layer as previously mentioned. These last two states (mirror-like and matt) have no transmission as is evidenced

by the corresponding optical microscope transmission images (Figure 3-26, bottom row), since the bottom mirror layer remains intact.

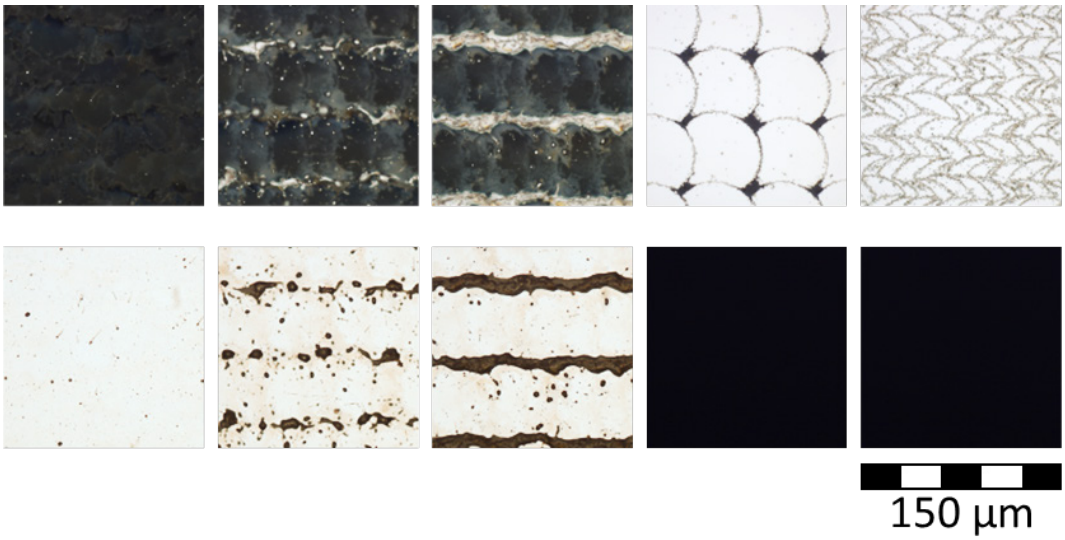

Figure 3-26. Optical microscopy reflection (top row) and transmission images (bottom row) of the five test pattern squares.

3.6 Conclusion

In summary, MIM systems that absorb more than 90% of the incident light in the VIS and thus have an initially black appearance were evaporated on either glass or PET foil. This high absorbance of the initially black state was made possible by optimizing the top and spacer layers thicknesses. The measured absorption spectra for various spacer thicknesses agreed excellently with simulation data. The black appearance of the optimum system was locally modified by laser focusing a λ = 1064 nm nanosecond pulsed laser to 50-micron sized spots and varying the pulse energy. This allowed the realization of a six-state 3D artwork print with defined areas containing either a black, mirror-like, matt-like or one of three transparent states.

The transparency was selectively tuned in three different grades by altering the raster strategy of the printing process. Realizing additional transparent states would be straightforward by further altering the rasterization. The influence of substrate material and metallic bottom layer thickness on the process window of this novel multi-state process was determined and discussed in detail. The mechanisms of the different states were investigated thoroughly and verified by microscopic inspections of the formed micropatterns.

3.6.1 Comments on industrial scalability

The whole system could be manufactured on foil with three successive evaporation steps on a roll-to-roll basis. All mentioned evaporation materials are commonly used in industry, they are even used for mass production of colorful ink pigments [132]. The only difference to this established mass production product is the thinner spacer layer thickness. This is actually an advantage as it saves material costs and possibly manufacturing time since one can increase speed to evaporate thin layers compared to the state-of-the-art ones. Thus, industrialization of the system seems to be very feasible, and one might apply this methodology also to alter the impression of these colorful ink pigments, turning them either mirror-like or transparent. Note that initial trials showed that the MIM system can also be applied on diffractive structures such as gratings, rendering devices based on these structures a black appearance.

However, evaporating the MIM system on top of any surface, be it a simple plane surface as shown here or a surface containing a plurality of nano- and microstructures comes at the cost of a main challenge. This challenge is the adhesion to the surface on which the layers are applied and the one between the different layers. The former could be solved by applying a nanometer or even sub-nanometer thick adhesion layer, although it nonetheless represents a challenge. The latter could be addressed by plasma treatment prior to each evaporation step. Independent of the solution chosen, it must fulfill the applications specifications.

For example, integrating such a three-layer system in an optically variable device (OVD) for the protection of document authenticity demands that the OVD satisfies certain standards. Applying it in an OVD that is applied on top of a data page, e.g on an identity card or the first page of a passport, it must pass the adhesion tape test [139]. In case it is part of an embedded solution, it must withstand the lamination process and pass the peel test [140] with minimum values specified in [141]. Both tests are relative measure on how well the OVD adheres to the applied surface or within the laminate stack; other applications might be even more demanding. Note that besides the optimization for peel of this embedded OVD solution, one must also optimize the spacer layer thickness as the refractive index of the embedding polymer is different from air. This step can be easily carried out with simulation methodology developed in this chapter. Thus, the MIM structure presented in this chapter might be detrimental for the chosen application without proper optimization of evaporation conditions, treatment and materials used.

3.6.2 Possible industrial applications

The application of the system on OVDs is driven by my personal expertise in this field of more than ten years. The application there makes perfects sense to me as it provides a mean for personalization of any OVD element, while initial tests indicate full compatibility with typical elements of OVDs such as gratings. It is certainly not limited to this very specialized field and can also find applications in any of the fields mentioned in Section 2.5.2 that demand a static black appearance and benefit from long-term and UV stability of the selected materials. However, the fact that the system allows for the modification of its initially black appearance to either highly reflective or transmissive one also enables its application to the following fields:

- Replacement of laser engravable plastics, e.g. for text and image areas in authentication documents
- Laser-personalized car plates, e.g. microtext within the black letters as forensic feature to proof authenticity
- QR codes due to high contrast, e.g. high specular reflection of mirror state vs. initial black
- Optical isolators for camera sensors, creation of very thin black lines between pixels
- Labels for track and trace applications
- Personalized product labels, e.g. on Coca-Cola bottles
- Backlighted advertisements that combine light-emitting (transparent) areas with reflecting or black ones
- Personalized clothes and fashion in general
- Diffractive optical devices as one can easily switch between high absorption, reflection, and transmission
- Binary recording material for pulsed laser holography
- Thermal printing by inclusion of low melting metals in the MIM system
- Validating element on multiple-journey tickets

This list is certainly not comprehensive, but highlights that many applications with a requirement on local modification of their optical appearance could benefit from the technology developed in this chapter.

Chapter 4 Color gamut enhancement of dye lacquers using corrugated surfaces

Both systems in the previous chapters are optimized for broadband and near perfect absorption across the entire VIS, resulting in a black appearance. Contrary to these systems, only a fraction of the VIS is absorbed by the system in this chapter to realize a colorful and vivid appearance. This is achieved by combining the structural color of crossed gratings with the color of dye lacquers. The presented results in this chapter are also an extended version of a publication [142], with additional content on the used methodology, industrial realizability and possible applications.

The objective of this chapter is to show how the (chemical) absorption of a dye can be strongly enhanced by interaction with a (physical) corrugated surface to create colorful and vivid appearance. For this purpose, I explore a fully original approach by combining physical/structural with chemical colorization means. The results are inspired by a baffling experiment made in the laboratory: By coating an almost colorless micron-thick yellow dye lacquer conformally onto a corrugated metal surface, suddenly extremely vivid saturated colors were observed, clearly differing form the expected yellow color. This totally unexpected effect is the signature of the strong interaction between the physical structure and the chemical dye, leading to significantly higher absorption of the system compared to what would be expected from the simple combination of the individual absorptions.

The origin of the significant color enhancement is attributed to the interaction between the dye lacquer and the strong near-field created by the corrugated metal surface in the form of a sub-wavelength crossed grating. The local field enhancement of more than a factor of 20 within the dye lacquer boosts its absorption. The gratings self-color is largely determined by the excitation of surface modes, which manifest as Rayleigh and Wood's anomalies. Detailed guidelines on how to engineer the corrugation self-color and widen the color gamut of the combined system are provided by showing the effects of varying the corrugation period and dye lacquer absorption. These findings can be used to realize any color at will with this combined system.

A brief overview for recent trends in color generation is given in Section 4.1, before details of the used methods are provided in Section 4.2. The latter section includes a thorough description of all experimental and numerical methods used to manufacture, measure, and simulate the combined system. The optical reflection spectra and resulting self-colors of the corrugation in the form of a crossed grating are reported in Section 4.3, while Section 4.4 introduces the excitation criteria and the nomenclature for different surface modes on linear gratings that can significantly modify the gratings reflection and absorption. In Section 4.5 it is demonstrated that absorption of dye lacquer can be significantly enhanced by applying it conformally on a crossed grating. This section also contains a detailed description on how the refractive index of the investigated dye lacquers is retrieved for accurate numerical modelling. Section 4.6 reveals the main mechanisms leading to this extraordinary absorption enhancement within the dye lacquer. The findings are applied in Section 4.7 to increase the color gamut of corrugations combined with artificial dye lacquers. This Chapter concludes with Section 4.8, where the possibility to manufacture the system on an industrial scale and further applications are discussed.

4.1 State-of-the-art in color generation

Pigment-based coloration is used for almost any type of plastic-based consumer good today, but colors could also be generated with structural colors [23,143]. Classical mechanisms for structural color generation are interference, diffraction gratings, and photonic crystals [143]. In the last decade, research also focused on color generation with plasmonic

systems. These systems allow for producing colors with colorless metals such as silver or aluminum [19,23,35,36,123,124,144]. Such systems can be as simple as a single metal particle, where material, size, shape and refractive index of the surrounding medium determine the color impression of the particle [5,14,16,145,146]. Indeed, all these parameters influence the absorption amplitude and the wavelength of the localized plasmon resonance within the particle [3,11]. On the other hand, one can also use a system supporting propagating surface plasmon-polaritons or in short surface plasmons [6,147,148]. These systems are often periodic at a length scale below the wavelength of visible light and have been optimized for color generation in reflection [23,43] as well as transmission [42,149,150]. In the case of periodic systems, the color is mainly determined by the material, periodicity, shape, and the refractive index of the surrounding medium [66]. The color generation of plasmonic systems is based on absorption due to the excitation of surface plasmons and not on an interference-based effect; the periodicity as well as material choice determine the wavelengths which can excite surface plasmons [6].

In this chapter, vivid colors are generated by strongly enhanced absorption within dye lacquers applied conformally on crossed metallic gratings with identical periodicity in both dimensions. Unlike previously published works, this chapter focus not only on the generation of color by the grating itself [23,43,143], but explores its possible interactions with a dye lacquer to strongly enhance the dye absorption. Instead of the conventional approach that consists in embedding a color generating system in a non-absorbing dielectric medium [23,35], a partially absorbing dye lacquer is applied conformally and in direct contact to the grating surface.

This idea is inspired by works of others, who measured a significant fluorescence emission enhancement for molecules placed at well-defined distances atop a metallic grating [151,152]. This concept was also used for light extraction to improve the efficiency of a light emitting diode [153]. Instead of enhancing fluorescence emission, the focus in this chapter lies on the enhanced absorption of sub-micron thick (semi-)transparent dye lacquers applied conformally to metallic crossed gratings. Rather than varying the distance of the absorbing material to the metal surface, the thickness and extinction coefficient κ of these lacquers is varied. This detailed study reveals the mechanisms for enhancing absorption within the dye lacquer. The findings are not limited to color generation and may find applications in other fields, such as solar cell absorption improvement [154], Raman spectroscopy [155], or highly sensitive sensing applications [156].

4.2 Methodology

4.2.1 Grating fabrication

The crossed grating is manufactured in photoresist by conventional two-beam laser interference [157,158]. The photoresist plate is exposed twice with a standing wave pattern in the form of a linear sinusoidal grating. Rotating the plate by 90° between the two consecutive exposure steps with identical doses, a square crossed grating with a period of 300 nm in both directions is exposed in the photoresist [159]. Developing the plate transforms the exposed image in a surface relief grating, which is then copied by electroforming in nickel [160]. The gratings shape and height depend mainly on the chosen exposure dose, development time and developer type, as reported elsewhere [160,161]. The chosen development conditions lead to a slightly non-linear grating profile and thus it cannot be described by a pure sine or cosine function as will be reported in Section 4.3.

4.2.2 Aluminum evaporation

The aluminum layer was evaporated with a Leybold Heraeus L560 by electron-beam evaporation, see Figure 3-2(a). For the deposition, the chamber was evacuated to a pressure of 4.6×10^{-5} mbar and the deposition rate was adjusted to 0.4-0.6 nm/s.

4.2.3 Simulation setup

All simulations were performed with Lumerical FDTD [83], where a linearly polarized broadband source from λ = 300 nm to 800 nm was used to illuminate the crossed grating. The simulation region was set to 300 nm × 300 nm × 2100 nm with a conformal meshing of variant 1 with an accuracy of 7. The mesh size was overwritten in the region, where the grating and dye are located to a maximum size of 3 nm × 3 nm × 1.5 nm to avoid significant staircasing effects of the gratings profile. Bloch-type periodic boundary conditions were selected laterally and perfect matching layers with 32 layers in *z*-direction. Power and grating order detectors were placed at appropriate positions in accordance with the recommendations by Lumerical to achieve the highest possible accuracy in reflection and grating order power detection. The material data of nickel and aluminum are based on literature values by Palik [130]. The most important simulation parameters are summarized in Table 4-1.

Parameter	
FDTD-simulation region	300 nm × 300 nm × 2100 nm
Boundary conditions	Bloch in X- and Y-direction. Perfect matching layer PML with 32 layers in z-direction
Mesh type, refinement, and accuracy	Auto non-uniform, conformal variant 1 and level 7
Time step and minimum mesh size	dt stability factor 0.99 and 0.3 nm
Source	Linear polarized light incident parallel to z-axis and 45° with respect to X-Y-axis with bandwidth 300-800 nm. Injected at z = -800 nm with unit amplitude
Frequency domain power monitors	Transmission is recorded at z = -1000 nm Reflection is recorded at z = 900 nm by a grating detector
Material parameters	Al (Aluminum) Palik with 6 coefficients Ni (Nickel) Palik with 6 coefficients Dye lacquers (custom fit) with 8 coefficients
Dielectric background/embedding	Constant values of 1.0 and 1.5, respectively
Early Shutoff	1E-5

Table 4-1. Summary of relevant simulation parameters.

4.2.4 Dye lacquer formulation and coating

The dye lacquers consist of four commercially available components, mainly two solvents as the solid content of each lacquer is less or equal to 1%. The lacquers are created by adding 1-methoxy-2-propanol to toluene, stirring and heating the mixture to 60°C. It is then combined with the binder Dow Paraloid A11 while stirring and stirred for 30 minutes before cooling to room temperature, when the dye BASF Orasol Red 365 was amended and stirred for another 5 min to create a homogenous and fully mixed solution. The solutions are applied on the gratings by spincoating at 3000 rpm for 30 s, after which they are dried for 15 min in a convection oven at 75°C to form the solid lacquer. This results in three different dye lacquer thicknesses, 13 nm (thin), 35 nm (medium) and 50 nm (thick), respectively. The recipes for 75 g of each lacquer are summarized in Table 4-2. Note that the ratio of dye and binder of the medium concentrated dye lacquers is constant.

Lacquer	Dye content (solid lacquer)	Solid content (solution)	BASF Orasol Red 365	Dow Paraloid A11	1-methoxy-2-propanol	Toluene
HC-Thin (13 nm)	80.0 wt%	0.25 wt%	0.20 wt% (0.150 g)	0.05 wt% (0.038 g)	49.87 wt% (37.406 g)	49.87 wt% (37.406 g)
MC-Medium (35 nm)	33.3 wt%	0.50 wt%	0.17 wt% (0.125 g)	0.33 wt% (0.250 g)	49.75 wt% (37.313 g)	49.75 wt% (37.313 g)
MC-Thick (50 nm)	33.3 wt%	1.00 wt%	0.33 wt% (0.250 g)	0.67 wt% (0.500 g)	49.50 wt% (37.125 g)	49.50 wt% (37.125 g)

Table 4-2. Formulations of three experimentally investigated dye lacquers.

4.2.5 Spectral measurements

All direct reflection measurements are carried out with a self-built spectroscopic setup, see Figure 3-3. The light of a broadband light source Thorlabs SLS201/M is guided and collimated with the bifurcated reflection probe Avantes FCR-7UVIR200-2-ME. The collimated light beam hits the sample, and the reflected part is guided again by the bifurcated reflection probe to the Avantes Avatec ULS3648-USB2 spectrometer. A broadband dielectric mirror Thorlabs BB1-E02 is used as a reference for all measurements.

4.3 Measurement and simulation of gratings self-color

Visual inspection of nickel crossed gratings that were fabricated as outlined in Section 4.2.1 exhibited a drastic color change in direct reflection upon embedding in a dielectric medium. The insets in Figure 4-1(a) show that the negative profile grating changes its color from light brown to violet (bottom row images with purple boarder), while the positive one changes to dark brown upon embedding (top row images with orange boarder). The negative profile is a galvanic copy of the gratings initial positive profile in photoresist and the positive profile is realized in nickel by copying galvanically the original photoresist profile twice.

The visually observed color difference of both profiles upon embedding can also be depicted from the measured spectra in Figure 4-1(a), where the chosen line colors coarsely resemble the observed one. The orange and upwards pointing triangles indicate the positive orientation, while the negative orientation is marked by downwards pointing ones in purple. The structure depth is identical for both grating profiles due to the galvanic copying, but the spectra are not, already indicating the crucial role of the profile shape. The observed spectral differences are an indication of an asymmetric shape, which is confirmed by scanning electron microscope (SEM) images of both orientations in Figure 4-1(b,c). The overlaid insets emphasize that both profiles are simple galvanically mirrored copies of each other with identical profile height, but mirrored shape. The SEM images are also framed with orange lines for the positive and violet ones for the negative profile matching the corresponding frame color of the insets in Figure 4-1(a).

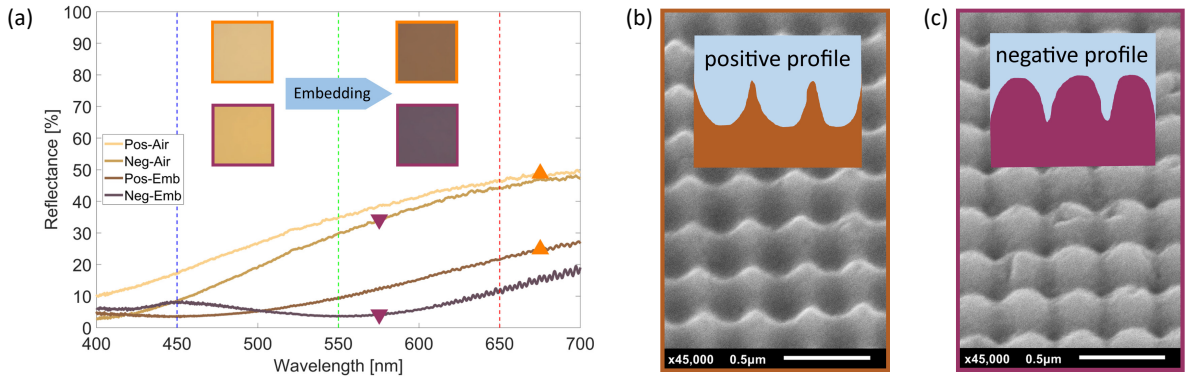

Figure 4-1. Measurements of nickel crossed gratings. (a) Measured reflection spectra for sinusoidal crossed gratings in nickel surrounded by air and embedded in a dielectric with refractive index n ≈ 1.5. The insets show optical microscope images of the color before and after embedding. (b) SEM images of a crossed grating with positive profile and (c) negative profile. The insets emphasize the asymmetry between the positive and negative grating profiles.

In order to analyze the origin of the observed color change upon embedding, the system is modeled in Lumerical FDTD [83]. The crossed grating is described in the simulation by a surface structure object and the shape of this object is defined by a third order cosine fit to enforce symmetry with respect to the center of a single grating period,

$$z(x) = 0.0045\cos^3(2\pi x\ /\ 0.3\ \mu m) + 0.0068\cos^2(2\pi x\ /\ 0.3\ \mu m) + 0.0520\cos(2\pi x\ /\ 0.3\ \mu m) + 0.0407. \quad (4\text{-}1)$$

Equation (4-1) is the result of a least square fit to graphically extracted data points following the central hill of the positive profile cross section shown in Figure 4-2(a). The fitted grating profile is overlaid as a dotted pink line on the cross section to demonstrate the excellent agreement between fit and cross section. The fit looks at first glance like a

pure cosine, but minorly differs from a cosine as one can observe quantitatively from Equation (4-1) and graphically from Figure 4-2(b). Nonetheless, this minor deviation from a pure cosine renders both profiles (positive and negative) non-symmetric, which leads to this well-visible color difference upon embedding in Figure 4-1(a). Note that for all results in this chapter, identical profiles are used in both directions of the crossed grating.

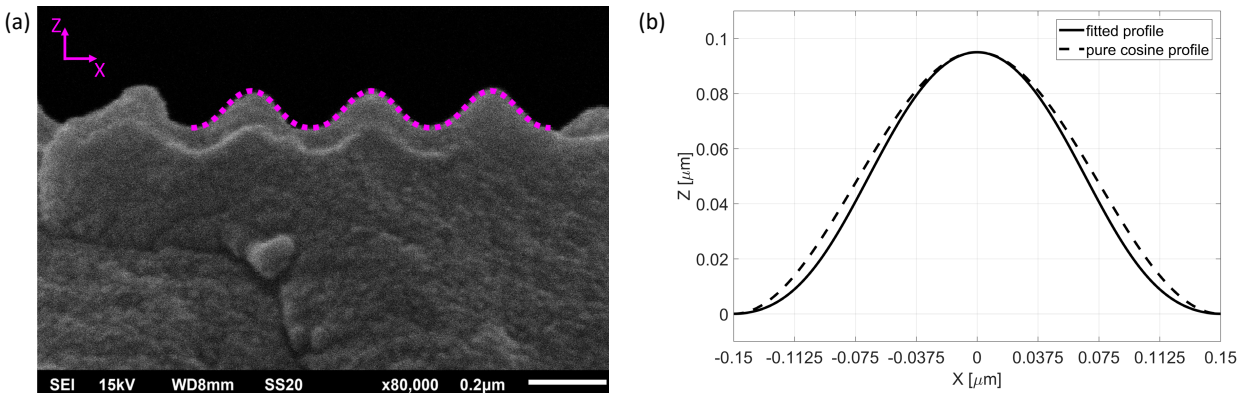

Figure 4-2. Visualizations of the positive profiles third order cosine fit. (a) SEM image of the gratings positive profile cross section overlaid with a third order cosine fit. (b) Fitted profile overlaid with a pure cosine grating of identical 95 nm maximum depth.

Larger deviations would lead to even stronger differences and gratings with identical height, but mirrored shape can even lead to complementary spectra, see Figure 4-3.

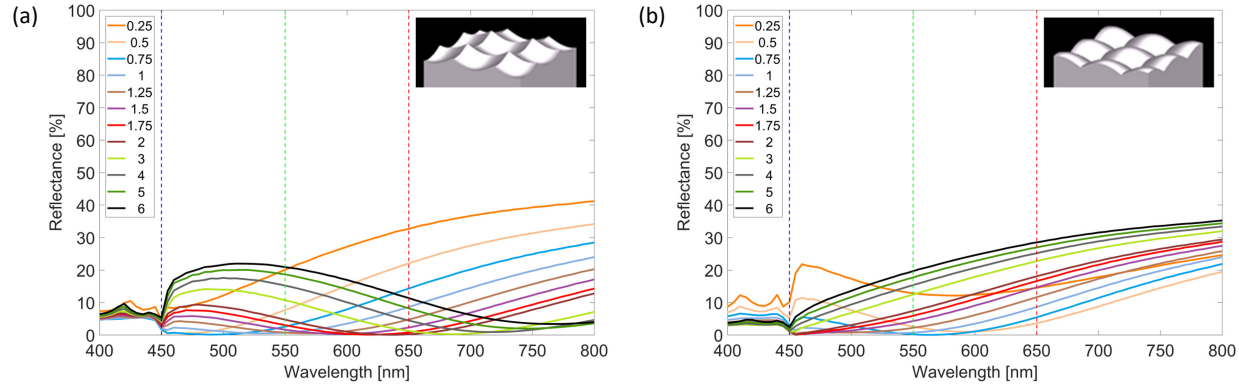

Figure 4-3. Simulated spectra for crossed cosine gratings for various cosine powers and a total depth of 175 nm with (a) positive profile and (b) negative profile of the grating. The insets illustrate the corresponding simulation geometries corresponding to 0.5th power gratings.

For the results in Figure 4-3, a linearly polarized plane wave source impinges on the corrugated surface with a polarization angle of 45° with respect to the gratings main axes and more simulation details are provided in Section 4.2.3. Based on the fit defined by Equation (4-1), the direct reflection of nickel grating is calculated with otherwise identical simulation parameters. The simulated spectra in Figure 4-4 agree extremely well with the experimental ones reported in Figure 4-1(a) for the different studied profile orientations, both in air and embedded in a dielectric with a refractive index *n* of 1.5.

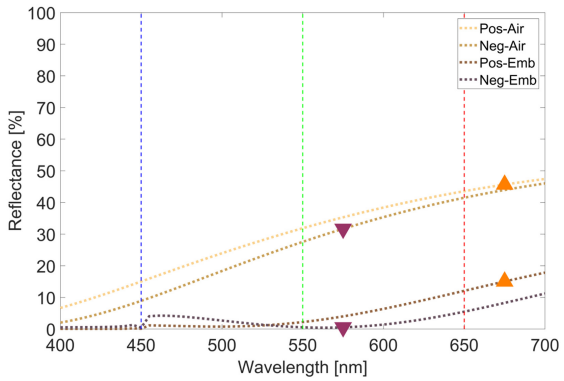

Figure 4-4. Simulated spectra of nickel gratings corresponding to measured spectra in Figure 4-1(a).

To reach this excellent agreement, a 10% reduced grating depth was used. The SEM fit estimates a total depth of 190 nm (2x 95 nm), but a variation of the depth showed best agreement for a total depth of 172 nm. This value also agrees exactly with the mean depth determined by atomic force microscopy (AFM), see Figure 4-5.

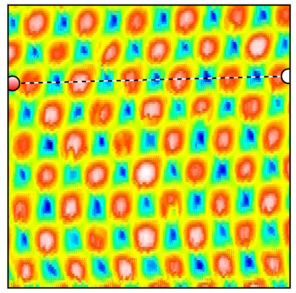

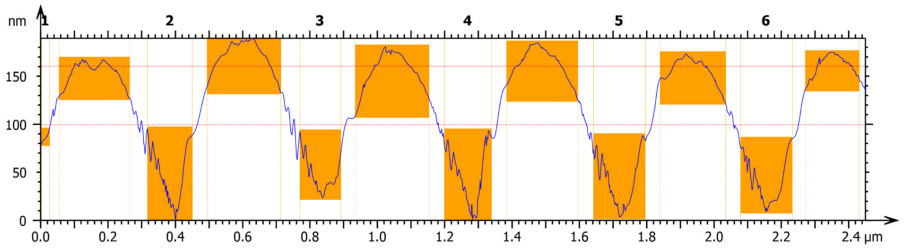

Parameters	Unit	Step 1	Step 2	Step 3	Step 4	Step 5	Step 6
Width	µm	0.0244	0.133	0.122	0.140	0.154	0.154
Total depth p-v	nm	*****	168	166	180	181	164

Figure 4-5. Exemplary AFM measurement of the positive profile crossed grating, the average depth is 172nm.

This slightly reduced depth also gives the best agreement, when the grating material is changed from nickel to aluminum as indicated by Figure 4-6. In the simulation, the semi-infinite grating material is simply changed from nickel to aluminum, while for the experimental realization, the nickel grating is overcoated with a 50 nm thick aluminum layer. On one hand, the chosen thickness ensures that negligible light is transmitted through the aluminum layer and the nickel base grating can be excluded in simulations. On the other hand, the layer is still so thin that the profile is not significantly altered as confirmed by the good agreement in Figure 4-6 of the measured aluminum grating spectra (solid lines) with the simulated ones (dotted lines).

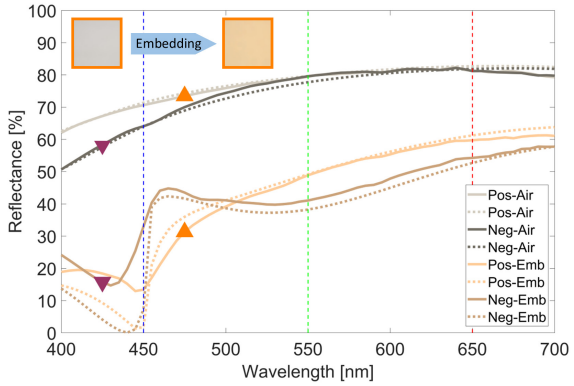

Figure 4-6. Measured (solid lines) and simulated (dotted lines) reflection spectra of the crossed gratings with aluminum surfaces. The insets show optical microscope images of the samples.

For the aluminum system, all observed colors are generally brighter due to the materials higher reflection compared to nickel. The colors are also clearly different from the nickel case and so is their alteration upon embedding in a lossless

dielectric: the color changes from metallic grey to a light orange for the positive profile as shown in the insets of Figure 4-6. Note that the measured spectra in Figure 4-1 and Figure 4-6 clearly indicate that the color is not based on interference effects because the characteristic regular interference minima and maxima are not present [28]. This is also confirmed by Figure 4-7, where the fitted positive profile according to Equation (4-1) is scaled to six different depths, showing that the locations of spectral peaks and valleys are nearly constant. This is contrary to the strong dependence on shape shown in Figure 4-3 as the dependence on depth is only modest as Figure 4-7 reveals. Strong material dependence and weak depth dependence indicate a different, possibly plasmonic-related color generation mechanism that will be introduced and studied next for linear gratings.

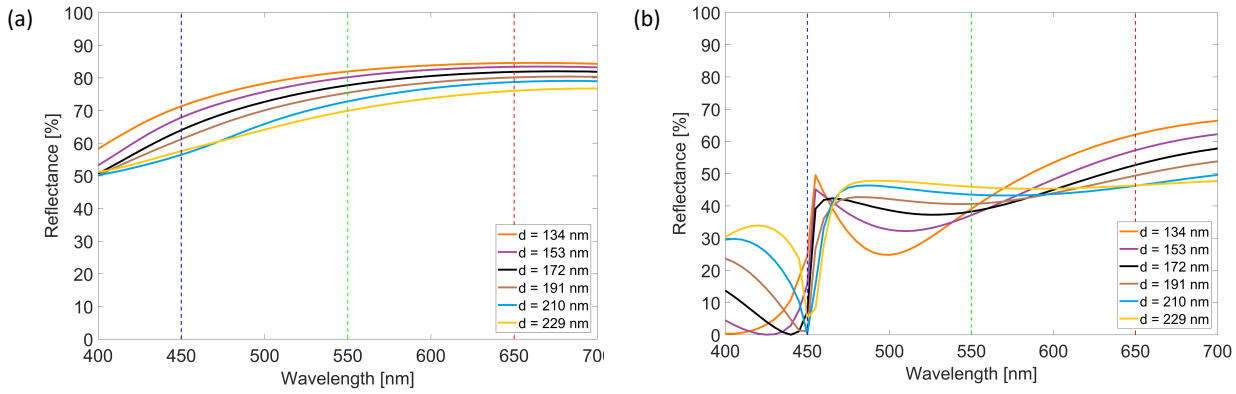

Figure 4-7. Simulated spectra for crossed gratings with a positive profile scaled to six different depths *d* (a) in air and b) embedded in a dielectric medium with refractive index of 1.5.

4.4 Surface modes excitation by gratings

The fabricated crossed gratings outlined in the previous section exhibit a distinct self-color in direct reflection that strongly depends on the surrounding dielectric medium. The corresponding spectrum for this self-color is greatly determined by the excitation of a Rayleigh anomaly as will be shown in Section 4.6 [162]. Rayleigh anomalies are the manifestation of one type of surface waves that can be excited on periodically corrugated surfaces, such as the grating considered here; the other type of surface wave leads to Woods anomalies [163–165]. Generally, light with a vacuum wavelength λ_0 is diffracted by a linear grating to several diffraction orders m, which propagate in direction θ_m defined by

$$\lambda_0^m = d\, n_d\, (\sin\theta_i + \sin\theta_m)\, /\, m, \tag{4-2}$$

where d denotes the grating period, n_d the refractive index of the surrounding medium, and θ_i the incidence angle. The grating order numbering is illustrated in Figure 4-8 and follows the definition by Palmer [166].

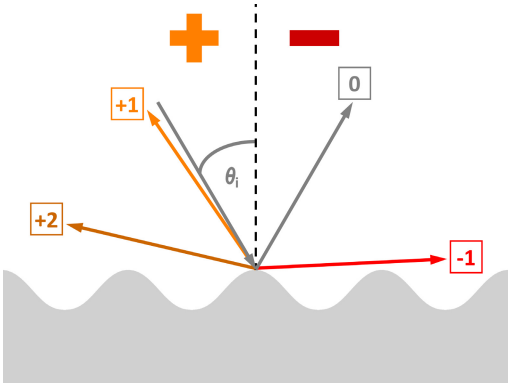

Figure 4-8. Visualization of the used grating order numbering scheme.

For the Rayleigh anomalies, these diffraction orders are grazing and propagate parallel to the surface, i.e. sin $\theta_m = 1$, and their corresponding Rayleigh vacuum wavelength λ_R can thus be calculated according to

$$\lambda_R^m = d\ n_d\ (\sin\theta_i \pm 1)\ /\ m, \tag{4-3}$$

where the sign in the bracket equals the sign of the *m*-th diffraction order [163]. For these wavelengths, there is an abrupt redistribution of energy from freely propagating ($|\theta_m| < 90°$) to evanescent ($|\theta_m| > 90°$) diffraction orders or vice versa. Rayleigh anomalies are the manifestation of surface modes, which travel parallel to the grating surface. Note that each λ_R^m is solely determined by geometrical parameters, i.e. θ_i and *d*.

Rayleigh anomalies can exist for both polarizations, although for s-polarization, where the field oscillates parallel to the grating grooves, they usually require large grating depths [165]. This is contrary to the resonant and material-dependent excitation of the second type of surface waves called Wood's anomalies after Wood, who first discovered their existence [167], but had no explanation for them [165]. Fano showed that this second type of surface waves is due to the excitation of a surface plasmon that propagates along the periodically corrugated surface [168]. The wave number k_{SP} for a semi-infinite, plane metal surface is given by

$$k_{SP} = k_d \sqrt{\frac{\varepsilon_m\ \varepsilon_d}{\varepsilon_m + \varepsilon_d}}\ ,\quad k_d = \frac{2\pi\ n_d}{\lambda_0}, \tag{4-4}$$

where ε_m denotes the metal's permittivity, ε_d that of the surrounding dielectric material, and k_d the wavenumber in the dielectric surrounding medium [3,6,165,169]. For the plasmonic metal gratings investigated here, i.e. silver and aluminum, k_{SP} is always larger than k_d. The surface waves are thus evanescent and cannot propagate in free space [165]. On the other hand, for the incident light, the wave vector component k_x parallel to the surface is defined by

$$k_x = \frac{2\pi\ n_d}{\lambda_0}\ \sin\theta_i \tag{4-5}$$

and is either smaller than k_d or equal to k_d for light incident parallel to the surface. Thus, one can only excite the surface plasmon when the wavevectors mismatch is compensated by the wavenumber of the grating k_m

$$k_{SP} = k_x + k_m, \qquad k_m = m\frac{2\pi\ n_d}{d}. \tag{4-6}$$

This is a necessary condition to ensure that the interaction of the incident light and the surface plasmon satisfies momentum conservation [165]. Contrary to Rayleigh anomalies, Woods anomalies can only be excited by p-polarized light, when the electric field is polarized parallel to the plane of incidence. For s-polarized light, excitation of surface plasmons is not possible, since they cannot fulfill the boundary condition imposed by Maxwells equations [3]. Contrary to Rayleigh anomalies that solely depend on the geometrical parameters, Wood anomalies depend also on the used metal since k_{SP} depends on its permittivity [6,165], see also Equation (4-4). This dependence will be studied and discussed in the next section.

4.4.1 Material-dependence of surface modes

Crossed gratings will be used for the experiments in this chapter and their response will be studied theoretically in Section 4.6. However, before studying such a complicated crossed grating, let us first gain insights into the response of a linear grating. Recently, Lassaline et al. showed that one can efficiently excite surface plasmons for a linear grating in silver with period *d* = 600 nm and depth *h* = 50 nm [170]. Thus, these values are used to study the influence of the grating material on the surface mode dispersion. Simulations are performed with Lumerical FDTD for a grating embedded in air, illuminated with p-polarized light and Figure 4-9 reports the corresponding dispersion diagrams, where the light line is drawn as a solid black line [83]. Any propagating mode would be on the left of the light line, while evanescent modes are on the right of the light line, where the surface plasmon's dispersion curve for a plane silver surface is located.

The plasmon dispersion is plotted as a dotted gray line and the plasmon can only be excited by adding extra momentum to the incident light by a diffraction order, see Equation (4-6). Figure 4-9(a) shows that below an angular frequency of 3000 THz this momentum is provided by the +1st-wavenumber of the grating. Above this frequency, the momentum is added by the -1 st-wavenumber of the grating and both lead to backfolding of the surface plasmon dispersion curve to the left of the light line. The additional grey dotted lines for higher energies (angular frequencies ω) are due to back-folding with higher order grating wavenumbers. Clearly visible is the reduced reflection along the backfolded surface plasmon dispersion curve in Figure 4-9 for the lowest order backfolding. This excitation of a non-radiative or dark surface mode leads to a modification of the reflection in Figure 4-9 and is usually referred to as Wood's anomaly [167].

The total reflection in Figure 4-9(a) accounts for all light reflected by the grating in any direction and thus includes all diffraction orders, which are plotted as dashed lines. Numbering and color coding of these dashed lines follow the definition in Figure 4-8, i.e. +1st-order is plotted in orange, the −1st-order in red, and the +2nd-order in dark orange. Note that in experiments, measuring total absorption requires that all diffraction orders are collected by the instrument, i.e. with a high numerical objective [170].

The direct reflection reported in Figure 4-9(b) is more relevant for visual inspection by naked eye and for spectroscopic measurements in this chapter. It corresponds to the light that is reflected to an angle matching the incidence angle θ_i. In direct reflection, besides the clearly visible dark mode, one can also observe a bright mode in Figure 4-9(b). This radiative mode is due to the excitation of a higher order surface plasmon on the silver grating. This mode is clearly visible in the direct reflection in Figure 4-9(b), while it is barely visible in the total reflection in Figure 4-9(a). The reason is that for this radiative mode, energy is added from the propagating diffraction orders to the direct reflection, thus the energy is only redistributed among the different grating orders and the total reflection remains constant. Due to this energy redistribution, the diffraction orders will have dips at these spectral locations, which can be detrimental for spectroscopic applications [166]. Figure 4-9(b) also reveals that above the two lines corresponding to +1st- and -1st-diffraction orders, direct reflection is significantly reduced as light is diffracted to these orders. They consequently alter the spectrum in direct reflection, while the 2nd-diffraction order has negligible influence owing to its low diffraction efficiency for shallow gratings [166]. Rayleigh anomalies would coincide with the dashed lines drawn for the diffraction order and cannot be excited efficiently with shallow linear gratings; they however exist for deeper gratings as shown in Section 4.4.3.

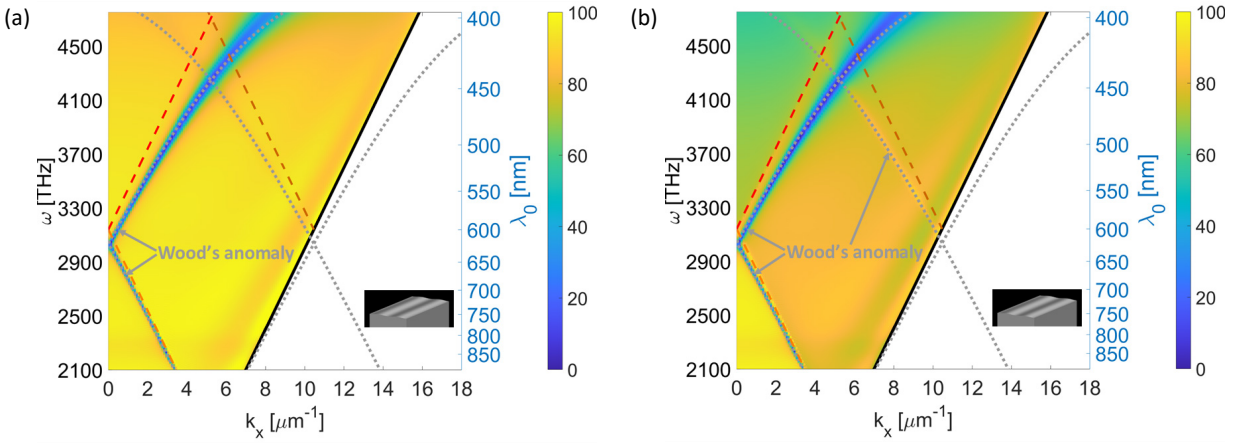

Figure 4-9. Simulated dispersion diagrams 50 nm deep for linear silver gratings in air (a) for total reflection and b) in direct reflection. The insets illustrate the corresponding simulation geometries. See text for the different lines shown in the graph.

The shape of the surface plasmon dispersion is determined by the used material. For the case of aluminum, the dispersion is much less inclined due to the higher plasma frequency of aluminum, see Figure 4-10. Consequently, the surface plasmon is excited at higher frequencies compared to silver in Figure 4-9. Furthermore, the excitation with higher diffraction orders is less efficient for aluminum than for silver, compare Figure 4-9(b) and Figure 4-10(b). Additionally, a radiative surface wave is excited by the −1st-oder, which modifies the reflection in direct reflection, see Figure 4-10(b).

The effects of this Rayleigh anomaly are only visible in Figure 4-10(b) and not for the total reflection reported in Figure 4-10(a). The reason is that the surface wave redirects light from the diffraction orders towards direct reflection and thus energy is only redistributed, i.e. the total reflected light remains constant.

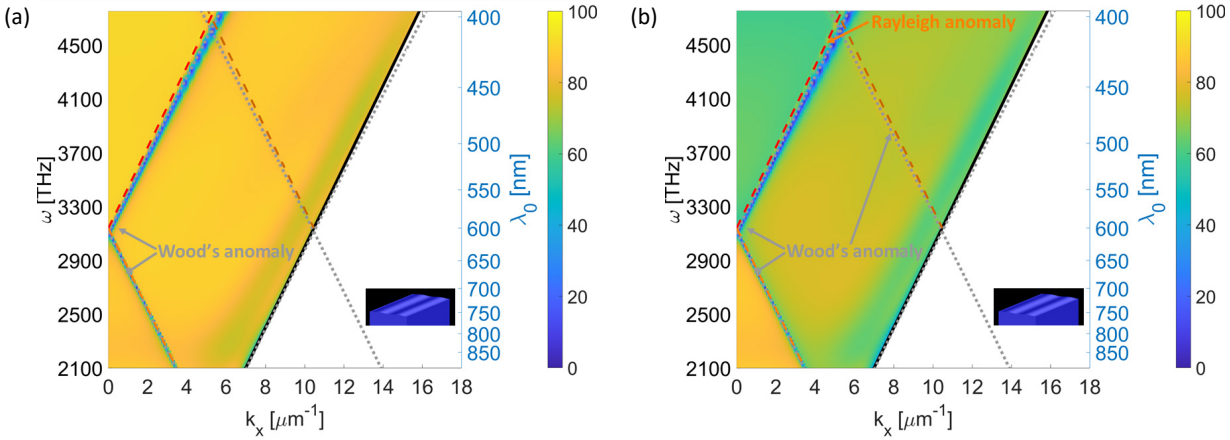

Figure 4-10. Simulated dispersion diagrams for 50 nm deep linear aluminum gratings in air
(a) for total reflection and b) in direct reflection. See text for the different lines shown in the graph.

4.4.2 Dependence on the dielectric environment and period of surface modes

The shape of the surface plasmon dispersion can also be modified by the surrounding dielectric material. The dispersion diagrams for the embedded grating in Figure 4-11(a) visualizes the total reflection of the system for varying incidence angles up to 41.81°. This is the angle that is accessible in experiments due to refraction, when the embedded grating is illuminated in air at grazing incidence, i.e. at 90°, see also Equation (2-7) (Snell's law). This illumination condition defines the maximum available wave vector magnitude and thus the air light line, which is plotted as thin solid black line in Figure 4-11. The light line in the dielectric medium with n = 1.5 is plotted as a thick black line and lies to right of the thin air light line. Embedding the linear silver gratings in a dielectric medium lowers the energies needed to excite surface plasmons, compare Figure 4-9 and Figure 4-11. Figure 4-11 also shows that the energy of the surface plasmon excited on the corrugated surface (corresponding to the middle of the blue area at a given angular frequency) is slightly lower compared to that for a surface plasmon on a planar interface (grey dotted line) as reported by Maradudin et al. [165]. This effect is even more prominent for deeper gratings as demonstrated in Section 4.4.3. Note that for clarity of the dispersion diagrams in Figure 4-11 and Figure 4-12, only the surface plasmon dispersion of effectively excited modes is plotted.

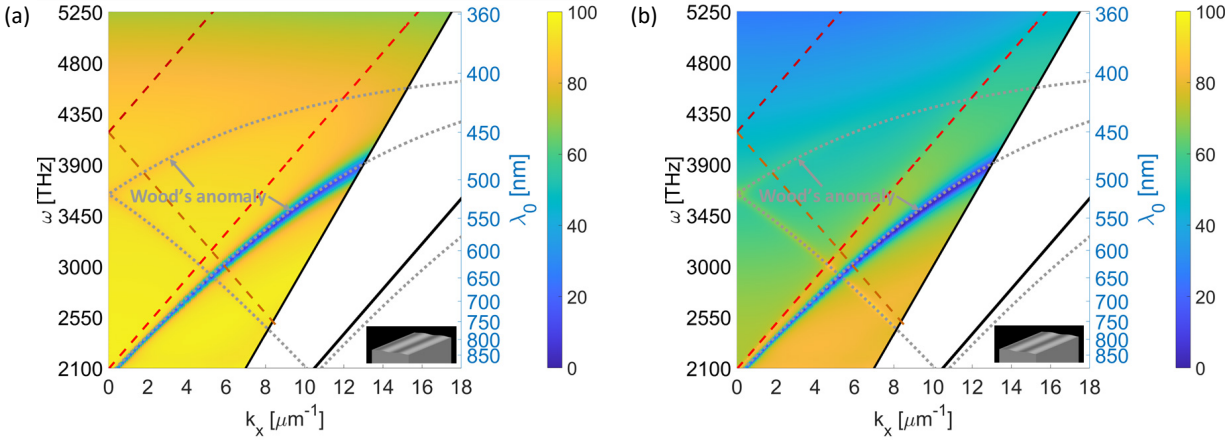

Figure 4-11. Simulated dispersion diagrams 50 nm deep for linear silver gratings in a dielectric with n_d = 1.5
(a) for total reflection and b) in direct reflection.

The energies needed for the excitation of the surface modes are lowered with increasing n_d or increasing d. For shorter periods, the surface modes energies are consequently higher as confirmed by Figure 4-12 for d = 300 nm. Note that this is also the period of the gratings, which are studied experimentally in the remainder of this chapter. The combination of this period with n_d = 1.5 leads to a dispersion diagram similar to that for a longer period in air, compare Figure 4-9 and Figure 4-12. The main difference of the grating with shorter period is that the relative depth of the grating $\mu = h/d$ is now twice as large [166,171]. This increased relative depth leads to stronger excitation of surface modes at higher energies.

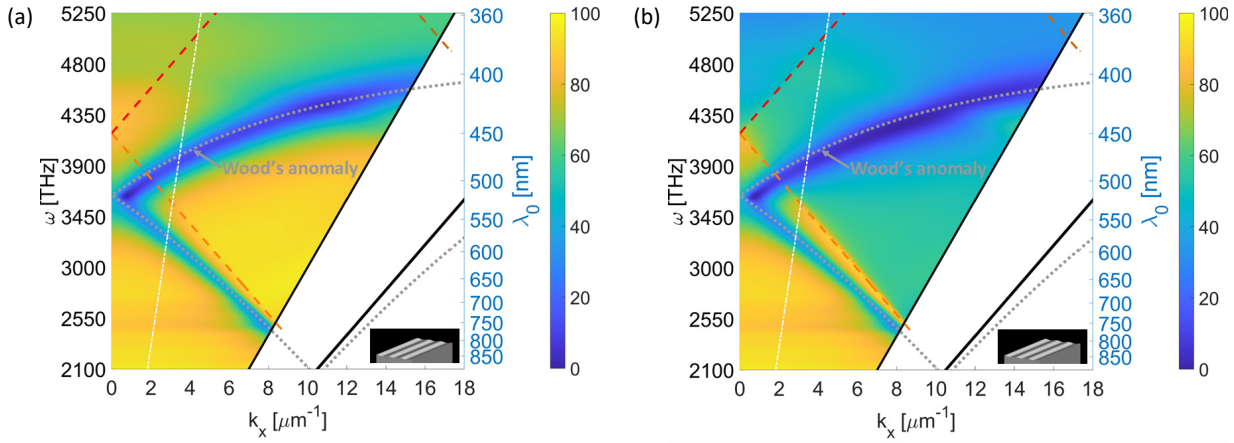

Figure 4-12. Simulated dispersion diagrams as in Figure 4-11, but with shorter period d = 300 nm
(a) for total reflection and b) in direct reflection. See text for the different lines shown in the graph.

4.4.3 Depth-dependence of surface modes

The excitation of surfaces modes strongly depends on the gratings depth as confirmed by the reflection spectra for silver gratings with d = 300 nm and varying depth in Figure 4-13. Each grating is illuminated with p-polarized light incident at 10°, which corresponds to k_x values that are indicated in Figure 4-12 with a white dash-dotted line. The values, where this lines crosses either the plasmon dispersion of a flat silver surface or the grazing diffraction order of the grating are also plotted in Figure 4-13 using identical line styles and color codes.

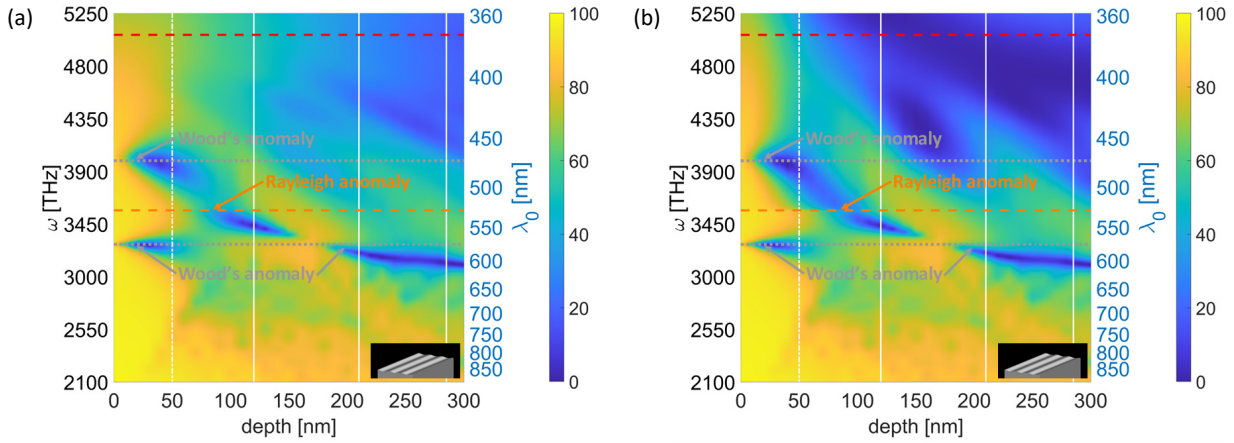

Figure 4-13. Simulated depth diagrams for linear silver gratings with varying depths d (a) for total reflection and b) direct reflection.

The reflection spectra for varying grating depths clearly show that the excitation of surface modes strongly depends on the grating depth. For gratings that are only a few nanometers deep, surface plasmon energy for a flat surface and the corrugated grating are identical as visible in Figure 4-13 at ω = 3276 THz for depths smaller than 50 nm. Increasing the grating depth further, leads to the excitation of surface plasmons with lower energy compared to a flat surface [165]. For depths above 80 nm it is at first not possible to excite surface plasmons or Wood anomalies, but one can effectively

excite Rayleigh anomalies till a depth of about 170 nm. Beyond this depth, only surface modes with energies below that on a flat surface can be excited. For gratings with depths exceeding the period, the reader is referred to works by Hooper et al., who investigated the strong deviation of the surface plasmon dispersion relation for very deep gratings consisting of either Gaussian shaped grooves [172] or ridges [173]. The solid white lines correspond to depth values for which the arc length of the sinusoidal profile equals multiples of the grating period. The white dash-dotted line at a depth of 50 nm in Figure 4-13 corresponds to the gratings investigated in Figure 4-9 to Figure 4-12.

The behavior of linear aluminum gratings in Figure 4-14 is very similar to the silver ones, although Wood's anomalies are excited at different energies as shown in Section 4.4.1. It is worth noting that only for very small grating depths one can excite Wood anomalies with higher energies around a frequency of 4770 THz as was the case for silver, where they were excited around 4100 THz. The grating depth values at which the different surface modes are excited are also very similar to the silver case. Rayleigh anomalies are excited efficiently shortly before and after the second vertical line in Figure 4-14, while Wood anomalies are excited for shallow gratings and beyond the third vertical line. The solid white lines correspond to depth values for which the arc length of the sinusoidal profile equals multiples of the grating period as in Figure 4-13.

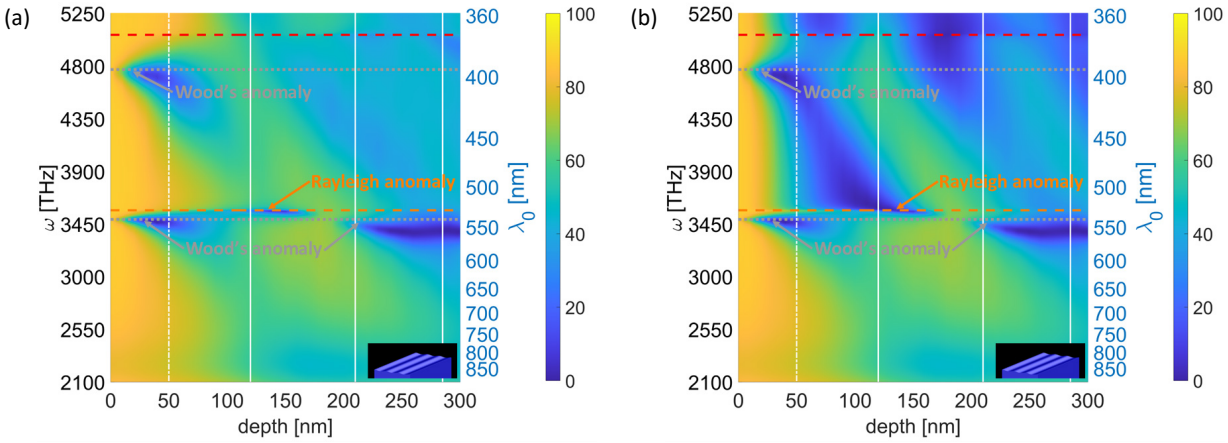

Figure 4-14. Simulated depth diagrams for linear aluminum gratings with varying depths *d* (a) for total reflection and b) direct reflection. See text for the different lines shown in the graph.

The phenomena described above exist also for two dimensions and will be investigated for crossed gratings in Section 4.6. Surface modes can also interfere like freely propagating waves and this can lead to unusual phenomena such as extraordinary transmission for sub-wavelength hole arrays [174] or strongly limiting divergence to a few degree for light transmitted by a Bull's eye structure [175]. Similar to the gratings self-color, these phenomena depend on the geometry and the optical properties of the used metals. In the case of the grating, the reflection and thus absorption is modified by these two parameters. In the next section, an alternative way to modify absorption is investigated by combining the metallic grating with a dye lacquer.

4.5 Observation of enhanced dye absorption

Inspired by works on Raman spectroscopy and fluorescence emission enhancement [151,152,155], in an initial experiment, the aluminum grating was overcoated with a micron-thick yellow dye lacquer. Surprisingly, this led to an even stronger color saturation than expected by simple addition of dye and grating absorptions, probably by strongly enhancing the intrinsic dye lacquer absorption in the blue. I hypothesize that this experimentally observed effect is caused by the interaction of the grating's near field with the thick yellow dye lacquer. To prove this hypothesis that strong dye absorption in close proximity to the grating surface is responsible for this enhancement, a much thinner and red colored

dye lacquer is applied by spincoating on the aluminized crossed gratings and on a plain aluminum surface for comparison. The red colored lacquer is chosen to clearly investigate the origin of this effect since the aluminized grating already absorbs in the blue, see Figure 4-6.

Figure 4-15(a) shows the measured absorption on flat aluminum surfaces for three investigated dye lacquers with different solid contents in solution and thicknesses as described in Section 4.2.4 and summarized in Table 4-2. Two of these lacquers have the same concentration of dye to binder (33.3 wt%, medium concentration MC), while the thinnest lacquer has a ratio of 80 wt%, high concentration (HC). Each lacquer contains at least 99% solvents to realize thicknesses smaller or equal to 50 nm and all dye lacquer layers are further encapsulated with a scotch tape of $n \approx 1.5$. The measured absorption follows the solid content concentration (1 wt%, 0.5 wt%, and 0.25 wt%, see Table 4-2) with thicker lacquers leadings to stronger absorption.

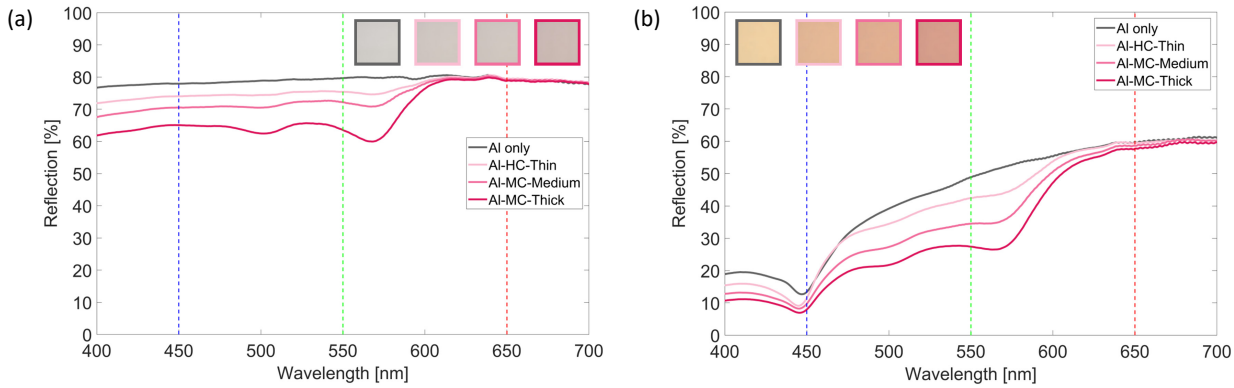

Figure 4-15. Measured reflection spectra of three different red dye lacquers applied on plane and corrugated surfaces. (a) Spectra for three embedded dye lacquers coated on aluminum substrates and the bare substrate and (b) the same conditions for a positive profile crossed grating. The insets show optical microscope images of the corresponding samples.

However, the dye's color is barely visible for the human eye even for the thickest lacquer and not at all for the two thinner ones on plane aluminum surfaces as confirmed by the insets in Figure 4-15(a). The three optical microscope images are almost identical and agree with the metallic grey appearance that is observed visually. This is in great contrast to the drastic color change of the aluminized crossed grating samples shown in the insets of Figure 4-15(b), where the color changes from a light orange to faint and then strong magenta with increasing lacquer thickness. The edge color of each microscope image in Figure 4-15 corresponds to the line color of the measured reflection spectrum.

The interaction of crossed gratings and dye lacquer enhances absorption by more than 50%, comparing the spectra for the coated grating samples in Figure 4-15(b) with the plain aluminum samples in Figure 4-15(a). In order to model and investigate the origin of this enhanced absorption, the relative transmission of the lacquers is measured on 1 mm thick polymethyl methacrylate (PMMA) substrates, see Figure 4-16(a). The relative transmission is the measured transmission of the dye lacquer coated sample divided by the transmission of a blank PMMA substrate. Based on the relative transmission, one can directly extract the approximate absorption coefficient α for the dye lacquers by the Beer-Lamberts law [176]. In a second step, the complex refractive index is retrieved by applying the Kramers-Kronig transformation to the linear related extinction coefficient κ to obtain the modification of the real part [177]. This direct approach has shortcomings for thin and highly absorbing films as it fully neglects thin film effects that can significantly alter transmission as well as reflection for the highly absorbing lacquers investigated here [178]. Consequently, an iterative approach is used to overcome these shortcomings and take interference effects properly into account [178,179]. The iterative approach thus allows for the accurate simulation of planar systems, compare Figure 4-16(a) with Figure 4-16(b), while the direct approach gave a reasonable agreement only (data not shown).

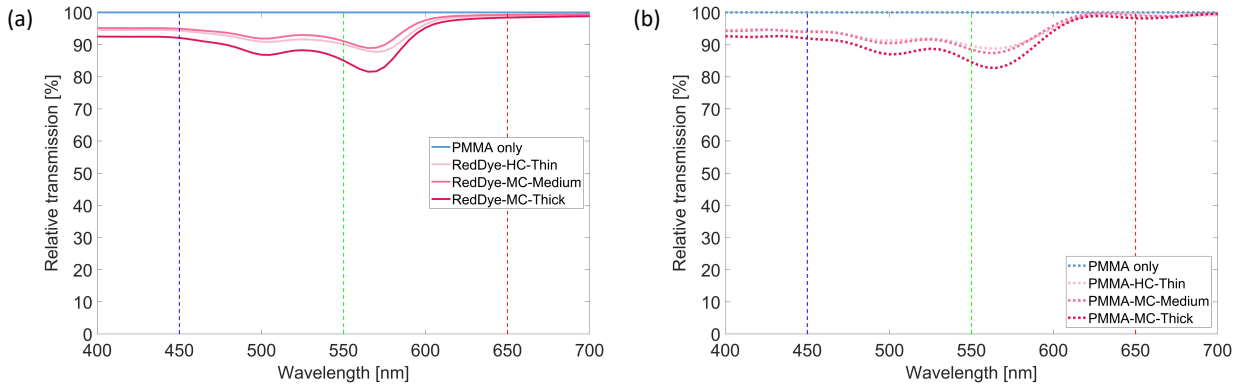

Figure 4-16. Measured and simulated transmission spectra of three different red dye lacquers on plane PMMA substrates. (a) Measured relative transmission spectra corresponding on PMMA and (b) simulated spectra.

The difference of the two approaches can be inferred by a comparison of the retrieved refractive index data in Figure 4-17. It shows that the direct method overestimates extinction and thus also leads to stronger and less accurate modification of the real part in agreement with the prediction for slightly thicker films in the infrared [179]. Alternatively, one could calculate the polarizability of individual dye molecules by measuring transmission of a weakly absorbing dye lacquer to avoid strong interference effects and then use the direct approach above as described in detail by Djorović et al. [177].

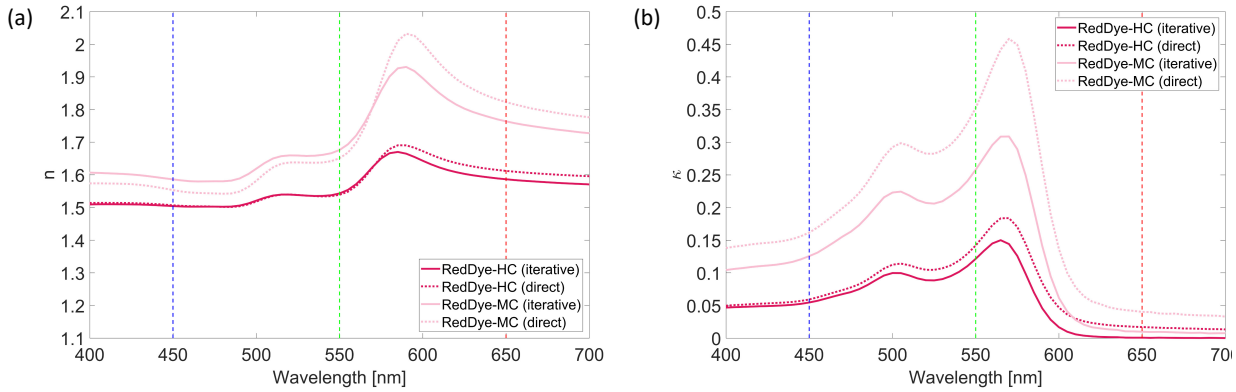

Figure 4-17. Determined refractive index data based on an iterative (solid lines) and a direct approach (dotted lines). (a) Real part *n* and (b) imaginary part *κ* of the retrieved complex refractive index.

The latter method might be even more accurate, but the achieved agreement is already very good. This can be confirmed by comparing the dotted lines of both panels in Figure 4-18 with the corresponding solid lines in the panels of Figure 4-15 for the same color code. The difference in absolute reflection values can be attributed to the encapsulation method as a simple scotch tape was used for all samples. Furthermore, the simulations in Figure 4-18(b) indicate that one could possibly even further enhance the grating systems absorption compared to the measured results in Figure 4-15(b). Thus, an even stronger color change far exceeding simple addition of both individual absorptions seems feasible. A possible reason for this slight discrepancy between simulations and experiments is that in the simulation the lacquer is overcoated conformally to the grating surface and the system is perfectly periodic. Both assumptions are difficult to fulfill perfectly in experiments as the dye lacquers was applied wet, i.e. by spin coating, and the periodicity is always slightly broken due to microscopic defects and minor shape variations from the fitted profile, see SEM images in Figure 4-1(b,c) and Figure 4-2(a).

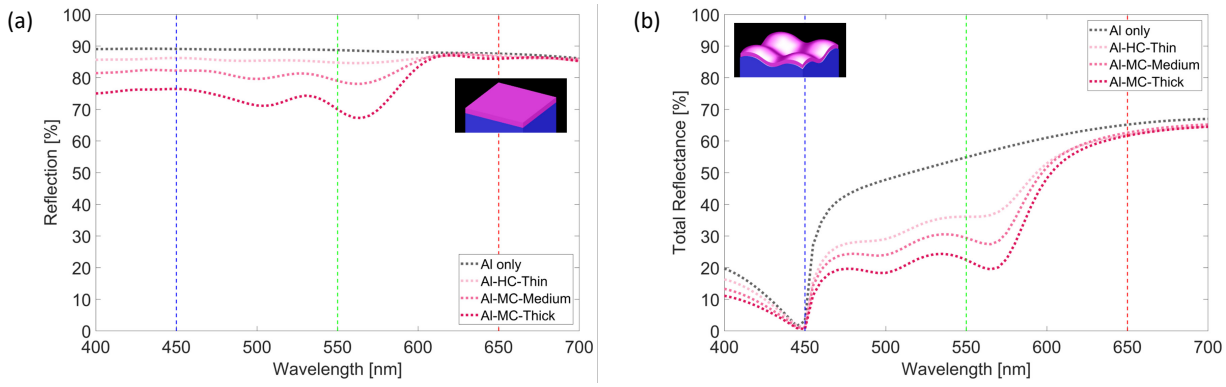

Figure 4-18. Simulated reflection spectra of three different red dye lacquers applied on plane and corrugated surfaces. (a) Spectra for three embedded dye lacquers coated on aluminum substrates and the bare substrate and (b) the same conditions for a positive profile crossed grating. The schematics illustrate the corresponding simulation geometries.

4.6 Mechanisms for absorption enhancement

The measured direct reflection spectra in Figure 4-18(b) show a clear dip at 450 nm, with and without dye lacquers. The origin of this dip and the angular dependence of the crossed grating reflection are revealed by the dispersion diagrams [147,180]. Following the discussion in Section 4.4.2 for embedded linear gratings, Figure 4-19 shows the dispersion diagrams for the embedded crossed grating without dye lacquer.

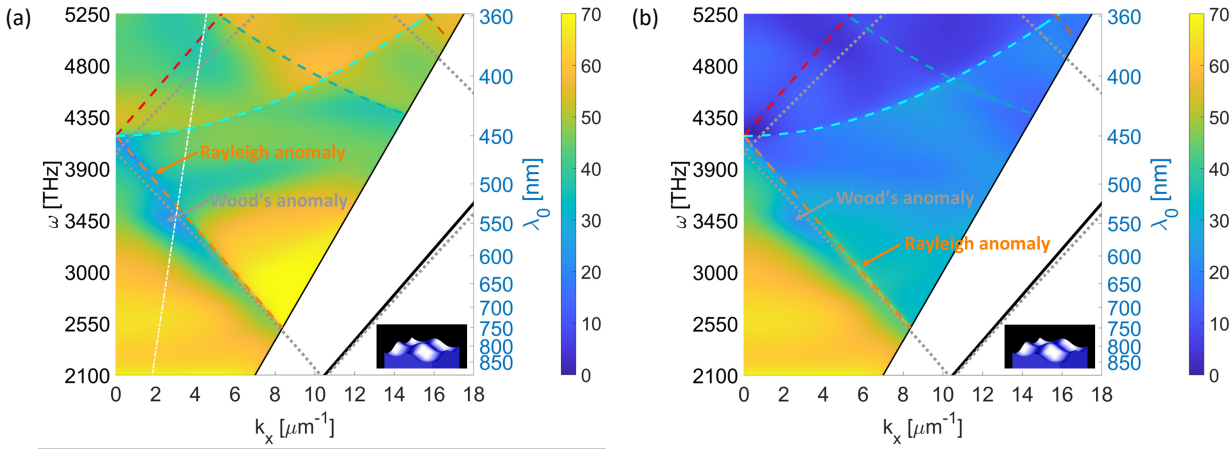

Figure 4-19. Simulated dispersion diagrams of embedded aluminum crossed gratings with a positive profile. Based on (a) total reflection and (b) direct reflection for unpolarized light illumination. The color maps show the reflection of the systems and the insets the simulation geometry. See text for the different lines shown in the graph.

The dispersion diagrams for the embedded grating in Figure 4-19(a) visualize the total reflection of the system for varying incidence angles up to 41.81°. This is the angle that is accessible in experiments due to refraction, when the embedded sample is illuminated in air at grazing incidence, i.e. at 90°, see also Equation (2-7) (Snell's law). This illumination condition defines the maximum available wave vector magnitude and thus the air light line, which is plotted as a thin black line. The light line in the dielectric medium with n = 1.5 is plotted as a thick black line and lies to the right of the thin air light line. The dispersion diagram is further overlaid with five dashed lines. The dashed lines are the propagating grazing diffraction orders, i.e. those parallel to the grating surface. The orange line corresponds to the +1st order diffraction in *x*-direction, the dark orange to +2nd order in *x*-direction, the red to −1st order in *x*-direction; the cyan to +1st and −1st orders diffraction in *y*-direction, and the dark cyan to cross terms of these orders, which correspond to diagonal diffraction orders. The order numbering is introduced in Section 4.4 for linear gratings, follows the definition by Palmer [166], and is visualized in Figure 4-8. The dashed orange and the cyan line mark energy levels at which the direct

reflection in Figure 4-19(b) significantly changes. The drastic changes in direct reflection can thus be attributed to appearing and disappearing diffraction orders [163]. The grating order energies are calculated in accordance to the detailed derivation of the Rayleigh wavelengths for grazing diffraction orders by Stewart and Gallaway [163].

When grazing diffraction orders excite a surface wave, they are typically called Rayleigh anomalies [162]. However, only the +1st order in x-direction (orange line) efficiently excites a Rayleigh anomaly as revealed for low k_x-values in Figure 4-19(a) and for large k_x-values in Figure 4-19(b). The measured intensity drop at λ_0 = 450 nm in the direct reflection spectra (k_x = 0), see Figure 4-6, coincides with a drop in the dispersion diagram in Figure 4-19(b). This is also the starting point of the orange +1st order diffraction curve. Every energy below this curve supports no propagating diffraction orders and has a generally high direct reflection.

The exception from this generally high reflection just below the dashed orange line are the signature of the second type of surface waves that can be excited, which are surface plasmons as shown in Section 4.4. The wavenumber (momentum) of a surface plasmon for a flat aluminum surface lies to the right of the light line in the dielectric for any angular frequency ω and is visualized by a grey dotted line in Figure 4-19(a). The sum of the grating's wavenumber k_m in x-direction and the momentum of the incident light k_x can however match the surface plasmon one k_{SP}, see Equation (4-6). This summation leads to backfolding of the surface plasmon dispersion to the left of the air light line and surface plasmons can thus be excited by light incident in air. For $k_x > 1.5$ a surface plasmon can be efficiently excited, which leads to a drop in total reflection by the grating. This type of surface resonance is usually called Wood's anomaly [167]. For smaller k_x-values, no Wood's anomaly is excited and thus the dip in Figure 4-18(b) at 450 nm is attributed to the excitation of a Rayleigh anomaly. Note that besides the angular frequency ω on the left vertical axis, the right vertical axes in Figure 4-19 shows selected vacuum wavelengths λ_0 to assist comparison with the spectra in previous sections.

The generally modest visibility of the Woods anomaly in Figure 4-19 is due to the fact that it can only be excited with p-polarized light as confirmed by s-polarized results in Figure 4-20(a), where no Wood's anomaly is visible as expected. Careful inspection of the results reveals that for $k_x < 1.5°\mu m^{-1}$, a Rayleigh anomaly can also be modestly excited with s-polarized light, see enlarged area in Figure 4-20(a). The p-polarized results in Figure 4-20(b) show that for $k_x > 3°\mu m^{-1}$ the Rayleigh anomaly leads to increased direct reflection (bright mode), while for smaller k_x-values the mode is dark, which is best seen in Figure 4-19(a).

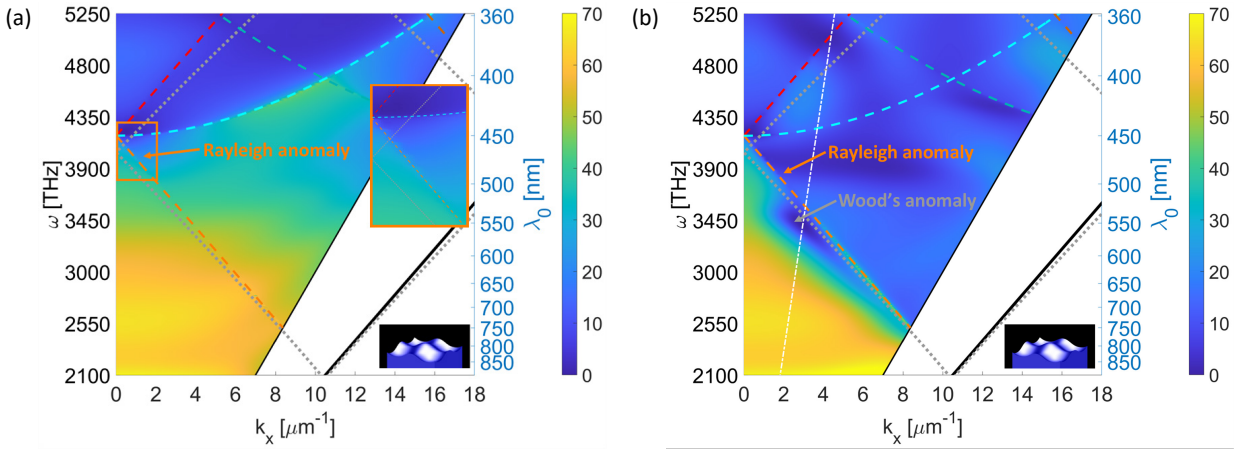

Figure 4-20. Simulated dispersion diagrams as in Figure 4-19, but for polarized illumination. (a) S-polarized results, where the orange framed inset on the right shows the enlarged simulation results of the corresponding smaller orange frame on the left and (b) for p-polarized illumination. See text for the different lines shown in the graph.

Generally, careful inspection of the dispersion diagrams is needed to identify the different modes, i.e. Rayleigh and Wood's anomalies. This is especially true when the excitation is only modest as for $k_x < 1.5°\mu m^{-1}$ and s-polarized illumination, Figure 4-20(a). Another possibility of identifying these surface modes is the simulation of the crossed gratings reflection for different depth in analogy to the results for linear gratings in Section 4.4.3. For this purpose, the crossed grating surface is described in FDTD according to Equation (4-1), but scaled to varying depths from 0 to 300 nm in 10 nm

steps. Figure 4-21 shows the resulting depth diagrams for an incidence angle of 10°, which corresponds to the white dash-dotted lines in Figure 4-19(a) and Figure 4-20(b). Note that the incident light in Figure 4-21(a) is also p-polarized to allow easier identification of the excited Wood's anomalies. The grating depth of 172 nm for the simulation results in Figure 4-19 and Figure 4-20 is marked in Figure 4-21 by a dash-dotted white line. Around this depth, one can excite both kinds of anomalies, Rayleigh and Wood's ones with the lowest energy. For shallower gratings with depths of up to 100 nm one could also excite a Wood's anomaly with higher energy (ω = 4769 THz), while for gratings depth greater 250 nm modest excitation of a higher energy Rayleigh anomaly is possible (ω = 4251 THz). Figure 4-21 further reveals that only for grating depths in the range 150-190 nm it is possible to excite Rayleigh anomalies efficiently with p-polarized illumination.

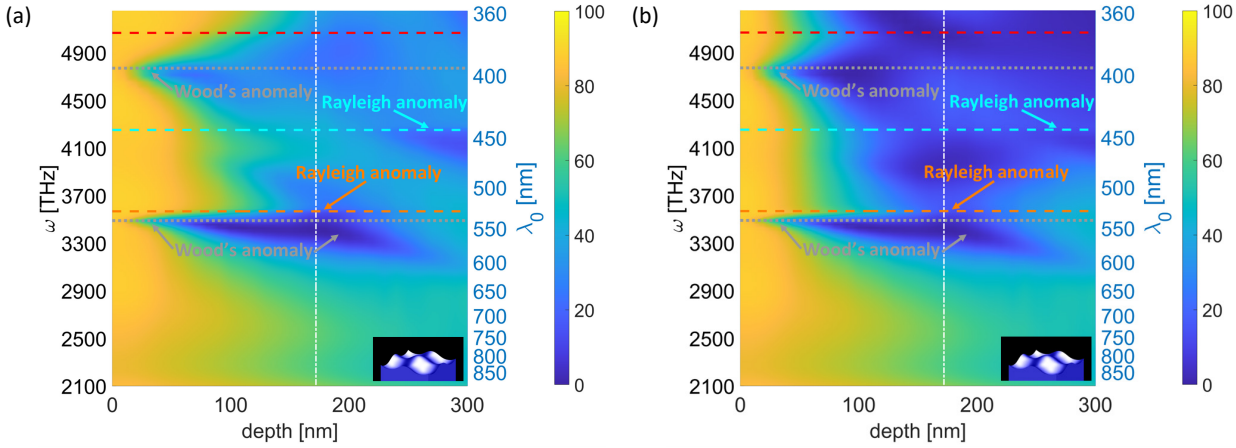

Figure 4-21. Simulated depth diagrams of embedded aluminum crossed gratings with a positive profile. Based on (a) total reflection and b) direct reflection, for p-polarized illumination. See text for the different lines shown in the graph.

The results in Figure 4-21(b) show that the excitation of both, lowest order Rayleigh and Wood's anomaly, reduces direct reflection significantly for p-polarized light incident at 10°. For light incident at 0° ($k_x = 0$), the measured intensity drop at $\lambda_0 = 450$ nm in the direct reflection spectra with unpolarized light, see Figure 4-6, is solely attributed to the excitation of a Rayleigh anomaly. The spectral modifications associated with these anomalies are rather narrow, while broadband and strong modifications can be observed when applying dye lacquers as reported in Figure 4-15(b). The two absorption peaks of the thick dye lacquer at 500 nm and 565 nm observed in Figure 4-17 are also prominent in the dispersion diagrams in Figure 4-22. The solid magenta lines mark these absorption peaks, which are independent of the incident angle as expected.

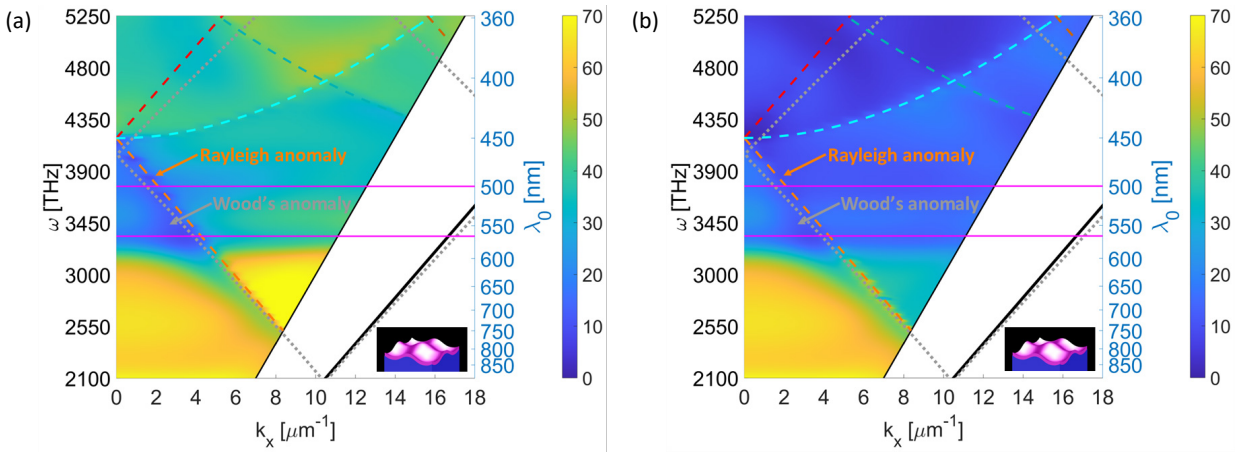

Figure 4-22. Simulated dispersion diagrams of crossed gratings as in Figure 4-19 overcoated with a 50 nm thick dye lacquer. Based on (a) total reflection and (b) direct reflection for unpolarized light illumination.

This broadband and strong reduction in reflection could be caused by the coupling of the surface modes with the localized absorption of the dye. Strong coupling of the surface modes supported by the grating with the dye absorption

bands should result into avoided crossing of the corresponding lines in Figure 4-22 [181]. This effect is not visible in Figure 4-22, neither for the total reflection in panel (a) nor in direct reflection in panel (b). The effect of strong coupling could be obscured by the very broadband absorption of the dye, which leads to significant reduced reflection slightly beneath and above the peak absorption wavelength of 565 nm. To exclude the effect of this broadband absorption and significantly faster 2D computations in FDTD, the effect of grating-dye-coupling is first studied for a linear aluminum grating. The grating is conformally overcoated with an artificial dye lacquer that has an absorption peak in the green at 565 nm and a Gaussian shaped absorption profile with a full width half maximum of 5 nm in close analogy to the results reported in the next section. The maximum extinction coefficient κ (imaginary part of the complex refractive index) is chosen to be 0.2 for this 50 nm thick dye lacquer. The resulting dispersion diagrams in Figure 4-23 clearly show an avoided crossing at $k_x = 3.9°\mu m^{-1}$ and thus there is grating-dye-coupling for the linear case. The excited surface plasmon mode, which manifest as a Wood's anomaly avoids crossing with the dye's absorption at $\omega = 3334$ THz. This also leads to slightly lower energy before the crossing and higher energy after, for the dye mode as expected for mode coupling.

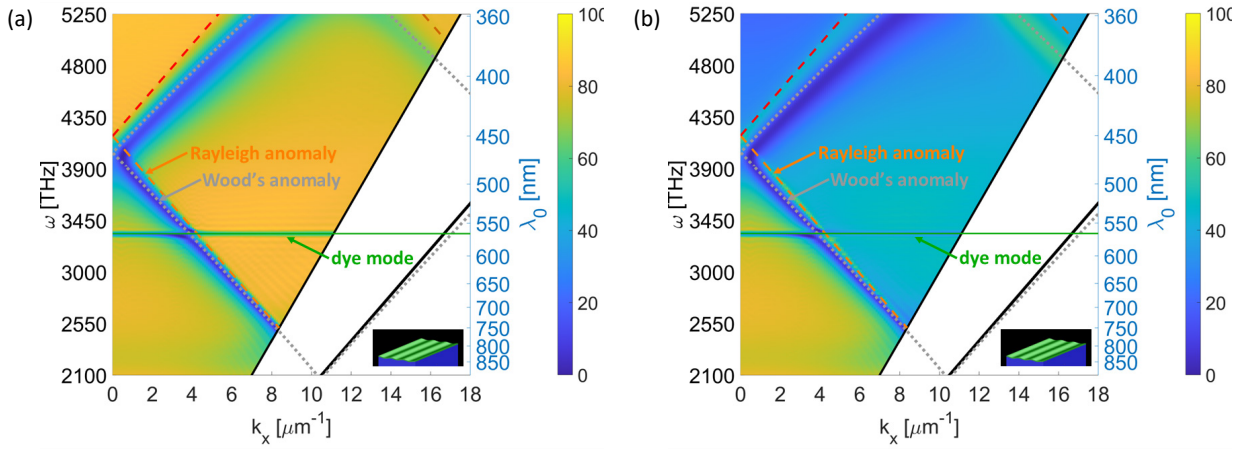

Figure 4-23. Simulated dispersion diagrams for 50 nm deep linear aluminum gratings overcoated with a dye lacquer (a) for total reflection and b) in direct reflection. See text for the different lines shown in the graph.

Dispersion diagrams based on simulations for a 50 nm thick conformal dye lacquer on the crossed grating are shown in Figure 4-24. The clearly observed anti-crossing of the modes in Figure 4-23 is not present in Figure 4-24, despite identical narrowband absorption parameter for the dye lacquer. The only sign of interaction between the dye and the excited surface modes on the crossed grating is a slight broadening of the dye's absorption for k_x-values in the range 2 – 4 μm^{-1}. Consequently, the direct reflection reported in Figure 4-22(b) and Figure 4-24(b) is not significantly altered due to grating-dye coupling.

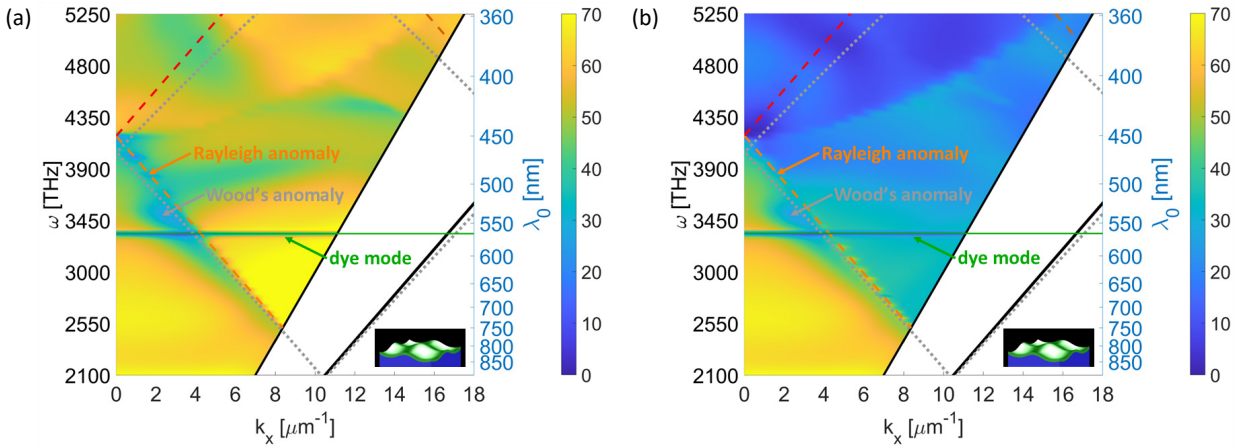

Figure 4-24. Simulated dispersion diagrams of crossed gratings overcoated with a narrowband absorbing dye lacquer. Based on (a) total reflection and (b) direct reflection for unpolarized light illumination.

The dye's absorption enhancement on top of the aluminum crossed grating compared to flat aluminum surfaces as reported in Figure 4-18 must thus have a different cause. The absorption enhancement is attributed to the local field enhancement, which is already noticeably stronger for a flat aluminum surface compared to a flat PMMA surface due to high reflection at the aluminum interface, compare intensity distributions in Figure 4-25(a) and Figure 4-25(b), where a 50 nm thick dye lacquer (MC-Thick) is applied on both surfaces.

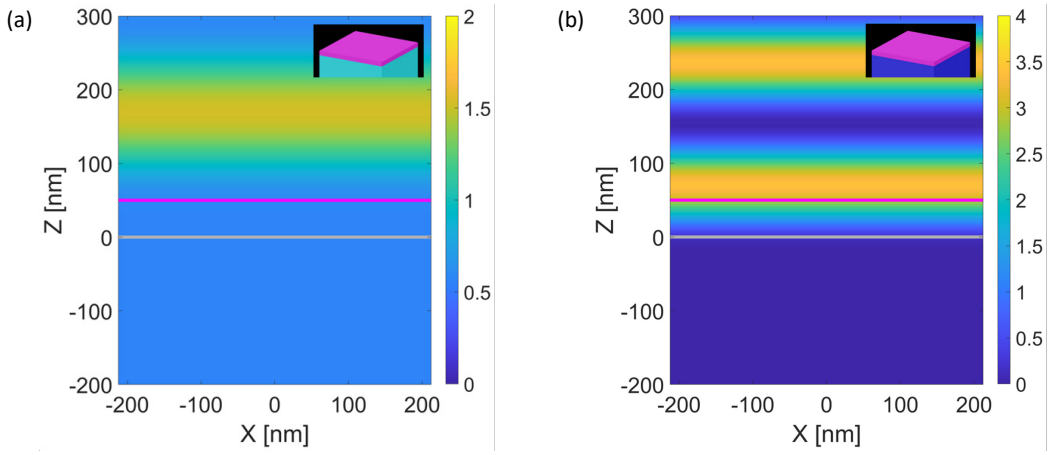

Figure 4-25. Simulated intensity distributions for flat surfaces at λ_0 = 500 nm. (a) PMMA substrate overcoated with a 50 nm thick dye lacquer and (b) overcoated aluminum substrate. The insets in each panel show the corresponding simulation geometries.

The simulations are evaluated at λ_0 = 500 nm, where the complex refractive index of the dye lacquer is about 1.52 + 0.10i, which differs only marginally from the constant dielectric embedding material and PMMA index of 1.5. Consequently, the standing wave pattern maximum intensity for the PMMA system within the whole simulation region is smaller than 1.54 and smaller than 0.59 at the top of the dye lacquer and relatively constant within the 50 nm thick dye lacquer. On the contrary, the maximum intensity above a flat aluminum surface is smaller than 3.74 within the whole simulation region and around 2.92 at the top interface of the dye lacquer and 0.21 at the bottom. The maximum possible intensity for such a two beam interference is four [161], but the slightly lower value of 3.74 observed here results from the "only" 93.5% light reflection at λ_0 = 500 nm for the aluminum surface. On average, the intensity is about 1.51 within the dye lacquer and thus more than twice larger compared to the case of the dye lacquer above the PMMA surface. The formed standing wave pattern atop the aluminum surface, clearly visible in Figure 4-25(b), is thus the main reason for the about twice higher absorption within the dye lacquer above aluminum compared to PMMA with a rather modest homogenous intensity distribution, see Figure 4-25(a).

The field enhancement caused by the crossed grating is significantly larger. The mean intensity for the 1% highest intensity values within the whole simulation area is 25.4 for the embedded grating in Figure 4-26(a) and 16.3 for the grating overcoated with a 50 nm thick dye lacquer, see Figure 4-26(b). The peak values can be extracted from the corresponding color bars, which are the rounded-up integer values of the maximum intensity value. In the case of an embedded grating, the peak and mean intensity values exceed the theoretical maximum value of four for two beam interference by more than a factor of six [161]. This strong field enhancement is attributed to the standing wave patterns resulting from propagating and evanescent grating orders [173,182].

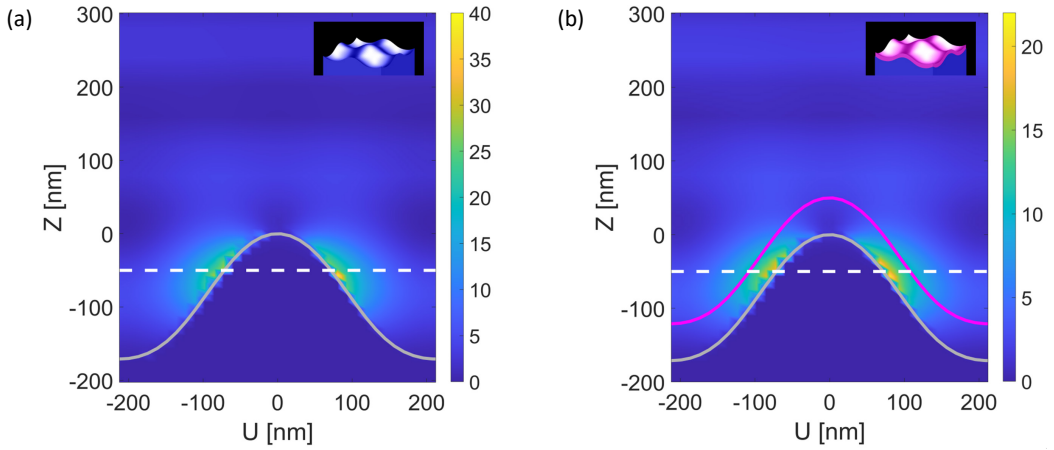

Figure 4-26. Simulated intensity distributions for corrugated surfaces at λ_0 = 500 nm. (a) Positive profile grating without and (b) with a 50 nm thick dye conformally coated lacquer. The insets show the corresponding simulation geometries.

The magenta-colored solid line in Figure 4-26(b) marks the top surface of the dye lacquer, while the grey colored solid lines in Figure 4-25 and Figure 4-26 mark the top surfaces of aluminum or PMMA, respectively. The white dashed lines at *z* = -50 nm in Figure 4-26 are the locations of the *xy*-crosscuts shown in Figure 4-27. Both patterns clearly show that the field enhancement is along the polarization of the incident light, the *u*-direction. Note that the *uz*-crosscuts in Figure 4-26 were taken along the *u*-direction marked by the diagonal white dashed lines in Figure 4-27.

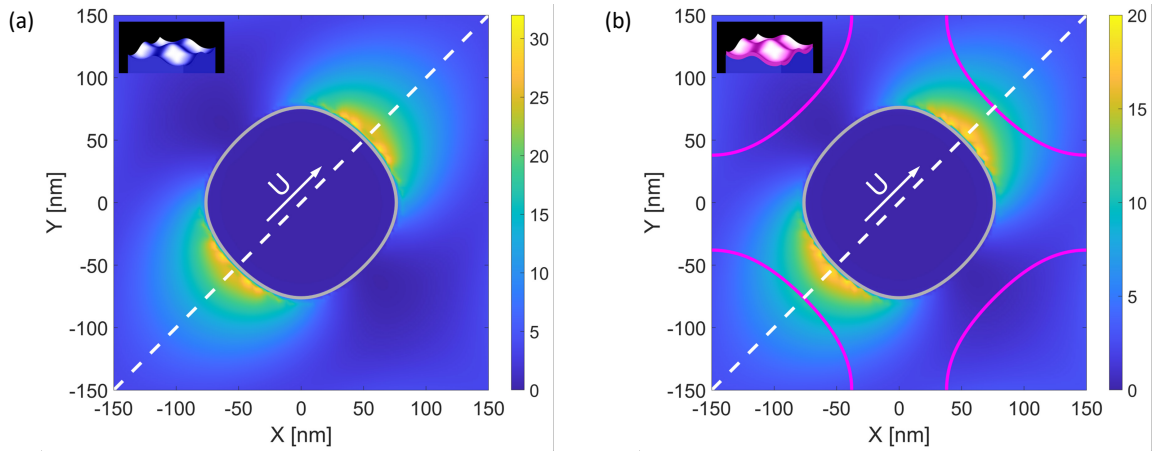

Figure 4-27. Simulated intensity distributions along *xy*-crosscuts at the locations marked by the dashed white lines in Figure 4-26. (a) Positive profile grating without and (b) with 50 nm thick dye lacquer. The insets show the corresponding simulation geometries.

The rescaled plot in Figure 4-28(a) of Figure 4-27(b) shows that the exceptional high intensity region exceeds the lacquer boundaries marked again by a magenta-colored line. Intensity values exceeding four are plotted in red. The value of four is chosen as it is the maximum intensity enhancement for flat surfaces [161]. Thus, one could enhance absorption even further with slightly thicker dye lacquers. The logarithmically scaled plot of the intensity distributions in Figure 4-28(b) highlights that the enhancement resembles a dipolar emission pattern.

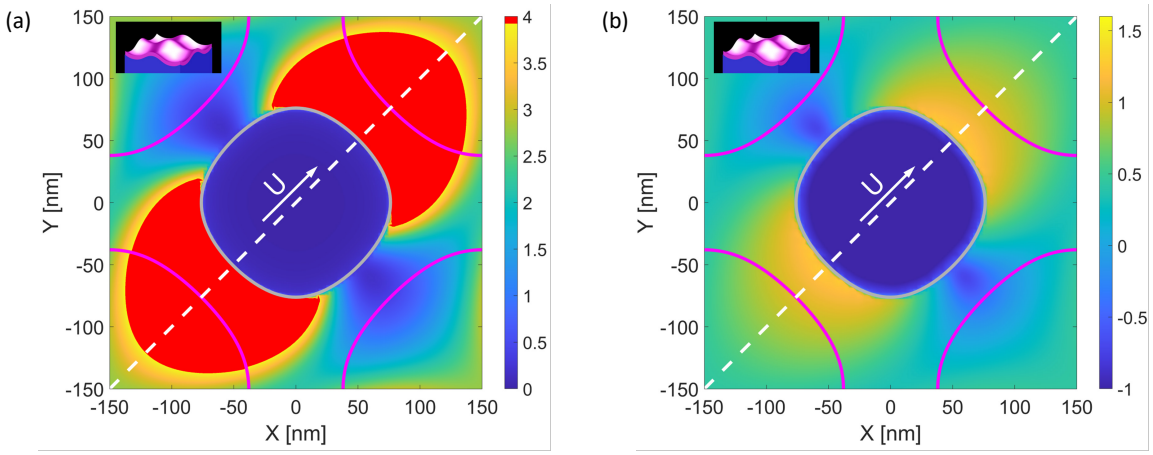

Figure 4-28. Replotted simulated intensity distributions for corrugated surfaces as in Figure 4-27(b). (a) Rescaled to a maximum value of four (higher values are plotted in red) and (b) logarithmically scaled intensity distribution.

4.7 Demonstration of color gamut enhancement

The previous results demonstrate that applying a dye lacquer on top of a crossed grating, leads to a strong absorption enhancement within the dye lacquer compared to the same lacquer on top of a plane aluminum interface. On one hand, this potentially enables one to apply less dye for the same absorption and associated color appearance. On the other hand, it also provides a mean to greatly tune the color appearance of the system in direct reflection by modifying the dyes absorption band as will be outlined below.

To study this effect with simulations, five artificial dye lacquers with corresponding complex refractive indices are created, see Figure 4-29. Their absorption peaks are located at chosen central wavelengths λ_c that span from 450 nm to 650 nm in 50 nm steps and have a Gaussian shaped absorption profile with a full width half maximum of 33.3 nm. The chosen simple absorption shape is very easy to depict visually in all the results below.

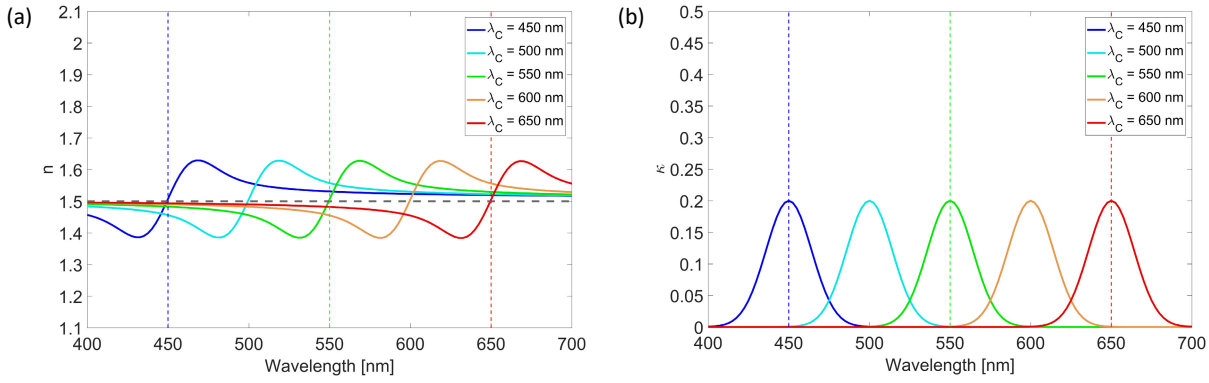

Figure 4-29. Calculated refractive index for the artificial dyes. (a) Real part n with an additional dashed grey line indicating the approximate refractive index of the dye lacquers binder and (b) imaginary part κ of the retrieved complex refractive index data.

The maximum extinction coefficient κ (imaginary part of the complex refractive index) is kept constant at 0.2, while the thickness of the dye lacquer is varied for each central wavelength λ_c with its associated color. This ensures that when light passes the lacquer once, the transmitted intensity I is constant at λ_c for all layers according to the Beer-Lambert law

$$I = I_0 \exp(-\alpha d_c) = I_0 \exp(-4\pi\kappa d_c/\lambda_0), \tag{4-7}$$

where I_0 denotes the incident intensity, α the absorption coefficient, κ the imaginary part of the dye lacquers refractive index, λ_0 the vacuum wavelength and d_c the color-dependent thickness of the dye lacquer [176,183]. To keep the transmitted intensity value constant for all five dye lacquers, d_c is varied according to

$$d_c = d_{550}\, \lambda_c \,/\, 550\ \text{nm}, \tag{4-8}$$

where d_{550} is the thickness of 50 nm for the green absorbing dye lacquer at λ_0 = 550 nm. Blue absorbing dye lacquers will thus be thinner and red absorbing ones thicker. This variation leads to nearly constant absorption for all five dye lacquers applied on top of aluminum or PMMA substrates, as confirmed by Figure 4-30. This is in contrast to the results in Figure 4-16 as the absorption band in the present calculations is narrower and the lacquer thickness is adapted to the peak absorption at λ_c for each band. This effectively balances out by design the standing wave enhancement due to the reflected light at planar interfaces for all five lacquers [178].

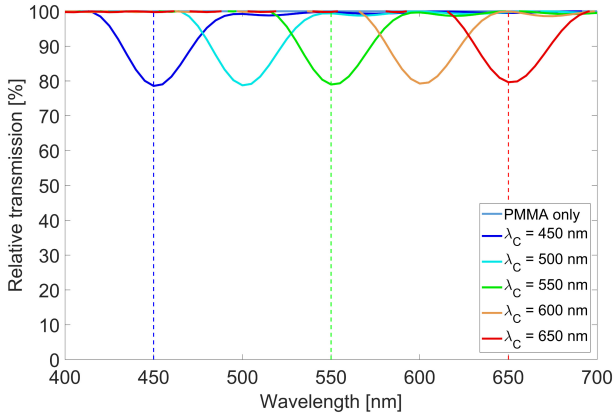

Figure 4-30. Simulated relative transmission of five different dye lacquers applied on plane PMMA surfaces.

Applying the lacquer conformally on top of a positive profile crossed grating leads again to a strongly enhanced absorption of the dye lacquer, compare Figure 4-31(a) and Figure 4-31(b). This enhancement by the grating is nearly independent of the wavelength, which is somewhat unexpected. It is attributed again to strong near-field enhancement caused by propagating and evanescent grating orders. It is truly remarkable that the grating supports a nearly constant enhancement across the entire VIS.

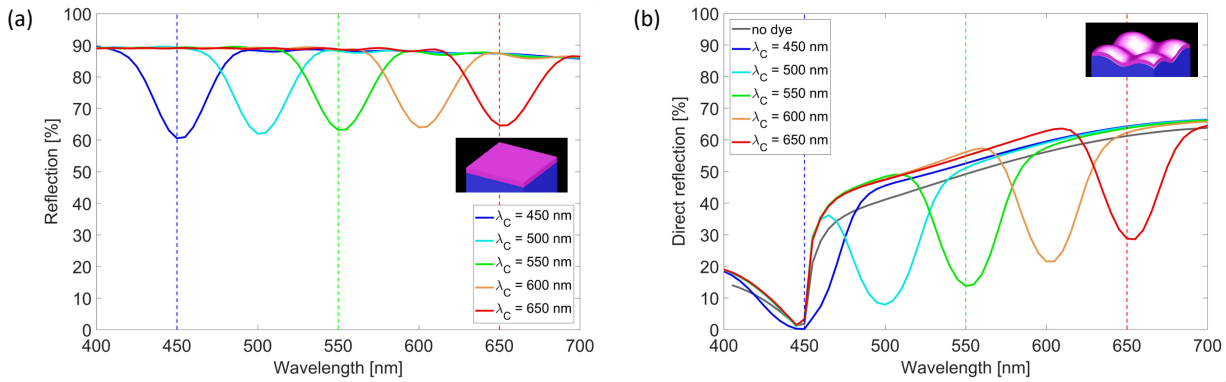

Figure 4-31. Simulated response of five different dye lacquers applied conformally on plane surfaces and crossed gratings. (a) Simulated reflection spectra for five embedded dye lacquers coated on aluminum substrates and (b) spectra for a positive profile crossed grating conformally overcoated with these lacquers. The insets on the right of each panel show a schematic visualization of the modelled systems.

Based on the simulated spectra, the color coordinates for a chromaticity diagram for a D65 light source (CIE 1964) are calculated [184]. Comparing the chromaticity diagrams in Figure 4-32(a,b) confirms that the crossed grating significantly widens the possible color gamut. The resulting color area is more than five times larger compared to the one obtained

for a flat aluminum substrate, confirming the strong color enhancement possibilities of the system. This comes at the cost that the resulting colors are not anymore centered around the white point, but somewhere around a light orange, corresponding to the grating color impression without lacquer, marked also by a grey circle in Figure 4-32(b).

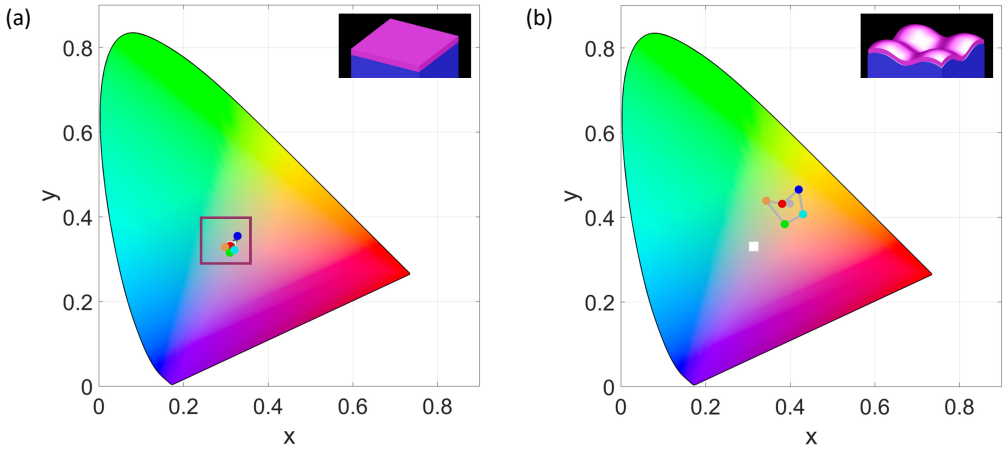

Figure 4-32. Chromaticity diagrams of the corresponding systems in Figure 4-31. The insets on the top right of each panel show a schematic visualization of the modelled systems.

The calculated color coordinates are marked by colored circles in Figure 4-32 that match the colors used for the spectra in Figure 4-31. Additionally, the location of an uncoated aluminum mirror is added to the diagram as a grey circle in Figure 4-32(a), which is close to the white point marked by a white square and resulting from the nearly uniform reflectivity across the visible spectrum, see Figure 4-31(a). The chromaticity diagram for the plane aluminum system also reveals that, albeit the clearly visible absorption in Figure 4-31(a), the produced colors are all located at or very close to the white point. The grey lines connecting the colored disks span a very small area that should be accessible by mixing the dye lacquers. The points are so close that only the enlarged part of the diagram in Figure 4-33 clearly reveals the location of each dye lacquer coated system. This enlarged area is framed by a purple line matching the color code of the overlaid square in Figure 4-32(a).

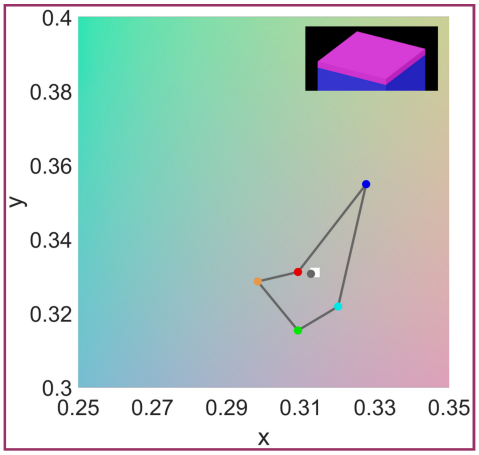

Figure 4-33. Enlarged part of Figure 4-32(a) to clearly visualize the area spanned by the five dye lacquers around the white point.

This color gamut can be increased even further by applying artificial dye lacquers with three times larger FWHM of 100 nm and double thickness, see Figure 4-34. The increased bandwidth and thicker dye lacquers lead to significantly higher absorption comparing Figure 4-34(a,b) with Figure 4-31(a,b). This in turn leads to a much wider color gamut of both systems, flat and corrugated. The color gamut spanned by the systems in Figure 4-34(c,d) is factors larger than those in Figure 4-32(a,b). The color gamut for the corrugated system in Figure 4-34(d) is still significantly larger than the one for the flat systems in Figure 4-34(c), confirming that strong enhancement is also possible with thicker lacquers. The difference is less significant compared to the thinner lacquers used for the results in Figure 4-32, but still remarkable. The ideal lacquer thickness for maximum enhancement is probably in the range 60-70 nm.

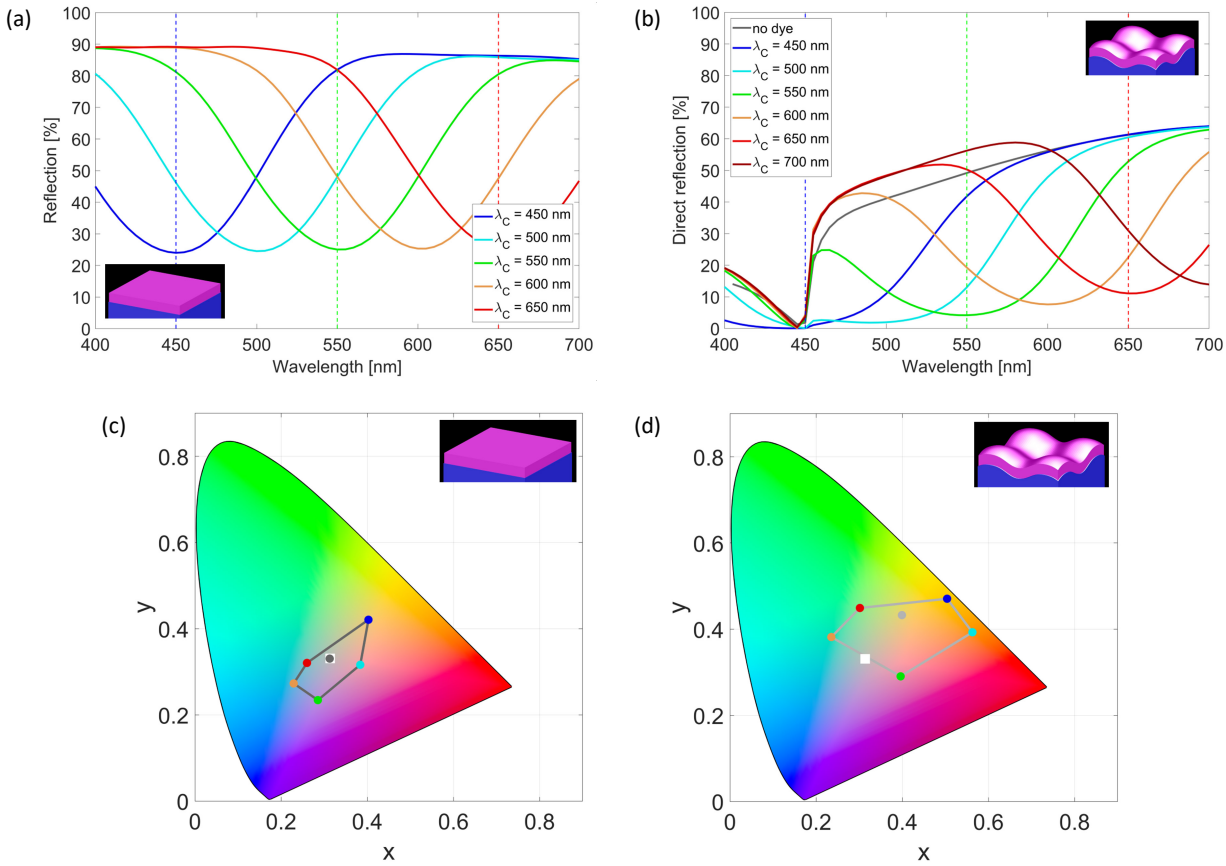

Figure 4-34. Simulated response of five different dye lacquers applied on plane surfaces and crossed gratings. (a) Simulated reflection spectrum for five 100 nm thick embedded dye lacquers with a 100 nm FWHM coated on flat aluminum substrates. (b) Spectra for a positive profile crossed grating conformally overcoated with these lacquers. (c,d) Chromaticity diagrams for the systems in panel (a,b). The insets in each panel visualize the corresponding simulation geometries.

The maximum extinction coefficient κ (imaginary part of the complex refractive index) is again kept constant at 0.2 for the results in Figure 4-34. This is also clearly depicted in Figure 4-35(b), where κ is plotted for the five broader absorbing dye lacquers with a FWHM of 100 nm, showing that the absorption peaks are again located at chosen central wavelengths λ_c that span from 450 nm to 650 nm in 50 nm steps. This ensures that when light passes the lacquer once, the transmitted intensity I is constant at λ_c for all layers according to the Beer-Lambert law, see Equation (4-7). Note that the increased absorption bandwidth leads to noticeably stronger modifications of the refractive index real part n as expected, comparing Figure 4-29(a) and Figure 4-35(a).

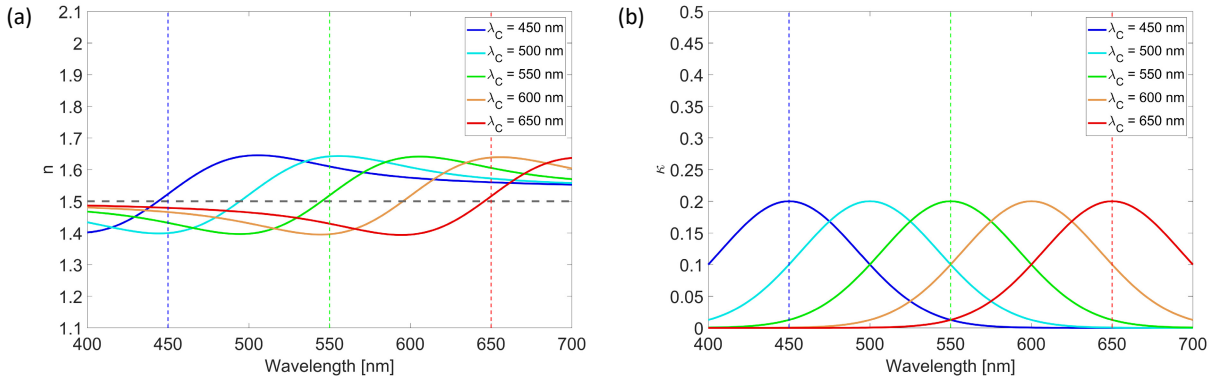

Figure 4-35. Calculated refractive index data of the artificial dyes that are used for the results in Figure 4-34 (lines have identical color code). (a) Real part n with an additional dashed grey line indicating the approximate refractive index of the dye lacquers binder and (b) imaginary part κ of the retrieved complex refractive index data.

One can realize with this broader absorbing dye lacquers atop the grating all colors except blue, because of the grating light orange self-color, grey dot in Figure 4-34(d). This orange color is mainly a result of the very low reflection below the gratings resonant reflection minimum at 450 nm. The wavelength of the minimum is solely determined by the grating period, see Figure 4-36, while the minimum reflection value depends on shape and depth, see Figure 4-3 and Figure 4-7, respectively.

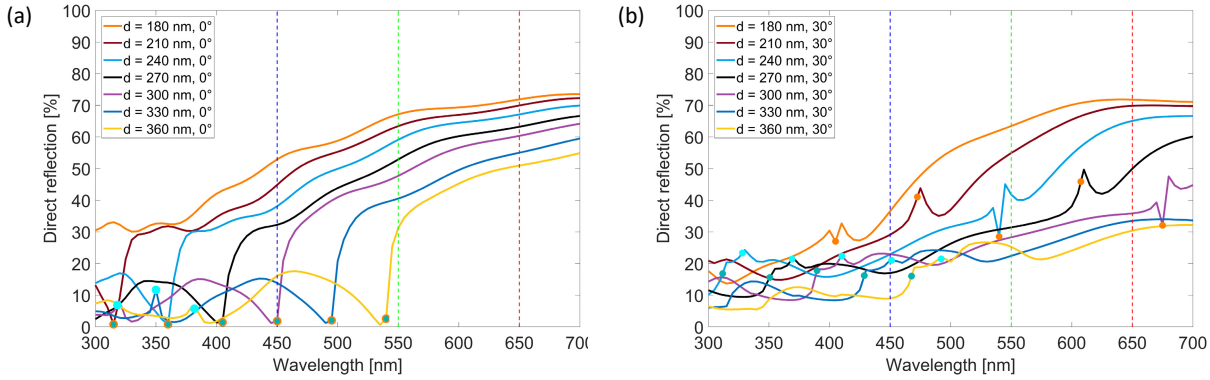

Figure 4-36. Simulated reflection spectra of positive profile crossed gratings with seven different periods *d* (heights scaled linearly to the initial period of 300 nm). (a) Simulated spectra for zero incidence angle and (b) spectra for 30° incidence angle. The dots correspond to glazing diffraction orders and are color coded in agreement with the dotted lines of the dispersion diagrams in Figure 4-19.

Consequently, a shorter pitched grating with its resonant absorption in the UV rather than in the blue at 450 nm could indeed be used to realize all colors. Initial simulations based on a grating with a 210 nm (brown line in Figure 4-36) instead of a 300 nm period show that it is indeed possible to create a large color gamut around the white point, see Figure 4-37(b). The grating depth of this short-pitched grating is 120 nm as the depth is scaled linearly to the 30% reduction of the period. This very simple scaling approach increases already the achievable color gamut compared to a flat surface, comparing Figure 4-34(c)and Figure 4-37(b), but can likely be increased further by exploring slightly thinner lacquers and optimizing the grating profile for this shorter pitch.

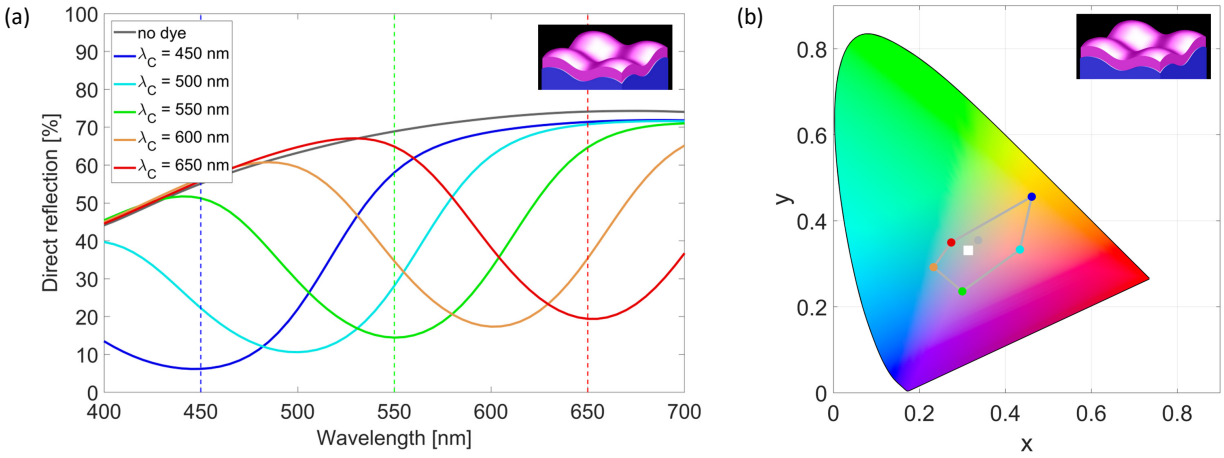

Figure 4-37. Five different dye lacquers applied conformally on positive profile crossed gratings with a period of 210 nm. (a) Simulated reflection spectra for nm thick dye lacquers (b) Corresponding chromaticity diagram of the systems. The insets in each panel show a schematic visualization of the modelled systems.

4.8 Conclusion

Baffled by an observed color change upon embedding of a corrugated surface in the form of a metallic crossed grating, I have investigated the origin of wavelength-dependent absorption and showed that material, shape, and dielectric environment of the corrugation determine the resulting gratings self-color. Inspired by works on fluorescence emission

enhancement, the crossed grating is coated conformally with three different dye lacquers. It is shown that the interaction of almost colorless appearing dye lacquers can be significantly altered and enhanced by its interaction with a grating, enhancing absorption locally by more than a factor of 20. The enhancement of the dye lacquers intrinsic absorption was attributed to strong local field enhancement caused by propagating and evanescent diffraction orders. For a set of artificial dye lacquers, it was shown how the achievable color gamut of these lacquers can be significantly enhanced when they are conformally coated as a very thin layer (<100 nm) on top of a corrugated surfaces compared to coating flat surfaces with the same lacquers.

I believe that these findings will find application in bio sensing [185], especially for those relying on visual inspection like the pregnancy test. The methodology allows for applying minute amounts of an almost colorless substance on top of the corrugated surface to create a drastic and clearly visible color change [186,187]. The fact that very thin layers of these substances are sufficient makes the principle especially promising for any application that relies on diffusion of e.g. a gas into the lacquer to produce absorption within minimal diffusion times [188,189]. Applications could include fast gas sensors and PH detectors and other possible applications are listed in Section 4.8.2 below. The sub-micron thickness also minimizes the amount of any substance needed for detection, such that scare, difficult to produce or extremely expensive substances can be employed for sensing.

Besides sensing, I can also envision applications in document authenticity protection. The lithographic combination of mirror and grating elements or the combination/rasterization of different crossed gratings with the same dye lacquer can be used for printing with sub-micron resolution. The dyes absorption will be enhanced locally depending on the corrugated or flat surface beneath it.

4.8.1 Comments on industrial scalability

The fabrication of metallized linear and crossed gratings is state-of-the art in modern foil production on roll-to-roll-basis. The mass fabrication of these structures is an essential part in current OVDs that are used for the protection of document authenticity [40]. The combined system reported in this Chapter needs an additional step compared to traditional metallized OVDs, the wet coating of the dye lacquer. This step can also be executed in a roll-to-roll manner after replication of the grating and evaporation of an aluminum layer. Each of these three successive steps is carried out today individually, the combination and thus industrialization of the system seems to be very feasible.

However, while applying roll-to-roll technologies like gravure printing for wet coating of thin lacquers is state-of-the-art [190], the formulated lacquers in Section 4.2.4 pose a challenge. The high solvent content greater or equal to 99% demands dedicated coating machines to prevent explosions. Further, using toluene in large quantities is not desirable as it is potentially ototoxic [191] and (abuse) can cause severe neurological harm [192,193]. This is also reflected in the ban for distribution of consumer goods in the European Union that contain more than 0.1 wt% of toluene in a mixture, adhesive, or spray paints [194]. Besides this safety issues, toluene easily dissolves many polymers, so one must avoid diffusion to the underlying gratings that are typically replicated in polymers [40]. Both issues can be fully resolved by formulating a water-based lacquer solution or at least reduced using a solution based on ether as a solvent. In any case, producing the system beyond lab-scale demands reformulating the lacquer in accordance with the constrains of any suitable roll-to-roll wet coating technology.

Besides optimizing the lacquer for roll-to-roll wet coating, one must also ensure proper adhesion of the lacquer to the aluminum interface for an application in OVDs as reported in Section 3.6.1. In that section, I reported also possible means to improve adhesion like plasma treatment prior to wet coating. Applying the system on a substrate through hot stamping also needs a further foil process, coating of a hot-melt adhesive [129,195]. The coated dye lacquer can potentially diffuse to this adhesive as observed on lab-scale for encapsulation with cold glue in initial experiments. This would

be detrimental as the dye must be located in proximity of the grating surface to explore the strong near-field enhancement. This diffusion issue was resolved by coating the dye lacquer with a diffusion barrier of MgF_2 prior to encapsulation, but is probably also solvable with the right combination of dye lacquer and hot-melt adhesive.

4.8.2 Possible industrial applications

The application of the system to OVDs is again driven by my personal expertise of more than ten years in this field. The application there is very appealing as it provides a mean for protection of authenticity with strong and vivid colors that can be judged visually. The lithographic combination of mirror and (different) grating elements overcoated with a homogenous applied dye lacquer enables color generation/printing with sub-micron resolution due to locally different enhancement of the dye's absorption. Industrial applications of the reported system are certainly not limited to this very specialized field and can also find their way in the following fields:

- Visual sensing like the pregnancy test
- PH detectors for sweat detection on wearable clothes for sportsmen
- Enhancing the visibility of chromatography test (gel electrophoresis)
- Lab on chip for low concentration absorbing substances
- Reduce dependency on dispensing accuracy for substances by only structuring and/or metallizing sensing areas
- Biological sensing with absorbing markers instead of fluorescence ones
- Sensing areas in microreactors in combination with fluidics to create thin absorbing films on the corrugation
- Improve efficiency of dye-sensitized solar cells for energy harvesting
- Time-temperature indicator for perishable products by tracking diffusion-depending color changes
- Pixel colorization method for passive color displays
- Partially metallized structured glasses for strong color impression in reflection and neglectable in transmission
- Fast gas sensors thanks to the very short diffusion times in the thin (<100 nm) absorbing lacquer
- Enhanced light generation by replacing the absorbing lacquers with a fluorescent one
- High-density (multi bit) data storage based on colorized pixels

This list is certainly not comprehensive, but highlights that many applications can benefit from the interaction of a corrugation with minute amounts of an absorbing substance, especially in the fields of sensing.

Chapter 5 Conclusion

In this thesis, three different absorbing systems were investigated using numerical simulations and experiments. The underlying resonant absorption mechanisms were revealed and the most important system parameters for optimum absorption were identified. Depending on the system at hand, the dominating absorption mechanism was very different, ranging from plasmonic inter-particle coupling to interference, and finally, the interaction of multiple diffraction orders. All three researched systems have in common that they benefit from high absorption and may find industrial applications as was outlined at the end of the individual chapters and in Section 5.2 below.

5.1 Main results

The first system was realized experimentally by Hedayati et al. through three successive evaporation and co-evaporation steps of SiO_2 and gold [56]. On one hand the resulting three-layer MIM system clearly demonstrated near perfect absorption across the entire VIS. On the other hand, the originally hypothesized mechanisms leading to this exceptionally high and broadband absorption were at least debatable. I have shown here that the absorption is caused mainly by two coupled mechanisms. Firstly, the partially overlapping gold nanoparticles in the top nano-composite layer coupled with each other, enhancing and broadening absorption strongly compared to individual particles or well separated particles in the same configuration. Key for this strong resonant absorption just beneath the particles surface were small gaps between particles and their partial overlapping within the nano-composite layer. Secondly, the nano-composite layer was placed at an optimum distance from the bottom mirror layer by a dielectric spacer layer, forming a lossy Fabry-Perot cavity. Most light was absorbed within the top nano-composite layer at this distance. It was thus demonstrated that replacing the partially absorbing gold mirror with a highly reflecting aluminum mirror surprisingly enhanced absorption, leading up to a four times stronger absorption in the top layer compared to free standing particles through the interaction of the nano-composite layer with the reflecting mirror. It was further demonstrated that the systems absorption strength and band can be tuned by varying mirror distance, particle shape, spacing, metal type, and dielectric environment, revealing the versatility of the system. Envisioned applications mentioned in the original work were absorbers and/or anti-reflection coatings as the involved evaporation processes are micro-electro-mechanical systems (MEMS) compatible and thus quite cost effective [56]. Further applications such as heat management and thermal solar cells are envisioned in Section 2.5.2 and it is outlined that the system is also somewhat compatible with modern roll-to-roll foil production, albeit with some risks associated with co-evaporation of electrically conducting and insulating materials.

This major obstacle from a mass production viewpoint was resolved in Chapter 3 by replacing the top nano-composite layer with a chromium one for the second system. This simplified MIM system was realized experimentally by successive evaporation of three homogenous material layers: aluminum, magnesium fluorite, and chromium. It was shown by optimization of the dielectric spacer and chromium layer thickness in simulations and experiments that it also possible to achieve near perfect absorption with this simpler system that also improves the reproducibility of the results. Analysis of the simulation results revealed that also for this MIM system, most light is absorbed in the top chromium layer and this inspired the idea that the initially black appearance could be locally modified with a focused nanosecond laser. The appearance was switched from black to metallic by melting the top chromium layer and by further increasing the pulse power to transparent by melting both metal layers within the focal spot. Surprisingly, the laser processing window was most influenced by the choice of substrate material and mirror layer thickness, two parameters that do not alter the initial black appearance at all. These findings were applied to realize a colorful 3D art print consisting of black, reflective and transparent microscopic elements. The possibility to alter the optical parameters microscopically opens further

applications of this modified system compared to the original one discussed in Chapter 2, including personalized product labels and diffractive optical elements. It was outlined that the system is fully mass production compatible and in fact, more than 1000 m^2 of foil have been produced meanwhile on roll-to-roll basis with an industrial partner as outlined in Section 5.2.

Contrary to the first two systems, the third system was not based on flat, but corrugated surfaces and only part of the VIS was strongly absorbed, resulting in a colorful appearance of the system instead of black. The corrugation was realized in the form of a metal crossed grating and it was shown experimentally that the gratings self-color strongly depends on the metal type, grating profile, and dielectric environment. This was also confirmed by simulations, which also validated the self-colors strong dependency on the profile shape and further revealed the modest influence of the grating height. Inspired by works on fluorescence enhancement, thin absorbing dye lacquers were coated conformally on these crossed gratings. The interaction between the two enhanced the absorption of the thin dye lacquer locally by more than a factor of 20, rendering otherwise almost colorless dye lacquers a vivid colorful appearance. The strong enhancement of the dye lacquers intrinsic absorption was attributed to local field enhancement caused by evanescent and grazing propagating diffraction orders. Simulations revealed that in combination with artificial dye lacquers, a huge color gamut can be realized compared to applying the same lacquers on flat surfaces. The color gamut was initially centered around the grating's orange self-color and not around the white point, which limited the accessible region of the color gamut. Simulations demonstrated that shorter pitched gratings have near uniform reflection and thus no self-color, centering the color gamut around the white point to strongly enhance dye absorption of any color. The possibility to strongly enhance the visibility of almost colorless, but absorbing substances paves the way for applications in visual sensing like the pregnancy test and other possible applications, including PH detection and fast gas sensors, which are listed in Section 4.8.2. The grating system is fully mass production compatible and can be realized with modern roll-to-roll foil processes as outlined in Section 4.8.1.

In summary, three different systems were optimized for absorption. Each system exploits very different absorption mechanisms, but all are in principle compatible with modern roll-to-roll foil production as outlined at the end of the corresponding chapters. This diversity of physical mechanisms poses a challenge, as each system requires a different approach for its analysis and optimization; on the other hand, this multiplicity brings an advantage as one can select the best system for a specific application. In the next section, I provide an outlook how each of these systems can be adapted for a selected application to demonstrate the potentially broad impact of engineering absorption. These applications range from photocatalytic ammonia production to personalized authenticity protection and, finally, visual sensing.

5.2 Outlook

One may wonder why it is so important to develop absorbing systems that can be produced by modern roll-to-roll foil production? There is an economical point of view as this lowers the potential cost of any realized system compared to batch processes or any other low throughput method. On one hand, this is certainly an advantage when it comes to selling a product. On the other hand, low cost makes technology available to the largest set of potential customers, which is an even greater advantage in my opinion as this makes the outcome of research available to the general public. Besides cost, success of an industrial realization is also influenced by the relevance to and scalability of the target market as roll-to-roll foil production is only cost effective for rather large quantities exceeding 10,000 m^2. In the following, I will discuss one possible large-scale application for each of the three systems investigated in this thesis.

The first absorption system could maybe find a very original application in heterogeneous catalysis, especially plasmon-enhanced ammonia production, a very large market as the global production exceeds 200 million tons per year [196]. One may wonder how an optical phenomenon such as absorption can be used for ammonia production? It was shown for the systems in Chapter 2 that inter-particle coupling of the gold particles in combination with the cavity system leads to strong absorption within the top layer and generates strong near fields at the particles edges. Thangamuthu et al. showed that both factors are key for hot electron generation with a periodic system [197]. They also demonstrated that

this in turn can be used for efficient photocatalytic ammonia production by exploiting plasmonic absorption effects. Contrary to conventional methods, which require high pressure and temperature, the process can be carried out at room temperature under atmospheric pressure. They used periodically arranged aluminum nano triangles covered with a 100 nm thick titanium dioxide (TiO_2) layer for their experiments. This configuration achieved a quantum efficiency for ammonia generation of about 0.06% with about 5% surface coverage of the triangles and less than 50% total absorption for the used UV light.

The system described in Chapter 2 probably has the potential to improve each of these factors. The nano-composite layer covers 71% of the surface, absorbs more than 90% of the light in the VIS. Furthermore, the gold particles can be directly exposed to the 0.1 M KNO3 (pH ≈ 6) electrolyte used in [197], avoiding possible diffusion limitations through the TiO_2 layer. All three factors combined could thus lead to quantum efficiencies on the order of a few percent for photocatalytic ammonia production at room temperature and atmospheric pressure.

Initial experiments were performed by modifying the system described in Chapter 2 as schematically illustrated in Figure 5-1(a). The system is fabricated on lab-scale by evaporating on a glass substrate successively a 200 nm thick tungsten mirror layer, a 50 nm thick TiO_2 spacer layer and a 4 nm thick gold layer. Compared to the system in Chapter 2, the SiO_2 layer is replaced with a thinner TiO_2 layer of 50 nm (TiO_2 has a higher refractive index), keeping the cavity's optical path length constant. The whole system is then annealed for 2 hours at 500°C in an oven under nitrogen atmosphere to form anatase TiO_2 and simultaneously reflow the gold layer. This leads to the formation of gold nanoparticles with mean diameters of about 50 nm, see Figure 5-1(b). The nanoparticles are not anymore embedded in SiO_2 as in Chapter 2, they are placed directly on TiO_2 to allow direct interaction with the electrolyte as schematically visualized in Figure 5-1(a).

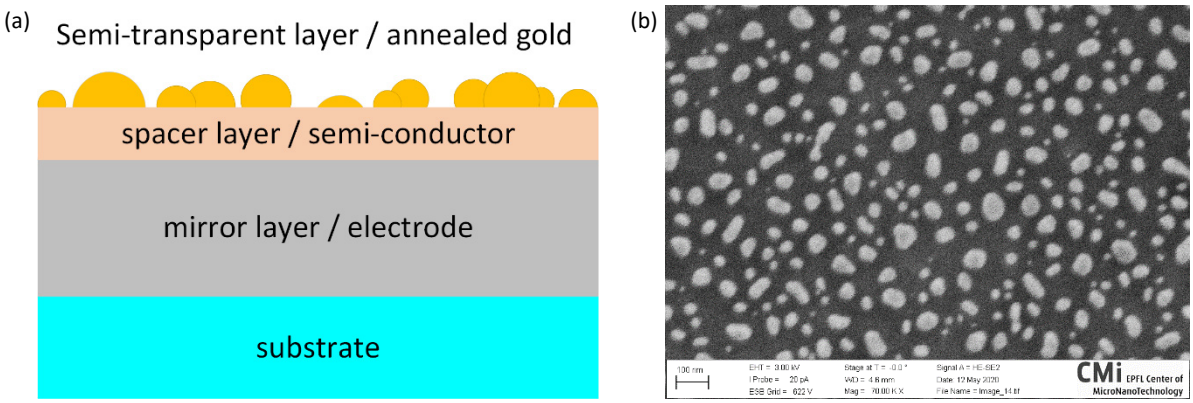

Figure 5-1. Modified MIM system for photocatalytic ammonia production. (a) Sketch of the system and (b) SEM image showing a representative size distribution of the annealed gold nanoparticle layer.

Despite tungsten's high melting point, it also reacted with the nitrogen atmosphere as was revealed by ellipsometry (data not shown). The measured permittivity of tungsten before and after annealing indicated a transition from metallic to dielectric behavior and very likely tungsten nitride was formed during annealing. The system thus became less absorbing and efficient ammonia production could not yet be shown with this modified system. Further research is needed to decide whether this approach justifies upscaling the application with roll-to-roll foil production for large quantity ammonia production.

Replacing the nano-composite layer with a homogenous chromium layer makes the second system easier to fabricate on industrial scale while still achieving near perfect absorption across the entire VIS. However, this also removes the strong local field enhancement found in the percolated layer, which rules out the system for ammonia production [197]. It can still be applied to document authenticity protection as outlined in Section 3.6.1. The ease of fabrication was demonstrated meanwhile with an industrial partner and more than 1000 m^2 of foil have been produced. In that case, the MIM system was fabricated in reversed order compared to the results in Chapter 3. First, the chromium layer was evaporated on a transfer foil with PET carrier, secondly the dielectric spacer layer and, finally, the aluminum mirror layer

was coated. On top of the aluminum layer a cold glue was applied to transfer the stack on a substrate by hot stamping [129,195]. The MIM system was consequently applied on white polyvinyl chloride (PVC) cards to demonstrate its application in protecting authenticity, see Figure 4-5.

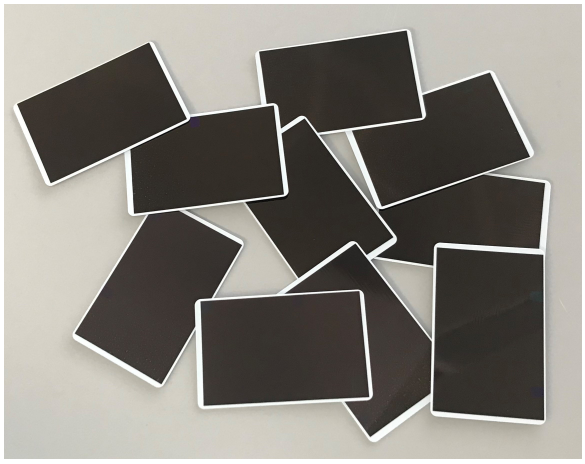

Figure 5-2. Photograph of the mass produced MIM system applied on white PVC cards.

The MIM system could be part of an integrated OVD solution, where for example an area of the applied transfer foil contains diffractive security elements and another area the black appearing MIM system that can be laser personalized. This integrated solution can reduce the total costs for customers by replacing laser engravable and cost intensive poly carbonate (PC) cards often used today [40], while also increasing security as the integrated solution with other security features will only be available from dedicated suppliers. The possibility to include black and metallic personalized areas further increases the level of security as one can prevent alteration of the personalized data with suitable laser personalization strategies. Contrary to the commonly used laser engravable PC card solution, information cannot be added, but only erased. Demonstrating the integrated solution will be the next step for the successful industrialization of the second system.

Contrary to the strong and broadband absorption of both previous systems, the third system absorbs rather narrowband to generate vivid colors. In cooperation with the same industrial partner, it was demonstrated that this system is at least partially already mass producible. In total more than 2000 m^2 of foil have been produced, where different crossed gratings with sub-wavelength periods were replicated in a suitable layer of a transfer foil and coated with a 20 nm thin aluminum layer. The system viewed through the PET carrier, see Figure 4-15(a), resembles the investigated ones in Chapter 4. Clearly visible are the gratings self-colors in Figure 4-15(a) that become significantly more vivid when spincoated with a 50 nm red dye lacquer, see Figure 4-15(b). One of the gratings even switches the color tone from yellow to wine red, compare the left parts of both pictures. This drastic color change certainly eases the implementation for any of the many application for visual sensing outlined in Section 4.8.2.

(a) (b)

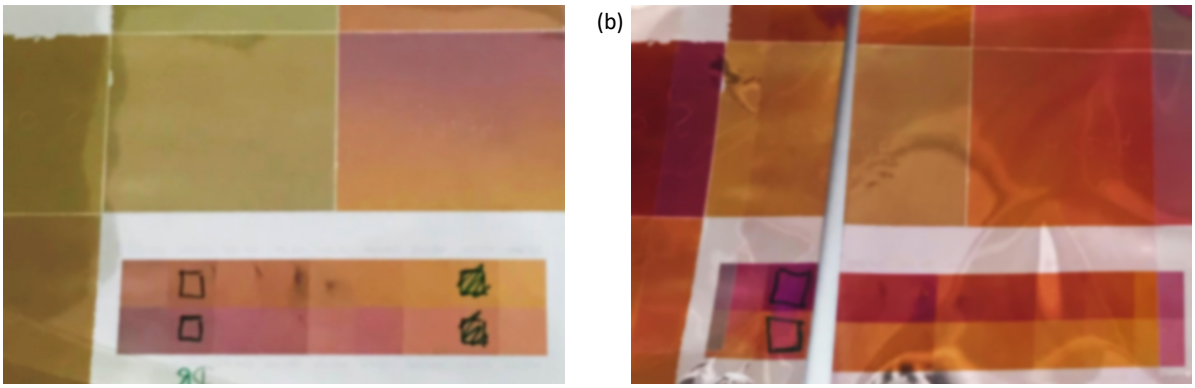

Figure 5-3. Photographs of different sub-wavelength crossed gratings manufactured by roll-to-roll foil production. (a) Photograph of the dielectric embedded gratings with $n \approx 1.5$ and (b) covered with a spincoated 50 nm thick red dye lacquer.

In Figure 4-15(b) one can also appreciate the huge color difference between flat mirror areas and corrugated surfaces. Flat mirror areas (white areas) are located at the top left corner and in the surrounding of the array of smaller test squares with varying crossed gratings. In cooperation with the industrial partner it is envisioned to create a prototype for visual pH-detection. Visual pH detection is not novel as it is a common method for pH detection; however, the observed vivid colors may make visual judging easier. In any case, the intention of the prototype is to find industrial partners with the required knowledge in biology and chemistry to bring this concept to life for visual sensing [185].

In summary, a possible industrial application was demonstrated for each of the three researched systems. They could all be industrialized with modern roll-to-roll foil production, which enables cost effective production of these systems for quantities exceeding 10,000 m^2.

List of abbreviations

3D	three-dimensional
AFM	atomic force microscopy
FDTD	finite difference time domain
HC	high concentration
LSP	localized surface plasmon
MC	medium concentration
MEMS	micro-electro-mechanical systems
MIM	metal insulator metal
OVD	optically variable device
PC	poly carbonate
PET	polyethylene terephthalate
PMMA	polymethyl methacrylate
PVC	polyvinyl chloride
SEM	scanning electron microscope
SPP	surface plasmon polariton
UV	ultra-violet
VIS	visible spectrum

List of figures

List of tables

References

1. C. F. Bohren and D. R. Huffman, *Absorption and Scattering of Light by Small Particles* (Wiley-VCH Verlag GmbH, 1998).
2. B. E. A. Saleh and M. C. Teich, *Fundamentals of Photonics*, 2. Edition (Wiley-Interscience, 2007).
3. S. Maier, *Plasmonics: Fundamentals and Applications* (Springer US, 2007).
4. M. K. Hedayati, M. Javaherirahim, B. Mozooni, R. Abdelaziz, A. Tavassolizadeh, V. S. K. Chakravadhanula, V. Zaporojtchenko, T. Strunkus, F. Faupel, and M. Elbahri, "Design of a Perfect Black Absorber at Visible Frequencies Using Plasmonic Metamaterials," Advanced Materials **23**(45), 5410–5414 (2011).
5. Y. Sun and Y. Xia, "Gold and silver nanoparticles: A class of chromophores with colors tunable in the range from 400 to 750 nm," Analyst **128**(6), 686–691 (2003).
6. H. Raether, *Surface Plasmons on Smooth and Rough Surfaces and on Gratings*, Springer Tracts in Modern Physics (Springer-Verlag, 1988).
7. Philip Laven MiePlot v4.6.09, "www.philiplaven.com/mieplot.htm," (2017).
8. K. L. Kelly, E. Coronado, L. L. Zhao, and G. C. Schatz, "The Optical Properties of Metal Nanoparticles: The Influence of Size, Shape, and Dielectric Environment," J. Phys. Chem. B **107**(3), 668–677 (2003).
9. J. P. Kottmann, O. J. F. Martin, D. R. Smith, and S. Schultz, "Plasmon resonances of silver nanowires with a nonregular cross section," Phys. Rev. B **64**(23), 235402 (2001).
10. A. Unger and M. Kreiter, "Analyzing the Performance of Plasmonic Resonators for Dielectric Sensing," J. Phys. Chem. C **113**(28), 12243–12251 (2009).
11. W. Zhang and O. J. F. Martin, "A universal law for plasmon resonance shift in biosensing," ACS Photonics **2**(1), 144–150 (2015).
12. P. Nagpal, N. C. Lindquist, S.-H. Oh, and D. J. Norris, "Ultrasmooth Patterned Metals for Plasmonics and Metamaterials," Science **325**(5940), 594–597 (2009).
13. K. M. McPeak, S. V. Jayanti, S. J. P. Kress, S. Meyer, S. Iotti, A. Rossinelli, and D. J. Norris, "Plasmonic Films Can Easily Be Better: Rules and Recipes," ACS Photonics **2**(3), 326–333 (2015).
14. S. Mader and O. J. F. Martin, "Mechanisms of perfect absorption in nano-composite systems," Opt. Express **26**(21), 27089–27100 (2018).
15. J. J. Mock, D. R. Smith, and S. Schultz, "Local Refractive Index Dependence of Plasmon Resonance Spectra from Individual Nanoparticles," Nano Lett. **3**(4), 485–491 (2003).
16. J. P. Kottmann, O. J. F. Martin, D. R. Smith, and S. Schultz, "Spectral response of plasmon resonant nanoparticles with a non-regular shape," Opt. Express **6**(11), 213–219 (2000).
17. J. J. Mock, M. Barbic, D. R. Smith, D. A. Schultz, and S. Schultz, "Shape effects in plasmon resonance of individual colloidal silver nanoparticles," J. Chem. Phys. **116**(15), 6755–6759 (2002).
18. U. Zywietz, A. B. Evlyukhin, C. Reinhardt, and B. N. Chichkov, "Laser printing of silicon nanoparticles with resonant optical electric and magnetic responses," Nat. Commun. **5**(1), 1–7 (2014).
19. X. Zhu, C. Vannahme, E. Højlund-Nielsen, N. A. Mortensen, and A. Kristensen, "Plasmonic colour laser printing," Nature Nanotechnology **11**(4), 325–329 (2016).
20. H. Oh, J. Lee, M. Seo, I. U. Baek, J. Y. Byun, and M. Lee, "Laser-Induced Dewetting of Metal Thin Films for Template-Free Plasmonic Color Printing," ACS Appl. Mater. Interfaces **10**(44), 38368–38375 (2018).
21. P. Nyga, S. N. Chowdhury, Z. Kudyshev, M. D. Thoreson, A. V. Kildishev, V. M. Shalaev, and A. Boltasseva, "Laser-induced color printing on semicontinuous silver films: red, green and blue," Opt. Mater. Express **9**(3), 1528–1538 (2019).

22. F. Pallottino, L. Hakola, C. Costa, F. Antonucci, S. Figorilli, A. Seisto, and P. Menesatti, "Printing on Food or Food Printing: a Review," Food Bioprocess Technol **9**(5), 725–733 (2016).

23. J. S. Clausen, E. Højlund-Nielsen, A. B. Christiansen, S. Yazdi, M. Grajower, H. Taha, U. Levy, A. Kristensen, and N. A. Mortensen, "Plasmonic Metasurfaces for Coloration of Plastic Consumer Products," Nano Lett. **14**(8), 4499–4504 (2014).

24. W. Rechberger, A. Hohenau, A. Leitner, J. R. Krenn, B. Lamprecht, and F. R. Aussenegg, "Optical properties of two interacting gold nanoparticles," Opt. Commun. **220**(1), 137–141 (2003).

25. T. Atay, J.-H. Song, and A. V. Nurmikko, "Strongly interacting plasmon nanoparticle pairs: from dipole−dipole interaction to conductively coupled regime," Nano Lett. **4**(9), 1627–1631 (2004).

26. P. Nordlander, C. Oubre, E. Prodan, K. Li, and M. I. Stockman, "Plasmon Hybridization in Nanoparticle Dimers," Nano Lett. **4**(5), 899–903 (2004).

27. R. Ameling and H. Giessen, "Cavity Plasmonics: Large Normal Mode Splitting of Electric and Magnetic Particle Plasmons Induced by a Photonic Microcavity," Nano Lett. **10**(11), 4394–4398 (2010).

28. R. Ameling and H. Giessen, "Microcavity plasmonics: strong coupling of photonic cavities and plasmons," Laser & Photonics Rev. **7**(2), 141–169 (2013).

29. J. R. Krenn, A. Dereux, J. C. Weeber, E. Bourillot, Y. Lacroute, J. P. Goudonnet, G. Schider, W. Gotschy, A. Leitner, F. R. Aussenegg, and C. Girard, "Squeezing the Optical Near-Field Zone by Plasmon Coupling of Metallic Nanoparticles," Phys. Rev. Lett. **82**(12), 2590–2593 (1999).

30. S. A. Maier, M. L. Brongersma, P. G. Kik, and H. A. Atwater, "Observation of near-field coupling in metal nanoparticle chains using far-field polarization spectroscopy," Phys. Rev. B **65**(19), 193408 (2002).

31. D. Brunazzo, E. Descrovi, and O. J. F. Martin, "Narrowband optical interactions in a plasmonic nanoparticle chain coupled to a metallic film," Opt. Lett. **34**(9), 1405–1407 (2009).

32. A. Christ, G. Lévêque, O. J. F. Martin, T. Zentgraf, J. Kuhl, C. Bauer, H. Giessen, and S. G. Tikhodeev, "Near-field–induced tunability of surface plasmon polaritons in composite metallic nanostructures," J. Microsc. **229**(2), 344–353 (2008).

33. G. Lévêque and O. J. F. Martin, "Optical interactions in a plasmonic particle coupled to a metallic film," Opt. Express **14**(21), 9971–9981 (2006).

34. S. D. Rezaei, J. Ho, R. J. H. Ng, S. Ramakrishna, and J. K. W. Yang, "On the correlation of absorption cross-section with plasmonic color generation," Opt. Express **25**(22), 27652–27664 (2017).

35. A. Kristensen, J. K. W. Yang, S. I. Bozhevolnyi, S. Link, P. Nordlander, N. J. Halas, and N. A. Mortensen, "Plasmonic colour generation," Nat. Rev. Mater. **2**, 16088 (2016).

36. M. Song, D. Wang, S. Peana, S. Choudhury, P. Nyga, Z. A. Kudyshev, H. Yu, A. Boltasseva, V. M. Shalaev, and A. V. Kildishev, "Colors with plasmonic nanostructures: A full-spectrum review," Appl. Physics Reviews **6**(4), 041308 (2019).

37. Z. Xuan, J. Li, Q. Liu, F. Yi, S. Wang, and W. Lu, "Artificial Structural Colors and Applications," Innovation **2**(1), (2021).

38. A. I. Kuznetsov, A. B. Evlyukhin, M. R. Gonçalves, C. Reinhardt, A. Koroleva, M. L. Arnedillo, R. Kiyan, O. Marti, and B. N. Chichkov, "Laser Fabrication of Large-Scale Nanoparticle Arrays for Sensing Applications," ACS Nano **5**(6), 4843–4849 (2011).

39. S. V. Makarov, V. A. Milichko, I. S. Mukhin, I. I. Shishkin, D. A. Zuev, A. M. Mozharov, A. E. Krasnok, and P. A. Belov, "Controllable femtosecond laser-induced dewetting for plasmonic applications," Laser & Photonics Rev. **10**(1), 91–99 (2016).

40. R. L. Renesse, *Optical Document Security*, 3rd ed., Artech House Optoelectronics Library (Artech House, 2005).

41. T. D. James, P. Mulvaney, and A. Roberts, "The Plasmonic Pixel: Large Area, Wide Gamut Color Reproduction Using Aluminum Nanostructures," Nano Lett. **16**(6), 3817–3823 (2016).

42. I. Koirala, V. R. Shrestha, C.-S. Park, S.-S. Lee, and D.-Y. Choi, "Polarization-Controlled Broad Color Palette Based on an Ultrathin One-Dimensional Resonant Grating Structure," Sci. Rep. **7**, 40073 (2017).

43. S. Wu Sr., Y. Ye, and L. Chen, "Polarization-dependent reflective colors incorporating meta-gratings with an asymmetric profile," in *Plasmonics III* (International Society for Optics and Photonics, 2018), **10824**, p. 1082418.

44. A. S. Roberts, S. M. Novikov, Y. Yang, Y. Chen, S. Boroviks, J. Beermann, N. A. Mortensen, and S. I. Bozhevolnyi, "Laser Writing of Bright Colors on Near-Percolation Plasmonic Reflector Arrays," ACS Nano **13**(1), 71–77 (2019).

45. Z. Li, E. Palacios, S. Butun, H. Kocer, and K. Aydin, "Omnidirectional, broadband light absorption using large-area, ultrathin lossy metallic film coatings," Sci. Rep. **5**(1), 15137 (2015).

46. H. A. Atwater and A. Polman, "Plasmonics for improved photovoltaic devices," Nat. Mater. **9**(3), 205–213 (2010).

47. K. Aydin, V. E. Ferry, R. M. Briggs, and H. A. Atwater, "Broadband polarization-independent resonant light absorption using ultrathin plasmonic super absorbers," Nat. Commun. **2**(1), 517 (2011).

48. F. Ding, J. Dai, Y. Chen, J. Zhu, Y. Jin, and S. I. Bozhevolnyi, "Broadband near-infrared metamaterial absorbers utilizing highly lossy metals," Sci. Rep. **6**(1), 39445 (2016).

49. J. Cesario, R. Quidant, G. Badenes, and S. Enoch, "Electromagnetic coupling between a metal nanoparticle grating and a metallic surface," Opt. Lett. **30**(24), 3404–3406 (2005).

50. Q. Chen, J. Gu, P. Liu, J. Xie, J. Wang, Y. Liu, and W. Zhu, "Nanowire-based ultra-wideband absorber for visible and ultraviolet light," Opt. Laser Technol. **105**, 102–105 (2018).

51. T. V. Teperik, V. V. Popov, and F. J. García de Abajo, "Void plasmons and total absorption of light in nanoporous metallic films," Phys. Rev. B **71**(8), 085408 (2005).

52. N. Liu, M. Mesch, T. Weiss, M. Hentschel, and H. Giessen, "Infrared perfect absorber and its application as plasmonic sensor," Nano Lett. **10**(7), 2342–2348 (2010).

53. J. A. Bossard, L. Lin, S. Yun, L. Liu, D. H. Werner, and T. S. Mayer, "Near-ideal optical metamaterial absorbers with super-octave bandwidth," ACS Nano **8**(2), 1517–1524 (2014).

54. H. Takele, H. Greve, C. Pochstein, V. Zaporojtchenko, and F. Faupel, "Plasmonic properties of Ag nanoclusters in various polymer matrices," Nanotechnology **17**(14), 3499–3505 (2006).

55. V. G. Kravets, S. Neubeck, A. N. Grigorenko, and A. F. Kravets, "Plasmonic blackbody: Strong absorption of light by metal nanoparticles embedded in a dielectric matrix," Phys. Rev. B **81**(16), 165401 (2010).

56. M. K. Hedayati, M. Javaherirahim, B. Mozooni, R. Abdelaziz, A. Tavassolizadeh, V. S. K. Chakravadhanula, V. Zaporojtchenko, T. Strunkus, F. Faupel, and M. Elbahri, "Design of a perfect black absorber at visible frequencies using plasmonic metamaterials," Adv. Mater. **23**(45), 5410–5414 (2011).

57. J. Y. Lu, A. Raza, S. Noorulla, A. S. Alketbi, N. X. Fang, G. Chen, and T. Zhang, "Near-perfect ultrathin nanocomposite absorber with self-formed topping plasmonic nanoparticles," Adv. Opt. Mater. **5**(18), 1700222 (2017).

58. J. W. Stewart, G. M. Akselrod, D. R. Smith, and M. H. Mikkelsen, "Toward Multispectral Imaging with Colloidal Metasurface Pixels," Adv. Mater. **29**(6), 1602971 (2017).

59. C. Etrich, S. Fahr, M. Hedayati, F. Faupel, M. Elbahri, and C. Rockstuhl, "Effective optical properties of plasmonic nanocomposites," Materials **7**(2), 727–741 (2014).

60. W. Zhu, F. Xiao, I. D. Rukhlenko, J. Geng, X. Liang, M. Premaratne, and R. Jin, "Wideband visible-light absorption in an ultrathin silicon nanostructure," Opt. Express **25**(5), 5781–5786 (2017).

61. T. V. Teperik, F. J. G. de Abajo, A. G. Borisov, M. Abdelsalam, P. N. Bartlett, Y. Sugawara, and J. J. Baumberg, "Omnidirectional absorption in nanostructured metal surfaces," Nature Photonics **2**(5), 299–301 (2008).

62. J. Hao, J. Wang, X. Liu, W. J. Padilla, L. Zhou, and M. Qiu, "High performance optical absorber based on a plasmonic metamaterial," Appl. Phys. Lett. **96**(25), 251104 (2010).

63. H. Deng, Z. Li, L. Stan, D. Rosenmann, D. Czaplewski, J. Gao, and X. Yang, "Broadband perfect absorber based on one ultrathin layer of refractory metal," Opt. Lett. **40**(11), 2592–2595 (2015).

64. F. Ding, L. Mo, J. Zhu, and S. He, "Lithography-free, broadband, omnidirectional, and polarization-insensitive thin optical absorber," Appl. Phys. Lett. **106**(6), 061108 (2015).

65. M. Chirumamilla, A. S. Roberts, F. Ding, D. Wang, P. K. Kristensen, S. I. Bozhevolnyi, and K. Pedersen, "Multilayer tungsten-alumina-based broadband light absorbers for high-temperature applications," Opt. Mater. Express **6**(8), 2704–2714 (2016).

66. P. Feng, W.-D. Li, and W. Zhang, "Dispersion engineering of plasmonic nanocomposite for ultrathin broadband optical absorber," Opt. Express **23**(3), 2328–2338 (2015).

67. P. Mao, C. Liu, F. Song, M. Han, S. A. Maier, and S. Zhang, "Manipulating disordered plasmonic systems by external cavity with transition from broadband absorption to reconfigurable reflection," Nat. Commun. **11**(1), 1538 (2020).

68. J. Le Perchec, P. Quémerais, A. Barbara, and T. López-Ríos, "Why Metallic Surfaces with Grooves a Few Nanometers Deep and Wide May Strongly Absorb Visible Light," Phys. Rev. Lett. **100**(6), 066408 (2008).

69. T. Søndergaard, S. M. Novikov, T. Holmgaard, R. L. Eriksen, J. Beermann, Z. Han, K. Pedersen, and Sergey I. Bozhevolnyi, "Plasmonic black gold by adiabatic nanofocusing and absorption of light in ultra-sharp convex grooves," Nat. Commun. **3**, 969 (2012).

70. M. Toma, G. Loget, and R. M. Corn, "Fabrication of Broadband Antireflective Plasmonic Gold Nanocone Arrays on Flexible Polymer Films," Nano Lett. **13**(12), 6164–6169 (2013).

71. A. B. Christiansen, G. P. Caringal, J. S. Clausen, M. Grajower, H. Taha, U. Levy, N. Asger Mortensen, and A. Kristensen, "Black metal thin films by deposition on dielectric antireflective moth-eye nanostructures," Sci. Rep. **5**, 10563 (2015).

72. M. Hedayati, F. Faupel, and M. Elbahri, "Review of plasmonic nanocomposite metamaterial absorber," Materials **7**(2), 1221–1248 (2014).

73. A. Leitner, Z. Zhao, H. Brunner, F. R. Aussenegg, and A. Wokaun, "Optical properties of a metal island film close to a smooth metal surface," Appl. Opt. **32**(1), 102–110 (1993).

74. U. K. Chettiar, P. Nyga, M. D. Thoreson, A. V. Kildishev, V. P. Drachev, and V. M. Shalaev, "FDTD modeling of realistic semicontinuous metal films," Appl. Phys. B **100**(1), 159–168 (2010).

75. T. Ji, L. Peng, Y. Zhu, F. Yang, Y. Cui, X. Wu, L. Liu, S. He, F. Zhu, and Y. Hao, "Plasmonic broadband absorber by stacking multiple metallic nanoparticle layers," Appl. Phys. Lett. **106**(16), 161107 (2015).

76. K. Seal, M. A. Nelson, Z. C. Ying, D. A. Genov, A. K. Sarychev, and V. M. Shalaev, "Growth, morphology, and optical and electrical properties of semicontinuous metallic films," Phys. Rev. B **67**(3), 035318 (2003).

77. W. R. Holland and D. G. Hall, "Frequency shifts of an electric-dipole resonance near a conducting surface," Phys. Rev. Lett. **52**(12), 1041–1044 (1984).

78. M. Yan, J. Dai, and M. Qiu, "Lithography-free broadband visible light absorber based on a mono-layer of gold nanoparticles," J. Opt. **16**(2), 025002 (2014).

79. R. Yu, P. Mazumder, N. F. Borrelli, A. Carrilero, D. S. Ghosh, R. A. Maniyara, D. Baker, F. J. García de Abajo, and V. Pruneri, "Structural coloring of glass using dewetted nanoparticles and ultrathin films of metals," ACS Photonics **3**(7), 1194–1201 (2016).

80. K. J. Berean, V. Sivan, I. Khodasevych, A. Boes, E. Della Gaspera, M. R. Field, K. Kalantar-Zadeh, A. Mitchell, and G. Rosengarten, "Laser-induced dewetting for precise local generation of Au nanostructures for tunable solar absorption," Adv. Opt. Mater. **4**(8), 1247–1254 (2016).

81. B. Choi, H.-H. Lee, S. Jin, S. Chun, and S.-H. Kim, "Characterization of the optical properties of silver nanoparticle films," Nanotechnology **18**(7), 075706 (2007).

82. S. Hewlett and A. Mock, "Engineering metamaterial absorbers from dense gold nanoparticle stacks," J. Appl. Phys. **122**(9), 093103 (2017).

83. Lumerical Inc. FDTD Solutions R2017a, "http://www.lumerical.com/tcad-products/fdtd/," (2020).

84. N. D. Lang and W. Kohn, "Theory of Metal Surfaces: Work Function," Phys. Rev. B **3**(4), 1215–1223 (1971).

85. J. Zuloaga, E. Prodan, and P. Nordlander, "Quantum Description of the Plasmon Resonances of a Nanoparticle Dimer," Nano Lett. **9**(2), 887–891 (2009).

86. C. Ciracì, R. T. Hill, J. J. Mock, Y. Urzhumov, A. I. Fernández-Domínguez, S. A. Maier, J. B. Pendry, A. Chilkoti, and D. R. Smith, "Probing the Ultimate Limits of Plasmonic Enhancement," Science **337**(6098), 1072–1074 (2012).

87. K. J. Savage, M. M. Hawkeye, R. Esteban, A. G. Borisov, J. Aizpurua, and J. J. Baumberg, "Revealing the quantum regime in tunnelling plasmonics," Nature **491**(7425), 574–577 (2012).

88. G. Toscano, J. Straubel, A. Kwiatkowski, C. Rockstuhl, F. Evers, H. Xu, N. Asger Mortensen, and M. Wubs, "Resonance shifts and spill-out effects in self-consistent hydrodynamic nanoplasmonics," Nat Commun **6**(1), 7132 (2015).

89. J. P. Kottmann and O. J. F. Martin, "Plasmon resonant coupling in metallic nanowires," Opt. Express **8**(12), 655–663 (2001).

90. H. Fischer and O. J. F. Martin, "Engineering the optical response of plasmonic nanoantennas," Opt. Express **16**(12), 9144–9154 (2008).

91. C. A. Downing and G. Weick, "Plasmonic modes in cylindrical nanoparticles and dimers," Proceedings of the Royal Society A: Mathematical, Physical and Engineering Sciences **476**(2244), 20200530 (2020).

92. K.-H. Su, Q.-H. Wei, X. Zhang, J. J. Mock, D. R. Smith, and S. Schultz, "Interparticle Coupling Effects on Plasmon Resonances of Nanogold Particles," Nano Lett. **3**(8), 1087–1090 (2003).

93. V. G. Kravets, A. V. Kabashin, W. L. Barnes, and A. N. Grigorenko, "Plasmonic Surface Lattice Resonances: A Review of Properties and Applications," Chem. Rev. **118**(12), 5912–5951 (2018).

94. P. Nordlander and E. Prodan, "Plasmon hybridization in nanoparticles near metallic surfaces," Nano Lett. **4**(11), 2209–2213 (2004).

95. A. Ghobadi, S. A. Dereshgi, H. Hajian, B. Bozok, B. Butun, and E. Ozbay, "Ultra-broadband, wide angle absorber utilizing metal insulator multilayers stack with a multi-thickness metal surface texture," Sci. Rep. **7**(1), 4755 (2017).

96. H.-C. Wang, C. H. Chu, P. C. Wu, H.-H. Hsiao, H. J. Wu, J.-W. Chen, W. H. Lee, Y.-C. Lai, Y.-W. Huang, M. L. Tseng, S.-W. Chang, and D. P. Tsai, "Ultrathin planar cavity metasurfaces," Small **14**(17), 1703920 (2018).

97. K. Thyagarajan, C. Santschi, P. Langlet, and O. J. F. Martin, "Highly improved fabrication of Ag and Al nanostructures for UV and nonlinear plasmonics," Adv. Opt. Mater. **4**(6), 871–876 (2016).

98. G. Baffou, R. Quidant, and C. Girard, "Thermoplasmonics modeling: A Green's function approach," Phys. Rev. B **82**(16), 165424 (2010).

99. Md. A. Badsha, Y. C. Jun, and C. K. Hwangbo, "Admittance matching analysis of perfect absorption in unpatterned thin films," Optics Communications **332**, 206–213 (2014).

100. H. A. MacLeod, *Thin-Film Optical Filters*, 5th ed. (Taylor & Francis Ltd, 2017).

101. J. C. M. Garnett, "Colours in Metal Glasses and in Metallic Films," Philosophical Transactions of the Royal Society A: Mathematical, Physical and Engineering Sciences **203**(359–371), 385–420 (1904).

102. D. a. G. Bruggeman, "Berechnung verschiedener physikalischer Konstanten von heterogenen Substanzen. I. Dielektrizitätskonstanten und Leitfähigkeiten der Mischkörper aus isotropen Substanzen," Annalen der Physik **416**(7), 636–664 (1935).

103. B. Abeles and J. I. Gittleman, "Composite material films: optical properties and applications," Appl. Opt., AO **15**(10), 2328–2332 (1976).

104. G. A. Niklasson, C. G. Granqvist, and O. Hunderi, "Effective medium models for the optical properties of inhomogeneous materials," Appl. Opt., AO **20**(1), 26–30 (1981).

105. P. B. Johnson and R. W. Christy, "Optical Constants of the Noble Metals," Phys. Rev. B **6**(12), 4370–4379 (1972).

106. S. Mader and O. J. F. Martin, "Engineering multi-state transparency on demand," Light: Adv. Manuf. **2**(4), 1–10 (2021).

107. W. Li and J. Valentine, "Metamaterial Perfect Absorber Based Hot Electron Photodetection," Nano Lett. **14**(6), 3510–3514 (2014).

108. K. Bae, G. Kang, S. K. Cho, W. Park, K. Kim, and W. J. Padilla, "Flexible thin-film black gold membranes with ultrabroadband plasmonic nanofocusing for efficient solar vapour generation," Nat. Commun. **6**(1), 1–9 (2015).

109. M. Yang, A. Gatto, and N. Kaiser, "Optical thin films with high reflectance, low thickness and low stress for the spectral range from vacuum UV to near IR," J. Opt. A: Pure Appl. Opt. **8**(3), 327–332 (2006).

110. N. Yu, P. Genevet, M. A. Kats, F. Aieta, J.-P. Tetienne, F. Capasso, and Z. Gaburro, "Light Propagation with Phase Discontinuities: Generalized Laws of Reflection and Refraction," Science **334**(6054), 333–337 (2011).

111. M. A. Kats, R. Blanchard, P. Genevet, and F. Capasso, "Nanometre optical coatings based on strong interference effects in highly absorbing media," Nat. Mater. **12**(1), 20–24 (2012).

112. A. M. Shaltout, J. Kim, A. Boltasseva, V. M. Shalaev, and A. V. Kildishev, "Ultrathin and multicolour optical cavities with embedded metasurfaces," Nat. Commun. **9**(1), 2673 (2018).

113. P. Hosseini, C. D. Wright, and H. Bhaskaran, "An optoelectronic framework enabled by low-dimensional phase-change films," Nature **511**(7508), 206–211 (2014).

114. D. Lin, P. Fan, E. Hasman, and M. L. Brongersma, "Dielectric gradient metasurface optical elements," Science **345**(6194), 298–302 (2014).

115. J. Heo, J.-W. Huh, and T.-H. Yoon, "Fast-switching initially-transparent liquid crystal light shutter with crossed patterned electrodes," AIP Adv. **5**(4), 047118 (2015).

116. M. Kim, K. J. Park, S. Seok, J. M. Ok, H.-T. Jung, J. Choe, and D. H. Kim, "Fabrication of Microcapsules for Dye-Doped Polymer-Dispersed Liquid Crystal-Based Smart Windows," ACS Appl. Mater. Interfaces **7**(32), 17904–17909 (2015).

117. A. I. Kuznetsov, A. E. Miroshnichenko, M. L. Brongersma, Y. S. Kivshar, and B. Luk'yanchuk, "Optically resonant dielectric nanostructures," Science **354**(6314), (2016).

118. M. L. Tseng, H.-H. Hsiao, C. H. Chu, M. K. Chen, G. Sun, A.-Q. Liu, and D. P. Tsai, "Metalenses: Advances and Applications," Adv. Opt. Mater. **6**(18), 1800554 (2018).

119. M. Wuttig and N. Yamada, "Phase-change materials for rewriteable data storage," Nat. Mater. **6**(11), 824–832 (2007).

120. M. Gu, Q. Zhang, and S. Lamon, "Nanomaterials for optical data storage," Nat. Rev. Mater. **1**(12), 1–14 (2016).

121. 2D-Barcode-Fibel 7th ed., https://barcodat.com/wordpress/wp-content/uploads/2017/08/Barcodat-2D-Code-Fibel_WEB.pdf, (2020).

122. Y. Md. Noor, S. C. Tam, L. E. N. Lim, and S. Jana, "A review of the Nd: YAG laser marking of plastic and ceramic IC packages," J. Mater. Process. Technol. **42**(1), 95–133 (1994).

123. F. Mao, A. Davis, Q. C. Tong, M. H. Luong, C. T. Nguyen, I. Ledoux-Rak, and N. D. Lai, "Direct Laser Writing of Gold Nanostructures: Application to Data Storage and Color Nanoprinting," Plasmonics **13**(6), 2285–2291 (2018).

124. J.-M. Guay, A. C. Lesina, G. Côté, M. Charron, D. Poitras, L. Ramunno, P. Berini, and A. Weck, "Laser-induced plasmonic colours on metals," Nat. Commun. **8**(1), 1–12 (2017).

125. G. V. Odintsova, E. A. Vlasova, Y. M. Andreeva, M. K. Moskvin, A. S. Krivonosov, E. V. Gorbunova, D. V. Pankin, O. S. Medvedev, M. M. Sergeev, N. N. Shchedrina, D. S. Lutoshina, and V. P. Veiko, "High-resolution large-scale plasmonic laser color printing for jewelry applications," Opt. Express **27**(3), 3672–3681 (2019).

126. A. D. Rakić, "Algorithm for the determination of intrinsic optical constants of metal films: application to aluminum," Appl. Opt. **34**(22), 4755–4767 (1995).

127. V. Lozanova, A. Lalova, L. Soserov, and R. Todorov, "Optical and electrical properties of very thin chromium films for optoelectronic devices," J. Phys.: Conf. Ser. **514**, 012003 (2014).

128. L. V. R. Marcos, J. I. Larruquert, J. A. Méndez, and J. A. Aznárez, "Self-consistent optical constants of MgF_2, LaF_3, and CeF_3 films," Opt. Mater. Express **7**(3), 989–1006 (2017).

129. J. Hielscher, D. Foik, A. Lyashenko, and R. Werthschützky, "P2.3 - Strain gauges made of laser patterned hot stamping foil," Proceedings SENSOR 2015 762–765 (2015).

130. E. D. Palik, *Handbook of Optical Constants of Solids*, 3rd ed. (Academic Press, 1998).

131. P. Feng, W.-D. Li, and W. Zhang, "Dispersion engineering of plasmonic nanocomposite for ultrathin broadband optical absorber," Opt. Express **23**(3), 2328–2338 (2015).

132. R. L. Renesse, "Interference-Based Security Features," in *Optical Document Security*, 3rd ed., Artech House Optoelectronics Library (Artech House, 2005), pp. 223–264.

133. G. R. Stoner, T. D. Albright, and V. S. Ramachandran, "Transparency and coherence in human motion perception," Nature **344**(6262), 153–155 (1990).

134. Y. Wu, J. D. Fowlkes, and P. D. Rack, "The optical properties of Cu-Ni nanoparticles produced via pulsed laser dewetting of ultrathin films: The effect of nanoparticle size and composition on the plasmon response," J. Mater. Res. **26**(2), 277–287 (2011).

135. Y. Oh and M. Lee, "Single-pulse transformation of Ag thin film into nanoparticles via laser-induced dewetting," Appl. Surf. Sci. **399**, 555–564 (2017).

136. F. Font, S. Afkhami, and L. Kondic, "Substrate melting during laser heating of nanoscale metal films," Int. J. Heat Mass Transf. **113**, 237–245 (2017).

137. C. M. A. Lopes and M. I. Felisberti, "Thermal conductivity of PET/(LDPE/AI) composites determined by MDSC," Polym. Test. **23**(6), 637–643 (2004).

138. D. Qi, D. Paeng, J. Yeo, E. Kim, L. Wang, S. Chen, and C. P. Grigoropoulos, "Time-resolved analysis of thickness-dependent dewetting and ablation of silver films upon nanosecond laser irradiation," Appl. Phys. Lett. **108**(21), (2016).

139. D01.23 Committee, *Test Methods for Rating Adhesion by Tape Test*, D3359-17 (ASTM International, 2017).

140. ISO/IEC JTC 1/SC 17, *Cards and Security Devices for Personal Identification — Test Methods — Part 1: General Characteristics*, ISO/IEC 10373-1:2020 (International Organization for Standardization, 2020).

141. ISO/IEC JTC 1/SC 17, *Identification Cards — Physical Characteristics*, ISO/IEC 7810:2019 (International Organization for Standardization, 2019).

142. S. Mader and O. J. F. Martin, "Remarkable Color Gamut Enhancement of Dye Lacquers Using Corrugated Surfaces," Adv. Phot. Res., 2100245 (2021).

143. S. Kinoshita, S. Yoshioka, and J. Miyazaki, "Physics of structural colors," Rep. Prog. Phys. **71**(7), 076401 (2008).

144. M. K. Hedayati and M. Elbahri, "Review of Metasurface Plasmonic Structural Color," Plasmonics **12**(5), 1463–1479 (2017).

145. W. A. Murray and W. L. Barnes, "Plasmonic Materials," Adv. Materials **19**(22), 3771–3782 (2007).

146. J. M. McMahon, G. C. Schatz, and S. K. Gray, "Plasmonics in the ultraviolet with the poor metals Al, Ga, In, Sn, Tl, Pb, and Bi," Phys. Chem. Chem. Phys. **15**(15), 5415–5423 (2013).

147. A. V. Zayats and I. I. Smolyaninov, "Near-field photonics: surface plasmon polaritons and localized surface plasmons," Journal of Optics A: Pure and Applied Optics **5**(4), S16–S50 (2003).

148. L. Novotny and B. Hecht, *Principles of Nano-Optics*, 2nd ed. (Cambridge University Press, 2012).

149. H.-S. Lee, Y.-T. Yoon, S.-S. Lee, S.-H. Kim, and K.-D. Lee, "Color filter based on a subwavelength patterned metal grating," Opt. Express **15**(23), 15457–15463 (2007).

150. Q. Chen and D. R. S. Cumming, "High transmission and low color cross-talk plasmonic color filters using triangular-lattice hole arrays in aluminum films," Opt. Express **18**(13), 14056–14062 (2010).

151. K. G. Sullivan, O. King, C. Sigg, and D. G. Hall, "Directional, enhanced fluorescence from molecules near a periodic surface," Appl. Opt. **33**(13), 2447–2454 (1994).

152. P. Andrew and W. L. Barnes, "Molecular fluorescence above metallic gratings," Phys. Rev. B **64**(12), 125405 (2001).

153. J. M. Lupton, B. J. Matterson, I. D. W. Samuel, M. J. Jory, and W. L. Barnes, "Bragg scattering from periodically microstructured light emitting diodes," Appl. Phys. Lett. **77**(21), 3340–3342 (2000).

154. A. Williamson, É. McClean, D. Leipold, D. Zerulla, and E. Runge, "The design of efficient surface-plasmon-enhanced ultra-thin polymer-based solar cells," Appl. Phys. Letters **99**(9), 093307 (2011).

155. W. Knoll, M. R. Philpott, J. D. Swalen, and A. Girlando, "Surface plasmon enhanced Raman spectra of monolayer assemblies," J. Chem. Phys. **77**(5), 2254–2260 (1982).

156. G. Ruffato, G. Zacco, and F. Romanato, "Innovative Exploitation of Grating-Coupled Surface Plasmon Resonance for Sensing," in *Plasmonics - Principles and Applications* (IntechOpen, 2012), pp. 419–444.

157. M. L. Schattenburg, E. H. Anderson, and H. I. Smith, "X-ray/VUV transmission gratings for astrophysical and laboratory applications," Phys. Scr. **41**(1), 13–20 (1990).

158. A. A. Ushkov, I. Verrier, T. Kampfe, and Y. Jourlin, "Subwavelength diffraction gratings with macroscopic moiré patterns generated via laser interference lithography," Opt. Express **28**(11), 16453–16468 (2020).

159. S. C. Kitson, W. L. Barnes, and J. R. Sambles, "The fabrication of submicron hexagonal arrays using multiple-exposure optical interferometry," IEEE Photonics Technol. Lett. **8**(12), 1662–1664 (1996).

160. B. Bläsi, "Holographisch hergestellte Antireflexoberflächen für solare und visuelle Anwendungen," Dissertation, University of Freiburg (2000).

161. B. de A. Mello, I. F. da Costa, C. R. A. Lima, and L. Cescato, "Developed profile of holographically exposed photoresist gratings," Appl. Opt. **34**(4), 597–603 (1995).

162. Lord Rayleigh, "On the Dynamical Theory of Gratings," Proceedings of the Royal Society of London. Series A, Containing Papers of a Mathematical and Physical Character **79**(532), 399–416 (1907).

163. J. E. Stewart and W. S. Gallaway, "Diffraction Anomalies in Grating Spectrophotometers," Appl. Opt. **1**(4), 421–430 (1962).

164. A. Hessel and A. A. Oliner, "A New Theory of Wood's Anomalies on Optical Gratings," Appl. Opt. **4**(10), 1275–1297 (1965).

165. A. A. Maradudin, I. Simonsen, J. Polanco, and R. M. Fitzgerald, "Rayleigh and Wood anomalies in the diffraction of light from a perfectly conducting reflection grating," J. Opt. **18**(2), 024004 (2016).

166. C. Palmer, *Diffraction Grating Handbook*, 8th ed. (MKS Instruments, 2020).

167. R. W. Wood, "XLII. On a remarkable case of uneven distribution of light in a diffraction grating spectrum," The London, Edinburgh, and Dublin Philosophical Magazine and Journal of Science **4**(21), 396–402 (1902).

168. U. Fano, "The Theory of Anomalous Diffraction Gratings and of Quasi-Stationary Waves on Metallic Surfaces (Sommerfeld's Waves)," J. Opt. Soc. Am., JOSA **31**(3), 213–222 (1941).

169. F. J. García de Abajo, "Colloquium: Light scattering by particle and hole arrays," Rev. Mod. Phys. **79**(4), 1267–1290 (2007).

170. N. Lassaline, R. Brechbühler, S. J. W. Vonk, K. Ridderbeek, M. Spieser, S. Bisig, B. le Feber, F. T. Rabouw, and D. J. Norris, "Optical Fourier surfaces," Nature **582**(7813), 506–510 (2020).

171. E. G. Loewen, M. Nevière, and D. Maystre, "Grating efficiency theory as it applies to blazed and holographic gratings," Appl. Opt. **16**(10), 2711–2721 (1977).

172. I. R. Hooper and J. R. Sambles, "Dispersion of surface plasmon polaritons on short-pitch metal gratings," Phys. Rev. B **65**(16), 165432 (2002).

173. I. R. Hooper and J. R. Sambles, "Surface plasmon polaritons on narrow-ridged short-pitch metal gratings," Phys. Rev. B **66**(20), 205408 (2002).

174. T. W. Ebbesen, H. J. Lezec, H. F. Ghaemi, T. Thio, and P. A. Wolff, "Extraordinary optical transmission through sub-wavelength hole arrays," Nature **391**(6668), 667–669 (1998).

175. H. J. Lezec, A. Degiron, E. Devaux, R. A. Linke, L. Martin-Moreno, F. J. Garcia-Vidal, and T. W. Ebbesen, "Beaming Light from a Subwavelength Aperture," Science **297**(5582), 820–822 (2002).

176. T. G. Mayerhöfer, S. Pahlow, and J. Popp, "The Bouguer-Beer-Lambert Law: Shining Light on the Obscure," ChemPhysChem **21**(18), 2029–2046 (2020).

177. A. Djorović, M. Meyer, B. L. Darby, and E. C. Le Ru, "Accurate Modeling of the Polarizability of Dyes for Electromagnetic Calculations," ACS Omega **2**(5), 1804–1811 (2017).

178. T. G. Mayerhöfer, S. Pahlow, U. Hübner, and J. Popp, "Removing interference-based effects from infrared spectra – interference fringes re-revisited," Analyst **145**(9), 3385–3394 (2020).

179. T. G. Mayerhöfer, S. Pahlow, U. Hübner, and J. Popp, "CaF2: An Ideal Substrate Material for Infrared Spectroscopy?," Anal. Chem. (2020).

180. T. Ochiai and K. Sakoda, "Dispersion relation and optical transmittance of a hexagonal photonic crystal slab," Phys. Rev. B **63**(12), 125107 (2001).

181. L. Novotny, "Strong coupling, energy splitting, and level crossings: A classical perspective," American Journal of Physics **78**(11), 1199–1202 (2010).

182. W. L. Barnes, T. W. Preist, S. C. Kitson, and J. R. Sambles, "Physical origin of photonic energy gaps in the propagation of surface plasmons on gratings," Phys. Rev. B **54**(9), 6227–6244 (1996).

183. V. B. Koman, C. Santschi, and O. J. F. Martin, "Multiscattering-Enhanced Absorption Spectroscopy," Anal. Chem. **87**(3), 1536–1543 (2015).

184. M. D. Fairchild, *Color Appearance Models*, 2. Edition (Wiley, 2005).

185. Maria Bauer, "Development of Optical Thinfilm Biosensors," Dissertation, TU Wien (2007).

186. M. Bauer, J. Haglmüller, F. Pittner, and T. Schalkhammer, "Direct Optical Visualization of DNA–DNA Interaction by Nanoparticle-Capture on Resonant PET-Films," J. Nanosci. Nanotechnol. **6**(12), 3671–3676 (2006).

187. L. Davoine, M. Schnieper, A. Barranco, and F. J. Aparicio, "Visual gas sensors based on dye thin films and resonant waveguide gratings," in *Optical Sensors 2011; and Photonic Crystal Fibers V* (International Society for Optics and Photonics, 2011), **8073**, p. 807312.

188. H. Walter, C. Harrats, P. Müller-Buschbaum, R. Jérôme, and M. Stamm, "Adsorption of Ampholytic Diblock Copolymers from Dilute Aqueous Solution at the Solid/Liquid Interface," Langmuir **15**(4), 1260–1267 (1999).

189. S. Arshavsky-Graham, E. Boyko, R. Salama, and E. Segal, "Mass Transfer Limitations of Porous Silicon-Based Biosensors for Protein Detection," ACS Sens. **5**(10), 3058–3069 (2020).

190. N. Bornemann, "Characterization and Investigation of Large-Area, Ultra-Thin Gravure Printed Layers," Dissertation, Technical University Darmstadt (2014).

191. P. Hoet and D. Lison, "Ototoxicity of Toluene and Styrene: State of Current Knowledge," Crit. Rev. Toxicol. **38**(2), 127–170 (2008).

192. H. Z. Streicher, P. A. Gabow, A. H. Moss, D. Kono, and W. D. Kaehny, "Syndromes of Toluene Sniffing in Adults," Ann Intern Med **94**(6), 758–762 (1981).

193. G. Devathasan, D. Low, P. C. Teoh, S. H. Wan, and P. K. Wong, "Complications of chronic glue (toluene) abuse in adolescents," Aust. N. Z. J. Med. **14**(1), 39–43 (1984).

194. European Chemicals Agency, *Registration, Evaluation, Authorisation and Restriction of Chemicals (REACH)*, EUR-Lex - 02006R1907-20210215 (European Parliament and Council, 2021).

195. W. Reinhart, "Hot stamping foil: vehicle for OVD concepts on optimized processing," in *Optical Security and Anticounterfeiting Systems* (International Society for Optics and Photonics, 1990), **1210**, pp. 54–58.

196. M. Lichtarowicz, "Ammonia," https://essentialchemicalindustry.org/chemicals/ammonia.html.

197. M. Thangamuthu, C. Santschi, and O. J. F. Martin, "Photocatalytic ammonia production enhanced by a plasmonic near-field and hot electrons originating from aluminium nanostructures," Faraday Discuss. (2019).

Curriculum Vitae

Personal Information

Name	Sebastian Mader
Address	Weinberghöhe 31 6340 Baar Switzerland
Mobile	+41 79 242 2696
Email	sebastian.mader.p@gmail.com
Date (Place) of Birth	16.07.1984 (Giessen, Germany)
Citizenship	German / Swiss
Marital Status	Married

Profile

- Professional experience as Project Manager at OVD Kinegram AG (Switzerland), 10 years
- Professional experience as R&D engineer and project leader at CSEM SA (Switzerland), 3 years
- Engineering consultant, Heliotis AG (Switzerland), 1.5 years, part-time
- Author and co-author of 14 patents and 9 articles
- Attendance of more than 20 national and international conferences
- Master of science in engineering degree in photonics engineering (Poland)
- Master of science degree in applied physics (Netherlands)
- Bachelor of science degree in computational physics (Switzerland)
- Bachelor of engineering degree in laser and optical technologies (Germany)

Languages

- German mother tongue
- English fluent
- Polish intermediate knowledge
- Italian basic knowledge

Education

2016/08 – to date	PhD, École Polytechnique Fédérale de Lausanne (EPFL)
2010/09 – 2011/08	Master of Science in Engineering in Photonics Engineering, Warsaw University of Technology (summa cum laude)
2009/09 – 2010/08	Master of Science in Applied Physics, Delft University of Technology
2007/09 – 2009/08	Bachelor of Science in Computational Physics, University of Basel
2003/09 – 2006/10	Bachelor of Engineering in Laser and Optical Technologies, University of Applied Sciences Jena

Professional Experience

2011/09 to date	Project Manager Product Development, OVD Kinegram AG
2006/11 – 2009/08	R&D Engineer / Project Leader, CSEM SA
2006/11 – 2008/03	Design Engineer, Heliotis AG
2005/02 – 2005/09	Internship, Jenoptik Laserdiode GmbH

Publications

- S. Mader and Olivier J.F. Martin, " Remarkable Color Gamut Enhancement of Dye Lacquers Using Corrugated Surfaces," *Adv. Phot. Res.*, **2021**, 2100245.
- S. Mader and Olivier J.F. Martin, "Engineering multi-state transparency on demand," *Light: Adv. Manuf. 2(4)*, **2021**, 1–10.
- S. Mader, C. Fraschina, and H. Walter, "Achromatic and Monochromatic Effects based on a new class of non-holographic asymmetric micro-structures," ODS Conference Proceedings, **2020**.
- S. Mader and Olivier J.F. Martin, "Mechanisms of perfect absorption in nano-composite systems," *Opt. Express* 26, **2018,** 27089-27100.
- H. Walter, C. Fraschina, and S. Mader, "Moiré in Transmission – a new and eye catching window effect," ODS Conference Proceedings, **2018**.
- H. Walter and S. Mader, "Color Movement Effects Based on Zero-Order Diffractive Filter," ODS Conference Proceedings, **2016**.
- H. Walter, S. Mader, and W. Tompkin, "Zero-order diffractive color-shift feature in reflection and transmission," ODS Conference Proceedings, **2014**.
- S. Mader, T. Kozacki, and W. Tompkin, "Limits of computational white-light holography," J. Phys.: Conf. Ser. 415, **2013**, 012046.
- H. Ma, R. Wijshoff, S. Mader, J. Veen, M. Van Der Mark, N. Bhattacharya, and P. Urbach, "A Simple and Low-cost Approach to Blood Flow Monitoring Using Speckle Contrast Technique," *AIP Conf. Proc. 1253*, **2010**, 50.

Oral Presentations

- "Achromatic and Monochromatic Effects based on a new class of non-holographic asymmetric micro-structures," Optical Document Security (ODS), San Francisco, USA, January 29-31 **2020**.
- "Mechanisms of Perfect Absorption in Nano-Composite Systems," Optics at the Nanoscale (ONS'17), Capri, Italy, September 10-14 **2017**.

Hobbies

- Hiking, tennis, snowboarding, skiing, soccer, jogging, fitness
- Languages, cooking, literature